UNIVERSITY OF CALIFORNIA SAN DIEGO

Cell membrane based nanostructure for biological neutralization

A Dissertation submitted in partial satisfaction of the requirements
for the degree Doctor of Philosophy

in

Nanoengineering

by

Dan Wang

Committee in charge:

Professor Liangfang Zhang, Chair
Professor Shaochen Chen
Professor Victor Nizet
Professor Jonathan Pokorski

2024

The Dissertation of Dan Wang is approved, and it is acceptable in quality and form for publication on microfilm and electronically.

University of California San Diego

2024

DEDICATION

This dissertation is dedicated to all those who have helped me in shaping my academic journey and personal growth. Without them, none of the work presented here would have been possible and I could not be the person I am today.

Special thanks to my loving family: Yongfeng Wang, Xiaoping Wang, and Bangyu Wang, who have supported me and belief in my abilities have been a source of strength throughout my academic career. I am also grateful to my boyfriends, Lin Sun, whose presence in my life is like sunlight that breaks through the night. His love and encouragement have provided me resilience needed to pursue my academic goals.

EPIGRAPH

"Everything is interesting if you go into it deeply enough."

--Richard Feynman

TABLE OF CONTENTS

LIST OF FIGURES

LIST OF TABLES

ACKNOWLEDGEMENTS

First and foremost, I am deeply grateful to my PhD advisor, Professor Liangfang Zhang for his guidance and support. His visionary leadership, kindness, and deep understanding of science have not only inspired me but also encourage me to be independent and strive for excellence. It is an enriching experience to work under his guidance, which made my graduate life memorable.

I would also like to thank my mentor, Dr. Weiwei Gao. His guidance has contributed to both my growth. I am particularly grateful for his patience during challenging times and his encouragement during moments of doubt. Working with him has broadened my perspectives and I learned a lot from him.

My lab mates made invaluable contributions to my work. I feel honored to be working with so many excellent researchers. I am thankful to Xiangzhao Ai for his mentorship at the beginning of my PhD journey. I acknowledge the friendship and collaboration of Lei Sun, Ilkoo Noh, Mingxuan Kai, Shuyan Wang, Yaou Duan, Weiting Shen, Nianfei Xian, Zhidong Zhou, Jiayuan Zhang, and Zhengxing Li. In addition, I want to acknowledge all the wonderful lab members I've encountered, including Animesh Mohapatra, Emily Lam, Joo H. Kang, Kailin Feng, Luke J. Kubiatowicz, Nishta Krishnan, Ronnie Fang, Rui Wang, Yiyan Yu, Zhongyuan Guo. I would like to acknowledge the alumni of out lab, from whom I gain help and guidance: Hua Gong, Joon Ho Park, Jia Zhuang, Jiarong Zhou, Maya Holy, Qiangzhe Zhang, Yao Jiang. I offer special thanks to Prof.Shaochen Chen, Prof. Victor Nizet, and Prof. John Porkski for serving on my defense committee. I would like to thank my friend and mentor, Lingyun Zhao and Sishen Feng, who provide guidance throughout my academic career. I would like to thank the undergraduate, Austin Haggard, for dedicating time and effort to the lab.

In addition, I would like to thank UCSD Jacobs Scholars Program, UCSD International Center, for recognizing my work. I would also like to thank UC San Diego for providing inclusive environment. I am grateful to Graduation coordinators and Graduate Division Staff who are friendly and provide a lot of help.

Chapter 1, in part, is a reprint of the material as it appears in *Advanced Healthcare Materials*, 2021, Dan Wang, Shuyan Wang, Zhidong Zhou, Dean Bai, Qiangzhe Zhang, Xiangzhao Ai, Weiwei Gao, and Liangfang Zhang; *Advanced Materials*, 2022, Shuyan Wang, Dan Wang, Yaou Duan, Zhidong Zhou, Weiwei Gao, and Liangfang Zhang. The dissertation author was either the primary investigator or a major contributor and co-author of these papers.

Chapter 2, in full, is a reprint of the material as it appears in *ACS nano*, 2022, Dan Wang, Xiangzhao Ai, Yaou Duan, Nianfei Xian, Ronnie H. Fang, Weiwei Gao, and Liangfang Zhang. The dissertation author was the primary author of this paper.

Chapter 3.1, in full, is a reprint of the material as it appears in *Journal of the American Chemical Society*, 2021, Xiangzhao Ai, Dan Wang, Anna Honko, Yaou Duan, Igor Gavrish, Ronnie H. Fang, Anthony Griffiths, Weiwei Gao, and Liangfang Zhang; The dissertation author was a major contributor and co-author of this paper.

Chapter 3.2, in full, is a reprint of the material as it appears in *Biomaterials*, 2023, Xiangzhao Ai, Dan Wang, Ilkoo Noh, Yaou Duan, Zhidong Zhou, Nilesh Mukundan, Ronnie H. Fang, Weiwei Gao, Liangfang Zhang. The dissertation author was a major contributor and co-author of this paper.

Chapter 4.1, in full, is a reprint of the material as it appears in *Angewandte Chemie International Edition*, 2023, Lei Sun, Dan Wang, Ilkoo Noh, Ronnie H. Fang, Weiwei Gao, and Liangfang Zhang; The dissertation author was a major contributor and co-author of this paper.

Chapter 4.2, in full, is prepared for submission for publication of the material. The dissertation author was the primary author of this paper.

VITA

2015 Bachelor of Science in Materials of Science and Engineering, Tsinghua University, China

2018 Master of Science in Materials of Science and Engineering, Tsinghua University, China

2024 Doctor of Philosophy in Nanoengineering, Univeristy of California San Diego, USA

PUBLICATIONS

1. Sun, L.; **Wang, D.***; Noh, I.*; Fang, R.; Gao, W.; Zhang, L. Synthesis of erythrocyte nanodiscs for bacterial toxin neutralization, Angewandte Chemie International Edition, 2023, 62, e202301566. (*Contributed equally)

2. **Wang, D.;** Ai, X.; Duan, Y.; Xian, N.; Fang, R.; Gao, W.; Zhang, L. Neuronal cellular nanosponges for effective detoxification of neurotoxins, ACS Nano, 2022, 16, 19145-19154.

3. **Wang, D.**; Wang, S.; Zhou Z.; Bai, D.; Zhang, Q.; Ai, X.; Gao, W.; Zhang, L. White Blood Cell Membrane-Coated Nanoparticles: Recent Development and Medical Applications, Advanced Healthcare Material, 2021, 2101349.

4. Ai, X.*; **Wang, D.***; Noh, I.; Duan, Y.; Zhou, Z.; Mukundan, N.; Fang, R.; Gao, W.; Zhang, L. Glycan-modified cellular nanosponges for enhanced neutralization of botulinum toxin. Biomaterials, 2023, 302, 122330.

5. Ai, X.*; **Wang, D.***; Honko, A.; Duan, Y.; Gavrish, I.; Fang, R.; Griffiths, A.; Gao, W.; Zhang, L. Surface glycan modification of cellular nanosponges to promote SARS-CoV-2 inhibition, Journal of the American Chemical Society, 2021, 143, 17615-17621 (*Contributed equally)

6. **Wang, D.**; Xie, W.; Gao, Q.; Yan, H.; Zhang, J.; Lu, J.; Liaw, B.; Guo, Z.; Gao, F.; Yin, L.; Zhang, G.; Zhao, L. Non-magnetic Injectable Implant for Magnetic Field-Driven Thermochemotherapy and Dual Stimuli Responsive Drug Delivery: Transformable Liquid Metal Hybrid Platform for Cancer Theranostics, Small, 2019, 1099511.

7. **Wang, D.**; Wang, J.; Xie, W.; Zhao, W.; Zhang, Y.; Sun, X.; Zhao, L. Drug-Loaded Magnetic Microhydrogel as Microwave Susceptible Agents for Cancer Multimodality Treatment and MR Imaging, Journal of Biomedical Nanotechnology, 2018, 14, 362-370.

8. Cao, Z.*; **Wang, D.***, Li, Y.; Xie, W.; Wang, X.; Tao, L.; Wei, Y.; Wang, X.; Zhao, L. Effect of nanoheat stimulation mediated by magnetic nanocomposite hydrogel on the osteogenic differentiation of mesenchymal stem cells, Science China Life Sciences, 2018, 61, 448-456. (*Contributed equally)

9. Sun, L.; Yu, Y.; Peng, Y.; **Wang, D**.; Wang, S.; Noh, I.; Fang, R.; Gao, W.; Zhang, L. Platelet membrane-derived nanodiscs for neutralization of endogenous autoantibodies and exogenous pathogens, Small 2024, 20, 2308327

10. Wang, S.; **Wang, D.**; Shen, W.; Kai, M.; Yu, Y.; Peng, Y.; Xian, N.; Fang, R.; Gao, W.; Zhang, L. "Protein-loaded cellular nanosponges for dual-biomimicry neurotoxin countermeasure", Small 2024, 20, 2309635.

11. Zhou, Z.; Kai M.; Wang, S.; **Wang, D.**; Peng,Y.; Yu, Y.; Gao, W.; Zhang, L. Emerging nanoparticle designs against bacterial infections, WIREs Nanomedicine & Nanobiotechnology, 2023, 15, e1881.

12. Duan, Y.; **Wang, D.**; Wang, S.; Zhou, Z.; Komarla A.; Zhou, J.; Zhang, Q.; Ai, X.; Gao, W.; Zhang, L. Cell membrane-coated nanoparticles and their biomedical applications, Encyclopedia of Nanomaterials, 2023, 3, 519-542.

13. Wang, S.; **Wang, D.**; Kai, M.; Shen, W.; Sun, L.; Gao, W.; Zhang, L. Design strategies for cellular nanosponges as medical countermeasures", BME Frontiers 2023, 4, 0018.

14. Wang, S., **Wang, D.**, Duan, Y.; Zhou, Z.; Gao, W.; Zhang, L. Cellular Nanosponges for Biological Neutralization, Advanced Materials, 2021, 2107719.

15. Xie, W.; Guo, Z.; Gao, Q.; **Wang, D.**; Liang, K.; Gu, Z.; Zhao, L.Y. Manganese-doped layered double hydroxide: a biodegradable theranostic nanoplatform with tumor microenvironment response for magnetic resonance imaging-guided photothermal therapy, ACS Applied Bio Materials, 2020, 3, 5845-5855.

16. Rajaee, A.; Zhao, L.; Wang, S.; **Wang, D.**; Liu, Y.; Wang, J.; Ying, K. Multifunction bismuth gadolinium oxide nanoparticles as radiosensitizer in radiation therapy and imaging, Physics in Medicine and Biology, 2019, 195007.

17. Huang, X.; **Wang, D.;** Yuan, Z.; Xie, W.; Wu, Y.; Li, R.; Zhao, Y.; Luo, D.; Cen, L.; Chen, B.; Wu, H. A Fully Biodegradable Battery for Self-Powered Transient Implants. Small. 2018, 14, 1800994.

18. Ding, H.; Lu, L.; Shi, Z.; **Wang, D.**; Li, L.; Li, X.; Ren, Y.; Liu, C.; Cheng, D.; Kim, H.; Giebink, N.C. Microscale Optoelectronic Infrared-to-Visible Upconversion Devices and Their Use as Injectable Light Sources. Proceedings of the National Academy of Sciences of the United States of America. 2018, 115, 6632-6637.

19. Liu, C.; Zhang, Q.; **Wang, D.**; Zhao, G.; Cai, X.; Li, L.; Ding, H.; Zhang, K.; Wang, H.; Kong, D.; Yin, L. High Performance, Biocompatible Dielectric Thin-Film Optical Filters Integrated with Flexible Substrates and Microscale Optoelectronic Devices, Advanced Optical Materials. 2018, 6, 1800146.

20. Xie, W.; Gao, Q.; **Wang, D.**; Guo, Z.; Gao, F.; Wang, X.; Cai, Q.; Feng, S.S.; Fan, H.; Sun, X.; Zhao, L. Doxorubicin-loaded Fe_3O_4@MoS_2-PEG-2DG nanocubes as a theranostic platform for magnetic resonance imaging-guided chemo-photothermal therapy of breast cancers, Nano Research, 2018, 11, 2470-2487.

21. Guo, Z.; Xie, W.; Gao, Q.; **Wang, D.**; Gao, F.; Li, S.; Zhao, L. In situ biomineralization by silkworm feeding with ion precursors for the improved mechanical properties of silk fiber, international journal of biological macromolecules, 2018, 109, 21-26.

22. Gao, Q.; Xie, W.; Wang, Y.; **Wang, D.**; Guo, Z.; Gao, F.; Zhao, L.; Cai, Q. A theranostic nanocomposite system based on radial mesoporous silica hybridized with Fe_3O_4 nanoparticles for targeted magnetic field responsive chemotherapy of breast cancer, RSC Advances, 2018, 8, 4321-4328.

23. Xie, W.; Gao, Q.; Guo, Z.; **Wang, D.**; Gao, F.; Wang, X.; Wei, Y.; Zhao, L. Injectable and self-healing thermosensitive magnetic hydrogel for asynchronous control release of doxorubicin and docetaxel to treat triple-negative breast cancer, ACS applied materials & interfaces, 2017, 9, 33660-33673.

24. Wang, J.; **Wang, D.**; Yan, H.; Tao, L.; Wei, Y.; Li, Y.; Wang, X.; Zhao, W.; Zhang, Y.; Zhao, L.; Sun, X. An injectable ionic hydrogel inducing high temperature hyperthermia for microwave tumor ablation, Journal of Materials Chemistry B. 2017, 5, 4110-4120.

25. Xie, W.; Gao, Q.; **Wang, D.**; Wang, W.; Yuan, J.; Guo, Z.; Yan, H.; Wang, X.; Sun, X.; Zhao, L. Melatonin potentiates 'inside-out' nano-thermotherapy in human breast cancer cells: a potential cancer target multimodality treatment based on melatonin loaded nanocomposite particles, International Journal of Nanomedicine, 2017, 12, 7351-7363.

26. Yuan, J.; Liu, J.; Song, Q.; **Wang, D.**; Xie, W.; Yan, H.; Zhou, J.; Wei, Y.; Sun, X.; Zhao, L. Photoinduced mild hyperthermia and synergistic chemotherapy by one-pot-synthesized docetaxel-loaded poly (lactic-co-glycolicacid) / polypyrrole nanocomposites. ACS Applied Materials & Interfaces. 2016, 8, 24445-24454.

ABSTRACT OF THE DISSERTATION

Cell membrane based nanostructure for biological neutralization

by

Dan Wang

Doctor of Philosophy in NanoEngineering

University of California San Diego, 2024

Professor Liangfang Zhang, Chair

Harmful reagents, including small molecules, proteins, bacteria, and viruses, have posed a serious threat to public health. The current medical countermeasures reply on accommodating the structures of the causative agents for the design of therapeutic agents. Despite their pivotal roles in treating numerous diseases, these strategies show inadequate efficacy, in part, due to the diversity of toxicants, leading to narrow-spectrum neutralization. Therefore, it is essential to explore innovative methods of biological neutralization that offer enhanced therapeutic efficacy.

The dissertation focuses on the development of novel cell membrane-based nanostructures. Cell membraned based nanoparticles represent a unique solution by mimicking susceptible host cells, intercepting harmful agents without knowing their molecular structure. By functionalization of cell membrane coated nanoparticles and exploiting novel nanostructures, these nanoformulations have potential in broad spectrum neutralization of a variety of pathological agents.

The first chapter discusses recent advances in biological neutralization using cell membrane coated nanoparticles, which explores different source cell membranes and functionalization strategies. The second chapter of this thesis introduces a new type of neuron cell membrane coated nanoparticles, highlighting its potential in neutralizing neurotoxins. Functioning as neuron decoys, these nanoparticles bind with neurotoxins, diverting them away from attacking the neurons. The third chapter of this thesis will concentrate on the functionalization of CNPs, including surface modification with heparin and ganglioside moieties via metabolic engineering. Heparin functionalized CNPs demonstrate the ability to bind with SARS-CoV-2, inhibiting viral infectivity. Glycan-modified CNPs enhance botulinum toxin binding capacity, which indicate higher detoxification efficacy than nanoparticles made from unmodified CNPs. Finally, the fourth chapter will demonstrate the design and biological neutralization of a new therapeutic platform, nanodiscs, a discoidal-shaped nanostructure. By inheriting native cell membrane functions, these nanodiscs have a broad neutralization ability against bacterial toxins and neurotoxins.

The dissertation serves as a paradigm to design nanostructures with different attributes for biological neutralization. By incorporating varying cell membrane types and surface engineering strategies, the functionalities of cell membranes are significantly enhanced. Additionally, nano discs put forth a new strategy for neutralization, counteracting the obstacles

related to toxin associated challenges. These cell membrane-based nanostructures broaden the current arsenals for biological neutralization.

Chapter 1 Introduction

1.1 Introduction

Threats from harmful molecules, either endogenous or exogenous, pose significant health problems. For example, poisoning by toxic chemicals, including drugs, nerve agents, and animal venom, leads to serious and sometimes deadly consequences.[1-3] Meanwhile, excessive production of endogenous molecules, including inflammatory cytokines, digestive enzymes, and auto-antibodies, underlie some of the most critical inflammatory disorders, such as sepsis, rheumatoid arthritis, and immune hypersensitivities.[4, 5] The threats can also come from infectious pathogens. For example, pathogenic bacteria secrete toxins in bacterial infections to manipulate host cell functions, favoring their colonization and reproduction. [6] In viral infections, viral particles attach themselves to the host cell membrane for invasion, hijacking host cell machinery to replicate.[7] To counteract these threats, biological neutralization represents a general strategy that deploys therapeutic agents to bind with the harmful molecules or pathogens, block their bioactivity, and thus prevent them from causing diseases.[8]

Therapeutic platforms, such as antisera, monoclonal antibodies, and small-molecule inhibitors, have been widely used for neutralization.[9-12] Despite their pivotal roles in treating numerous diseases, these platforms sometimes show inadequate efficacy. The reason is attributable, in part, to their design of focusing on the causative molecules or pathogens, which leads to narrow-spectrum neutralization solutions.[13] For example, some antidotes are highly effective in treating poisoning, but most deadly toxicants do not have specific pharmacological antidotes. In inflammatory disorders, existing agents neutralizing one or a few cytokines are insufficient to halt or reverse disease progression due to the multiplicity of cytokine targets and signaling network redundancy.[14] In bacterial infections, bacterial toxins display enormous

diversity of molecular structures.[15] In contrast, current neutralizing agents target specific toxin structures and require customized designs for different toxins, making their wide applications impractical. Similarly, viral neutralization focuses heavily on specific viral species and therefore cannot be deployed across different species or families of viruses or may be rendered ineffective as the virus accumulates mutations and escapes treatments.[16] Overall, these challenges underscore the need for innovative biological neutralization approaches.

Cell membrane-based nanostructures have emerged as a new therapeutic strategy. They were used as host decoys for a wide range of biological neutralization applications. Compared to traditional neutralization strategies, these nanoparticles stand out by mimicking susceptible host cells rather than accommodating the structures of the causative agents for the design of therapeutics. As all pathological agents must interact with host cells for bioactivity, these nanoparticles bypass the diversity of these agents and create function-driven and broad-spectrum neutralization solutions. Cell membrane-based nanostructures include cell membrane coated nanoparticles (CNPs) and cell membrane based nanodiscs (CNDs). CNPs comprise synthetic cores enclosed by natural cellular membranes, replicating the distinctive features of host cells to achieve unique biointerfacing capabilities.[17] By carefully selecting specific membrane types, fine-tuning membrane compositions, diversifying substrate materials, and customizing synthetic substrate physicochemical attributes, scientists have adeptly transformed CNPs into a versatile category of nanomedicine with promisingapplications.

1.2 Native cell membrane coated nanoparticles

Initial development of CNP focuses on harnessing functions of various cell types to bind with and neutralize toxins, while the synthetic core mostly serves as a template to stabilize the

membrane and maintain an overall small size critical for high collision frequency and potent toxin neutralization.

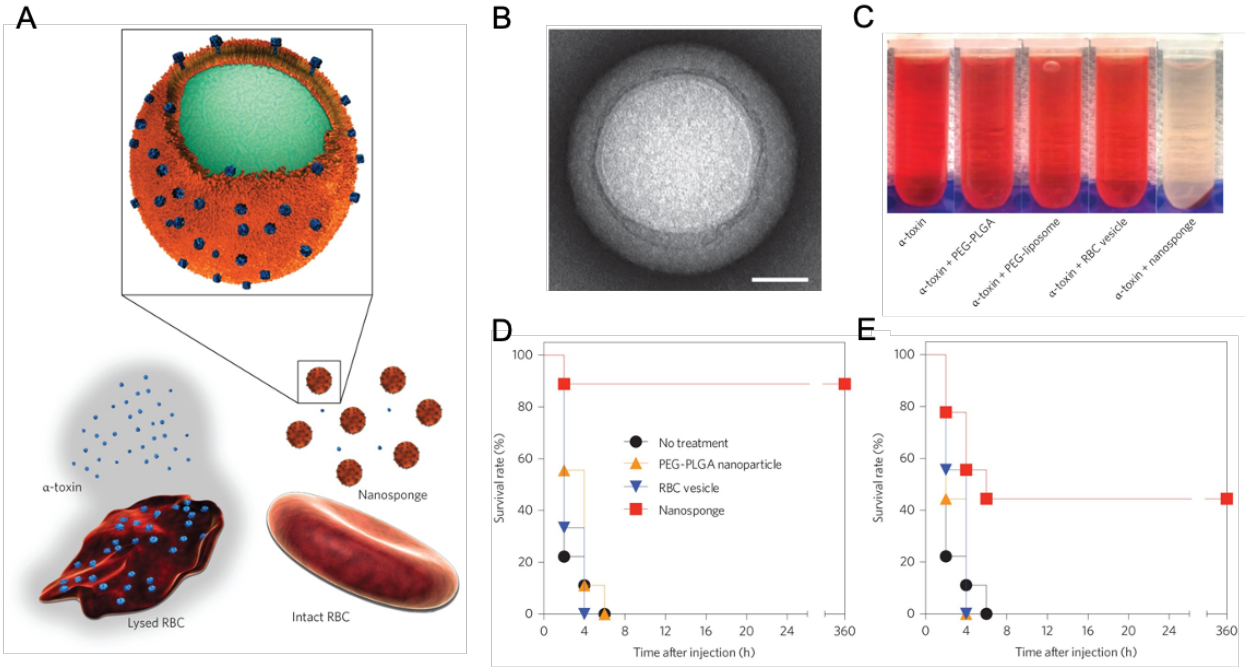

Figure 1.1 A biomimetic CNP that absorbs pore-forming toxins

Schematic structure of RBC-NPs and their mechanism of neutralizing PFTs. Secreted by bacteria, PFTs perforate cell membranes and lyse the RBCs. After absorbing PFTs, CNPs diverted the toxins away from their cellular targets, preventing toxin-mediated haemolysis. (B) TEM visualization of a PFTs-absorbed CNPs (scale bar, 20 nm). (C) Centrifuged RBCs after incubation with α-toxin mixed in PBS, PLGA nanoparticles, liposomes, RBC membrane vesicles or CNPs indicated the ability of the CNPs to neutralize PFTs. (D, E) Survival rates of mice over 15 days following an intravenous injection of α -toxin (75 μg/kg). The RBC-NPs, RBC vesicles or PEG–PLGA nanoparticles were administered intravenously 2 min either before (D) or after (E) the toxin injection. All injections were performed via tail vein (n = 9). Copyright 2013, Nature Publishing Group.

1.2.1 Blood cell membrane coated nanoparticles

Red blood cells (RBCs) are long-circulating delivery vehicles in the body. The ability is largely mediated by their surface markers, including CD47 and complement regulatory proteins. RBCs membrane-coated nanoparticles (denoted 'RBC-NPs') were initially developed to mimic natural RBCs and prolong nanoparticle circulation but soon were applied to neutralize RBC susceptible toxins. [18] Particularly, pore-forming toxins (PFTs) are virulence factors secreted by

bacteria that perforate cell membranes for bioactivity. RBC-NPs absorbed PFTs and diverted them away from their intended cellular targets. These nanoparticles acted as host decoys and effectively neutralized alpha-hemolysin (Figure 1.1).[19] Based on the same working principle, they were also shown to neutralize other PFTs, such as melittin, listeriolysin O (LLO), streptolysin O (SLO), hemotoxin, and cytolysin.[20-24]

Following the initial development, RBC-NPs were also applied to neutralize pathological antibodies and small molecule toxicants. In antibody induced anemia (AIHA), autoantibodies attack the surface antigens present on RBCs, leading to a decreased number of RBCs in the blood. Current treatments start with systemic cytotoxic drugs and B cell-depleting monoclonal antibodies, followed by splenectomy depending on patient response to the therapy. Considerable iatrogenic risk was imposed while spleen removal heightens susceptibility to severe infections.[25] By serving as an alternative target for autoantibodies, RBC-NPs deplete circulating autoantibodies without contributing additional toxic metabolites. [26] As a small molecule neurotoxic chemical, organophosphorus compounds (OPs) disrupt cholinergic synaptic transmissions by inactivating acetylcholinesterase (AChE), a membrane-anchored protein on RBCs, neuromuscular junctions, and cholinergic brain synapses. RBC-NPs with AChE receptors on its surface preserved RBC AChE enzymatic activity. By scavenging dichlorvos (DDVP), a model OPs, these nanoparticles improved the survival of lethal DDVP challenged mice. [27]

Besides RBC-NPs, CNPss made with membranes from other types of blood cells were also developed for biological neutralization. Platelet is a blood circulating sentinel for vascular damage and invasive microorganisms. Its main function is maintaining hemostasis as they stop bleeding via recruiting to sites of vascular injury and triggering the coagulation cascade. [28] Platelets are also a major player in modulating innate immunity or regulating tumor growth and

metastasis. Platelets membrane-coated nanoparticles (denoted 'PNP') inherit rich surface moieties of platelets and show platelet-like functions such as immune modulation, subendothelium adhesion, and pathogen interactions. [29] For example, PNP offered specific glycosphingolipid receptors for neutralizing Shiga toxin (Stx), a toxin produced by Escherichia coli that induces hemolytic uremic syndrome. [30] In another example, by absorbing methicillin-resistant Staphylococcus aureus (MRSA) secreted toxins, PNPs blocked platelet and macrophage damage induced by these toxins, demonstrating therapeutic benefit against MRSA infection in vivo. [31] Like RBC-NP, PNPs also neutralize anti-platelet antibodies that otherwise cause immune thrombocytopenia purpura (ITP). [32]

1.2.2 White blood cell membrane coated nanoparticles

White blood cells (WBCs), such as macrophages, dendritic cells, B cells, T cells and neutrophils, are also blood cells playing critical roles of immune modulation, pathogen clearance, and tissue repair. WBC membrane coated nanoparticles (WBC-NPs) mimic host cells to bind with bacterial endotoxins, inflammatory cytokines, or viruses, diverting them away from their intended host target.[19] Such a decoy-based working mechanism can bypass the need to elucidate biomolecule structures or pathogen signaling pathways often too complex to understand.[33] This neutralization property makes WBC-NPs a versatile and broad-spectrum countermeasure platform technology (Figure 1.2).

For example, MΦ-NPs have been developed to sequester bacterial endotoxins in sepsis. When bacteria invade the host, macrophages bind to bacterial endotoxins through toll-like receptor 4 (TLR-4) and CD14. These macrophages then release proinflammatory cytokines such as tumor necrosis factor-alpha (TNF-α), interleukin 6 (IL-6), and interferon-gamma (IFN-γ). These cytokines further activate other macrophages. Such signaling propagation may lead to

sepsis. In severe sepsis, septic shock may occur, resulting in multiorgan damage and death. To manage sepsis, MΦ-NPs were made by coating J774 mouse macrophage membranes onto PLGA cores (Figure1.3).[34] By acting as macrophage decoys, these nanoparticles bound and neutralized endotoxins that would otherwise trigger immune activation.

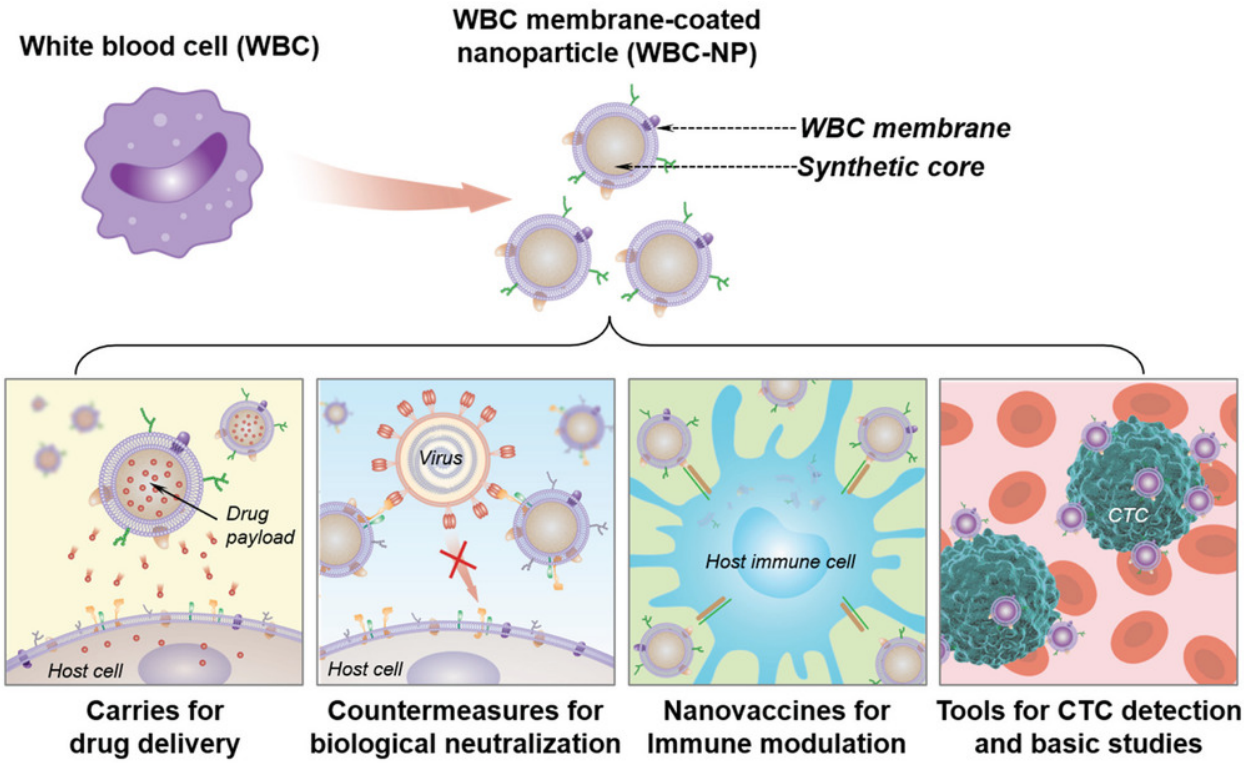

Figure 1.2 A schematic summary of using white blood cell (WBC) membrane-coated nanoparticles (WBC-NPs) for medical applications.

WBC-NPs are made by cloaking plasma membranes derived from natural WBCs onto synthetic cores. WBC-NPs inherit natural cellular markers on the source cell membranes for biointerfacing. WBC-NPs have been applied to numerous research areas including their use as carriers for drug delivery, as countermeasures for biological neutralization, as nanovaccines for immune modulation, and as tools for circulating tumor cell (CTC) isolation and basic studies.

Besides, they sequestered proinflammatory cytokines and inhibited their ability to potentiate the sepsis cascade. In a mouse model of LPS-induced endotoxemia, MΦ-NPs reduced lethality and serum proinflammatory cytokine levels after intravenous administration. When mice were challenged with a lethal dose of Escherichia coli intraperitoneally, MΦ-NPs alleviated

bacteria burden, lowered proinflammatory cytokines in the blood and major organs, and ultimately improved overall survival rate. Macrophage membranes were also coated onto iron oxide nanoparticles for LPS sequestration in sepsis management.[35] The positively charged iron oxide nanoparticles were coated with negatively charged macrophage membrane through extrusion. The resulting MΦ-NPs were administered intravenously into endotoxemia mice. They sequestered LPS and reduced serum levels of proinflammatory cytokines. By halting the immune response, these nanoparticles also conferred a survival benefit.

MΦ-NPs were also used to inhibit bacterial infections. The primary antibacterial mechanism is the neutralization of LPS and proinflammatory cytokines, which promoted bacterial uptake by macrophages. Additional antibacterial actions can be introduced by selecting core materials that have antibacterial capabilities. For example, MΦ-NPs were prepared with a composite nanoparticle core containing bactericidal TiO2 to treat bacterial infection in the bone.[36] In the MΦ-NP synthesis, composite nanoparticle cores were first cultured with macrophage cells for phagocytosis. Then, an external electric field was applied to the cells, inducing membrane re-assemble and nanoparticle coating. These MΦ-NPs absorbed LPS and proinflammatory cytokine IL-6, attenuating subsequent macrophage activation in vitro. Under UV-irradiation, the TiO2 core generated reactive oxygen species (ROS) that killed bacteria directly.

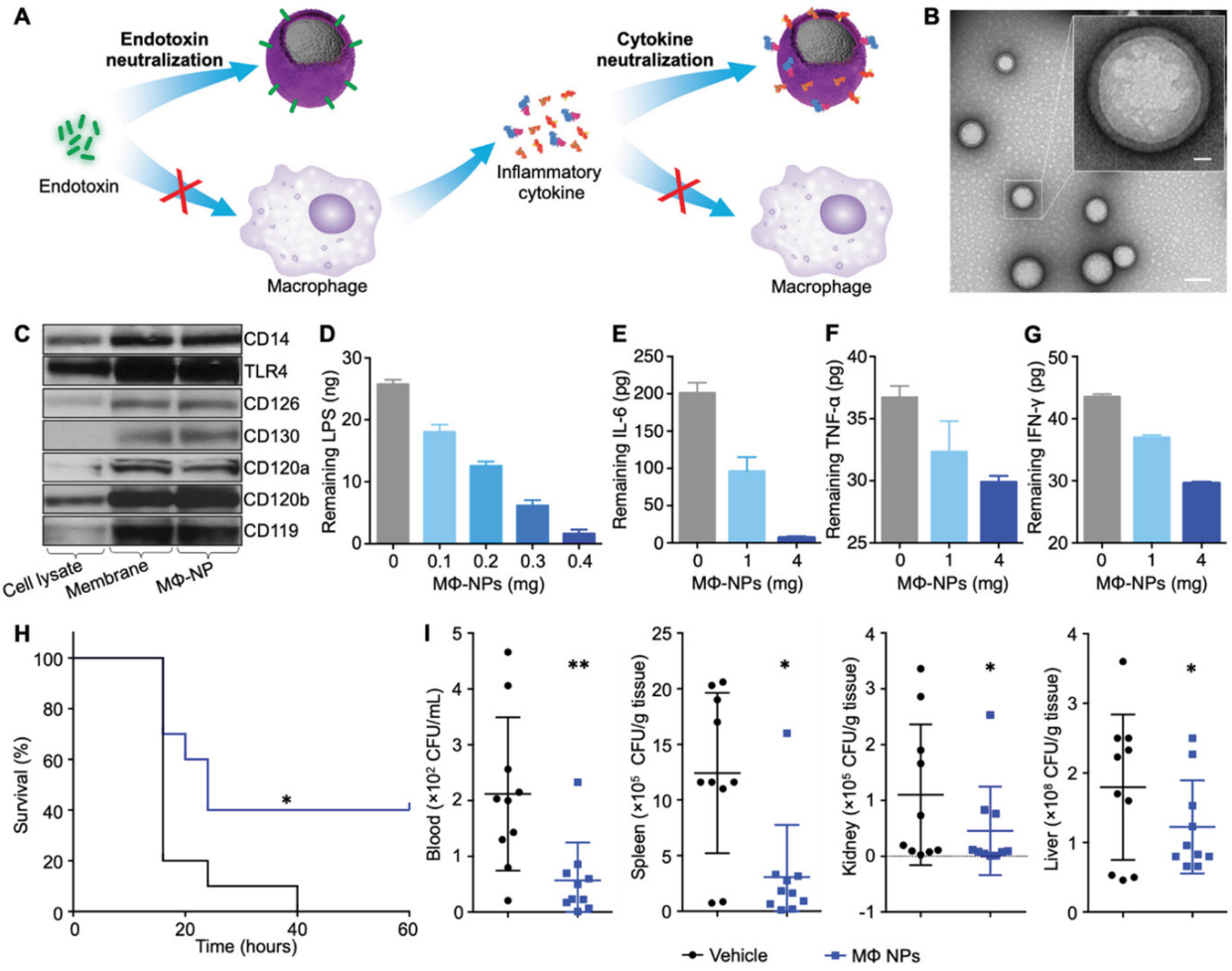

Figure 1.3 Macrophage membrane-coated nanoparticles (MΦ-NPs) concurrently absorbing endotoxins and proinflammatory cytokines for sepsis management.

A) Schematic representation of using MΦ-NPs to neutralize endotoxins and proinflammatory cytokines as a two-step process for sepsis management. B) TEM images of MΦ-NPs negatively stained with uranyl acetate. (Scale bar: 100 nm) Inset: a zoomed-in view of a single MΦ-NP. (Scale bar: 10 nm) C) Representative protein bands of macrophage cell lysate, membrane vesicles, and MΦ-NPs resolved using Western blotting. D) Quantification of LPS removal with a fixed amount of LPS (25 ng) while varying MΦ-NPs. E–G) Removal of proinflammatory cytokines, including E) IL-6, F) TNF-α, and G) IFN-γ, with MΦ-NPs (n = 3, mean ± standard deviation). H) Survival curve of mice with bacteremia after treatment with MΦ-NPs (n = 10). I) Bacterial enumeration in blood, spleen, kidney, and liver at 4 h after MΦ-NPs was intraperitoneally injected. *$p < 0.05$, **$p < 0.01$. Copyright 2017, National Academy of Sciences.

Besides sepsis and bacterial infections, MΦ-NPs were also used as anti-inflammatory therapeutics to treat other disorders. For example, MΦ-NPs rescued transplanted liver from

ischemia-reperfusion injury (I/RI) through LPS sequestration.[37] In this case, intravenously administered MΦ-NPs neutralized LPS in circulation and inhibited the activation of hepatic macrophages, which together effectively halted the pathogenesis of hepatic I/RI. In addition, MΦ-NPs also controlled inflammation and accelerated bone repair after traumatic bone injury.[38] In the study, MΦ-NPs neutralized inflammatory cytokines in the injured bone tissue to safeguard the synthesis of mineralized extracellular matrix for bone regeneration. Meanwhile, the gold nanocage core generated heat under near-infrared (NIR) irradiation and released resolvin D1, an anti-inflammatory drug. Furthermore, macrophage membranes were coated onto amphiphilic chitosan oligosaccharide nanoparticle cores responsive to ROS for degradation.[39] When used to treat atherosclerosis, these MΦ-NPs neutralized inflammatory cytokines in the atherosclerotic tissues, including TNF-α, IL-1β, and IL-6. The rich ROS in the inflamed atherosclerotic tissue triggered the degradation of the nanoparticle cores and thus released atorvastatin, the antiatherosclerotic payload, for further anti-inflammatory treatment.

In addition to MΦ-NPs, nanoparticles coated with neutrophil membranes (denoted "neutrophil-NPs") were also applied to treat inflammatory disorders such as rheumatoid arthritis. In this case, neutrophil membranes were coated onto PLGA cores to neutralize inflammatory cytokines that would otherwise drive progressive joint damage.[40] These nanoparticles mirror the cytokine receptors on the source cells. They inhibit multiple types of cytokines concurrently, overcoming the complexity and heterogeneity of the inflammatory network. In mouse models of inflammatory arthritis, neutrophil-NPs suppressed synovial inflammation and elicited a robust chondroprotective effect. Neutrophil-NPs were also applied to reverse immunosuppression in the tumor microenvironment.[39] In this regard, neutrophil-NPs neutralized granulocyte-macrophage colony-stimulating factor (GM-CSF) and chemokine ligand 2 (CXCL2) in vivo. As

a result, they inhibited the generation, expansion, and tumor-tropic migration of myeloid-derived suppressor cells (MDSCs) that would otherwise establish an immunosuppressive tumor microenvironment. In mice bearing subcutaneous B16F10 tumor, intravenously administered neutrophil-NPs inhibited the migration of MDSCs, promoted tumor infiltration and activation of T lymphocytes, and enhanced the anticancer efficacy of checkpoint blockade cancer immunotherapy.

Recently, nanoparticles coated with WBC membranes were also used for viral neutralization. These WBC-NPs inherit key surface receptors from their parent cells for viral binding, blocking the viruses from interacting with their intended host targets. For example, T cell membrane-coated PLGA nanoparticles (TNPs) were developed for HIV neutralization.[41] The TNPs utilized T cell viral receptors, including CD4, C–C chemokine receptor type 5 (CCR5), and C–X–C chemokine receptor type 4 (CXCR4) for binding with viral envelope glycoprotein gp120. By acting as decoys, TNPs inhibited the gp120-mediated killing of T cells and the infection of peripheral blood mononuclear cells (PMBCs) by HIVs in vitro. The TNPs further neutralized 125 strains of HIV pseudoviruses across major circulating clades, demonstrating broad-spectrum neutralization capability. Following the same principle, MΦ-NPs were applied to inhibit SARS-CoV-2 infectivity (Figure 1.4).[42] The nanoparticles retained critical SARS-CoV-2 binding receptors on the surface, including ACE2, C-type lectin domain family 10 (CLEC10), and CD147. When tested against authentic SARS-CoV-2 virus, MΦ-NPs inhibited viral infectivity in vitro. The multifunctionality and engineering flexibility of WBC-NPs may provide additional advantages for antiviral applications. For example, combining cytokine neutralization and viral binding is an attractive strategy as sepsis also causes major fatality in sustained viral infections.[43] Additional viral receptors can be added onto the cell

membranes through chemical conjugation, lipid insertion, or genetic engineering. Such membrane modification can increase the nanoparticle-virus affinity for better antiviral outcomes.

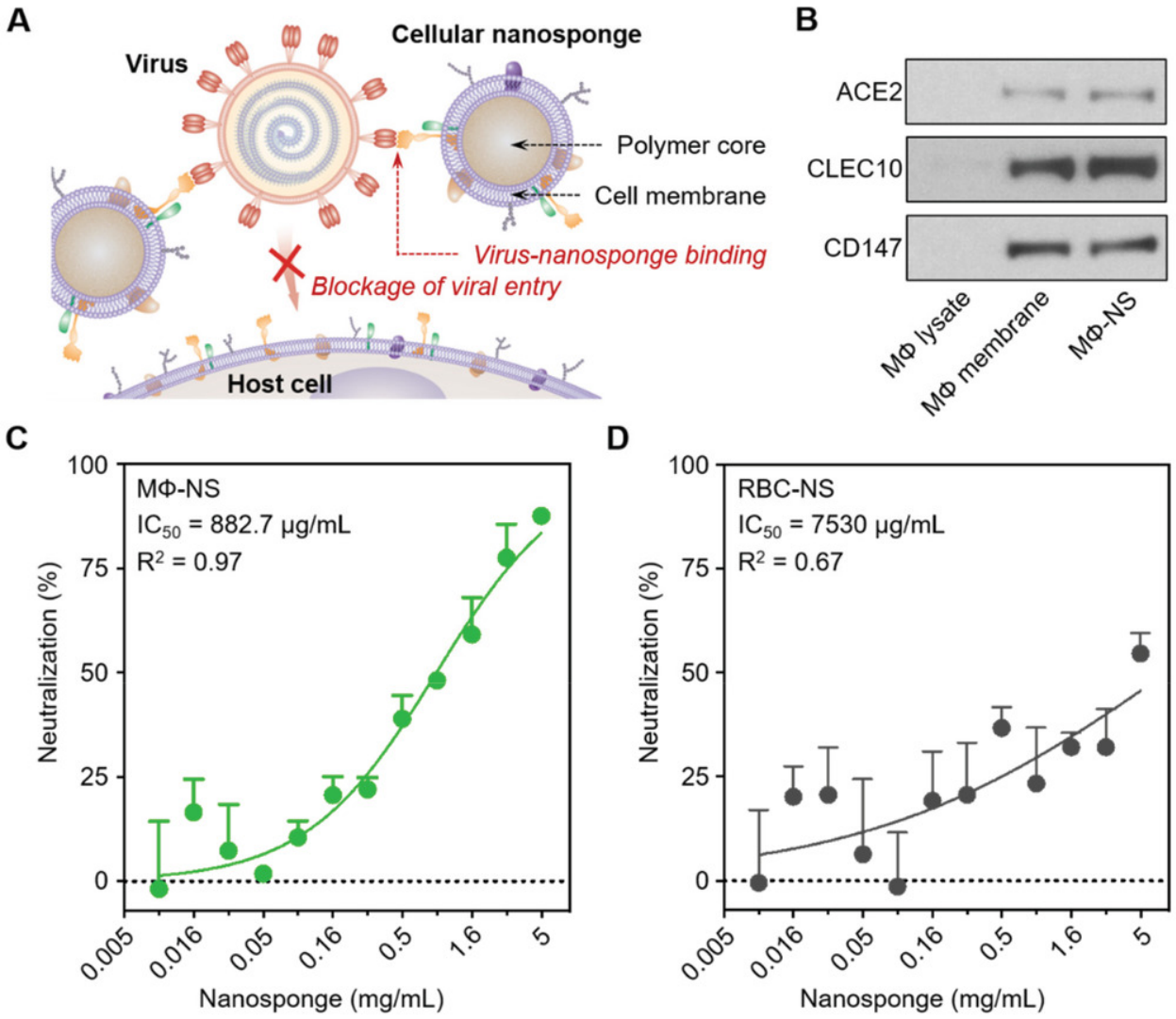

Figure 1.4 Cellular nanosponges inhibit SARS-CoV-2 infectivity.

A) Schematic mechanism of cellular nanosponges inhibiting SARS-CoV-2 infectivity. B) Selective protein bands of cell lysate, cell membrane vesicles, and cellular CNPs resolved with Western blotting analysis. C,D) The neutralization against SARS-CoV-2 infection by C) MΦ-NS and D) CNPs made from RBC membrane (RBC-NS, used as control) was tested using live SARS-CoV-2 viruses on Vero E6 cells. The IC50 value for MΦ-NS was found to be 882.7 μg mL^{-1} (membrane protein concentration). Data are presented as mean + standard deviation (n = 3). A horizontal dashed line marks the zero levels. IC50 value was derived from the variable slope model using Graphpad Prism 8. Copyright 2020, American Chemical Society.

A summary of WBC-NPs developed for biological neutralization is listed in Table 1.1. Overall, WBC-NPs have been shown to neutralize bacterial endotoxin, inflammatory cytokines, and viruses, with applications in treating various diseases, including infections, cancers, and inflammatory disorders. These nanoparticles have shown to be effective countermeasure nanotherapeutics with broad-spectrum neutralization activity. The multifunctionality and engineering flexibility of the WBC-NPs implies significant potentials of these nanoparticles for broad medical applications.

Table 1.1 Selective WBC-NPs developed for biological neutralization

Source cell	Disease	Key target
Macrophage	Sepsis	LPS and inflammatory cytokines
	Liver transplant	LPS and inflammatory cytokines
	Atherosclerosis	Cytokines and oxidated LDL
	Viral injection	SARS-Cov-2
Neutrophil	Inflammatory arthritis	Inflammatory cytokines
	Cancer	Cytokines and chemokines
T cell	Viral infection	HIV

1.2.3 Bacterial membranes coated nanoparticles

Besides mammalian cells, bacterial membranes have also been used as coating materials to make cellular CNPs. Pathogenic bacteria adhere to the host cells via surface receptors, allowing them to multiply in the host. For example, *Helicobacter pylori* (*H. pylori*) bacteria had the species-specific tissue tropism due to a plethora of adhesins on its surface, leading to the development of gastritis ulcers and gastric cancer. Polymeric nanoparticles coated with *H. pylori*

outer membrane (denoted ‘OM-NPs’) occupied binding sites on the host cells and in turn reduced bacteria attachment (Figure 1.5). They also promoted dissociation of colonized *H. pylori* from infected mouse stomach tissue. [44]

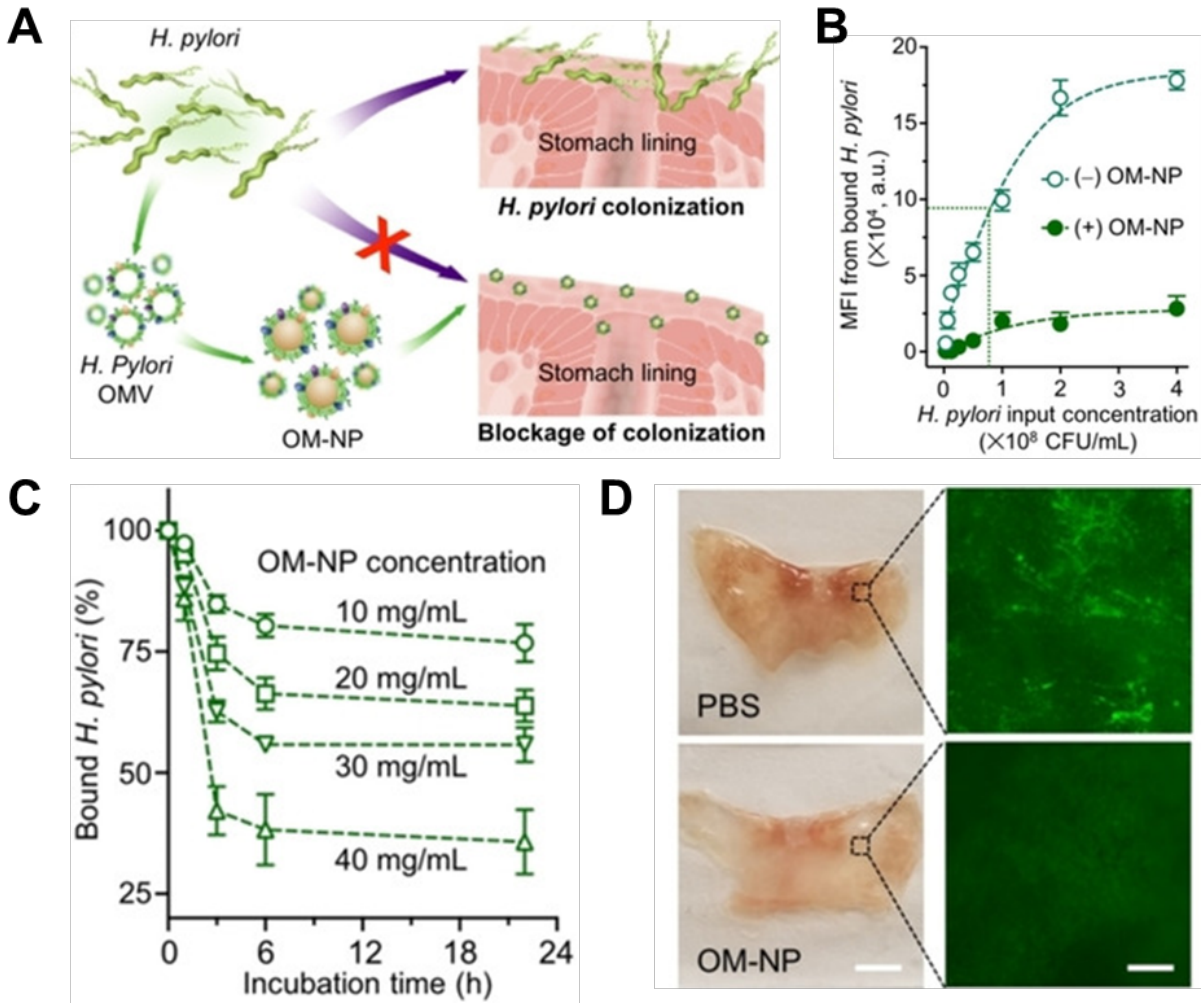

Figure 1.5 Bacterial membrane coated nanoparticles against bacterial infections

(**A**) OM-NPs inherit outer bacteria antigens to inhibit colonization of H. pylori on the stomach lining by competing with *H. pylori* bacteria. (**B**) Treatment with OM-NPs reduces *H. pylori* adhesion on AGS cells. (**C**) Remaining *H. pylori* on AGS cells after incubation with OM-NPs decreases with increase of OM-NPs concentration, indicating bacteria dissociation ability of OM-NPs. (**D**) OM-NPs reduce H. pylori colonization on the mouse stomach tissue. Mouse stomach tissue is incubated with PBS or OM-NPs before H. pylori is added. Scale bar=5 mm.

1.3 Engineering cell membrane-coated nanoparticles

1.3.1 Fine-tuning membrane composition

To enhance the functionalities of CNPs, researchers have also tailored the membrane composition of CNPs for improved therapeutic performance. Various techniques have been explored, including lipid insertion, membrane hybridization, metabolic engineering, and genetic modification (Table 1.2).

Lipid insertion exploits the fluidity of bilayered lipid membranes to functionalize CNPs with the assistance of lipid tethers. This involves synthesizing ligand-linker-lipid conjugates, which are then spontaneously inserted into membranes through hydrophobic interactions. For instance, 1,2-distearoyl-sn-glycero-3phosphoethanolamine-N-[amino(polyethyleneglycol)-2000] (PEG-DSPE) was conjugated with folate or aptamers, and the lipid tether facilitated the anchoring of these small molecules onto the membrane. The resulting functionalized CNPs targeted folate receptors-overexpressing KB cells and nucleolin-overexpressing MCF-7 breast cancer cells, exhibiting higher cellular uptake compared to non-targeted CNP counterparts [45]. PEG-DSPE has also been employed to anchor antibodies onto CNPs, targeting human epidermal growth factor receptor 2 (HER2), epithelial growth factor receptor (EGFR), or epithelial cell adhesion molecule (EpCAM) on cancer cells [46].

Another strategy involves coating nanoparticles with hybrid membranes originating from distinct cell types, resulting in hybrid membrane-coated nanoparticles ("hybrid cellular nanoparticles" or "hybrid CNPs") with enhanced multi-functionalities and multitasking capabilities. For example, cancer cell-RBC hybrid CNPs exhibited prolonged blood circulation and increased accumulation at the tumor site [47]. Hybrid CNPs formed by the fusion of cancer cell membranes with white blood cell (WBC) membranes demonstrated enhanced detection

sensitivity for circulating tumor cells due to reduced interaction with background WBCs [48]. Additionally, the fusion of cancer cell membranes with dendritic cell (DCs) membranes resulted in hybrid CNPs combining antigen-presenting abilities with homotypic targeting, showing higher anti-tumor efficacy in 4T1 tumor-bearing mice [49].

Metabolic engineering directly manipulates membrane composition through cellular metabolic pathways by culturing source cells with modified metabolic substrates. For instance, glycoengineering employs sugar substrates such as N-acetylmannosamine (ManNAc), N-acetylneuraminic acid (Neu5Ac), N-acetylgalactosamine (GalNAc), and fucose to manipulate glycosylation pathways. In a specific application, azido group (N3) modified ManNAc was used to introduce N3 on human macrophage membranes, and the resulting N3-labeled T cell membranes coated nanoparticles were conjugated with heparin, inhibiting SARS-CoV-2 infectivity [50]. Phospholipid engineering, another metabolic engineering approach, employs choline substrates to modify cell membranes through a natural biolipid synthesis pathway. For instance, macrophages incubated with azide-choline were engineered, and the resulting membranes were conjugated with a tumor-targeting peptide and coated onto Fe3O4 nanoparticles for siRNA delivery [51].

Genetic engineering involves directly modifying cell membrane surface proteins through selective gene editing. DNA or mRNA is intracellularly delivered into the cytosol by various methods, and the genetically modified membranes are then coated onto nanoparticles, imparting CNPs with various functions, including targeting ability [52]., prolonged circulation [53]., and immune modulation [54]. In an example, C1498 mouse leukemia cells were engineered to overexpress VLA-4, and the resulting engineered membrane-coated nanoparticles targeted vascular cell adhesion molecule-1 (VCAM-1) on inflamed endothelial cells, improving anti-

inflammatory drug delivery to inflamed lungs and demonstrating therapeutic efficacy in a murine model of endotoxin-induced lung inflammation [55]

Table 1.2 Representative strategies of tailoring cell membrane composition

Method	Highlight	Reference
Lipid insertion	Efficient, applicable to many ligands	[46]
Membrane hybridization	Provide CNPs with functionalities exclusive to individual membranes	[48]
Metabolic engineering	Alter membrane composition directly with minimum impact to membrane function. The subsequent conjugation is applicable to many ligands.	[50]
Genetic engineering	Alter membrane composition directly with biocompatibility. Stable expression minimizes downstream manufacturing effort.	[52]

1.3.2 Customizing substrate physicochemical attributes

Besides membrane functionalization, the customization of substrate physicochemical properties, including size, shape, anisotropy, dimension, and elasticity, can further enhance the functionalities of Cellular Nanoparticles (CNPs). Smaller nanoparticles have demonstrated prolonged circulation time and enhanced tumor accumulation, whereas larger nanoparticles are more susceptible to organ capture, resulting in reduced tumor accumulation. For instance, RBC membrane-coated mesoporous silica nanoparticles with a 60nm core size exhibited prolonged blood circulation compared to those with a 90nm core size [56]. Similarly, bacteria membrane-coated gold nanoparticles with a smaller core size (30nm) showed higher lymph node accumulation compared to CNPs with a larger core size (90nm), enhancing antibacterial immune responses [57].

Table 1.3 Common customizable physicochemical attribute of CNP substrate

Physicochemical attributes	**Properties**	**Reference**
Size	A smaller size may prolong circulation time ideal for passive targeting. A larger size may facilitate organs to capture the CNP.	[56]
Shape	An anisotropic shape may better resist cell clearance and therefore enhance neutralization efficiency.	[58]
	CNPs with cubic gold cores demonstrate photothermal effect.	[59]
Aspect ratio	Planar device with membrane coating enables highly sensitive toxin detection	[60]
	Nanofibers with pancreatic beta cells coating enhance insulin secretions	[61]
Mechanical properties	Softer CNPs with a more protein-rich surface showed lower macrophage uptake and higher cancer cell uptake.	[62]

The particulate shape of CNPs is a crucial factor in customizing their biological properties. Nanoparticles with anisotropic shapes, whether prolate or oblate ellipsoids, demonstrated immune evasion capabilities, synergizing with a red blood cell membrane coating to prolong circulation half-life in the bloodstream. Additionally, due to their increased surface

area, these CNPs exhibited improved efficacy in detoxifying toxins in a mouse model of alpha toxin intoxication compared to their spherical counterparts [58]. Cubic particles, such as gold nanocages, have also been used as core materials, exhibiting tunable photothermal effects. Combined with the stealth effect of RBC membranes, these CNPs demonstrated therapeutic efficacy upon near-infrared (NIR) irradiation in a mouse model of breast cancer [59]. Moreover, cell membranes have been coated onto materials with different aspect ratios, such as nanofibers or planar devices, adding dimension and flexibility. For instance, RBC membranes were coated onto carbon nanotube-based field-effect transistors (FETs), demonstrating high sensitivity in detecting PFTs [60]. Additionally, nanofibers coated with pancreatic beta cell membranes were used to enhance the insulin secretion function of beta cells [61].

The mechanical properties of nanoparticle cores have been reported to impact the bio-interfacing properties of CNPs. In a study, mesenchymal stem cell membranes were coated onto silica nanocapsules (referred to as "MCSN") with different elasticity [63]. Compared with stiff MCSN, soft MCSN demonstrated a higher concentration of CXCR4 and CD90 receptors on the surface, leading to enhanced uptake by Huh-7 liver cancer cells. The customization of physicochemical properties has a great impact on the functionalization of CNPs (Table 1.3).

1.4 Summary and outlook

Overall, CNPs are powerful nanomedicine platforms that leverage cell membrane functions for detoxification. They have opened therapeutic opportunities for critical diseases currently challenging or untreatable. As our understandings on cellular mechanisms of diseases deepens, cellular CNPs will play more important roles in future medicine.

Fine-tuning sizes enable CNPs to achieve prolonged circulation and increased tumor accumulation. Moreover, particulate shape and mechanical properties contribute to

biointerfacing properties, impacting their efficacy in biological applications. Coating cell membranes onto materials with diverse aspect ratios introduces dimension and flexibility. These refined physicochemical customizations improve CNPs design, elevating their capabilities for intricate biointerfacing scenarios. The combination of these approaches with membrane functionalization highlights the multifaceted strategies aimed at CNP functionalities for diverse biological applications.

Chapter 1, in part, is a reprint of the material as it appears in Advanced Healthcare Materials, 2021, Dan Wang, Shuyan Wang, Zhidong Zhou, Dean Bai, Qiangzhe Zhang, Xiangzhao Ai, Weiwei Gao, and Liangfang Zhang; Advanced Materials, 2022, Shuyan Wang, Dan Wang, Yaou Duan, Zhidong Zhou, Weiwei Gao, and Liangfang Zhang. The dissertation author was either the primary investigator or a major contributor and co-author of these papers.

1.5 References

[1] P. Masson, Evolution of and perspectives on therapeutic approaches to nerve agent poisoning, Toxicology letters 206(1) (2011) 5-13.

[2] Y.S. Chan, R.C.F. Cheung, L. Xia, J.H. Wong, T.B. Ng, W.Y. Chan, Snake venom toxins: toxicity and medicinal applications, Applied microbiology and biotechnology 100 (2016) 6165-6181.

[3] S. Costanzi, J.-H. Machado, M. Mitchell, Nerve agents: what they are, how they work, how to counter them, ACS chemical neuroscience 9(5) (2018) 873-885.

[4] R.S. Hotchkiss, D.W. Nicholson, Apoptosis and caspases regulate death and inflammation in sepsis, Nature Reviews Immunology 6(11) (2006) 813-822.

[5] Q. Guo, Y. Wang, D. Xu, J. Nossent, N.J. Pavlos, J. Xu, Rheumatoid arthritis: pathological mechanisms and modern pharmacologic therapies, Bone research 6(1) (2018) 15.

[6] J.K. Rudkin, R.M. McLoughlin, A. Preston, R.C. Massey, Bacterial toxins: Offensive, defensive, or something else altogether?, Plos pathogens 13(9) (2017) e1006452.

[7] D.S. Dimitrov, Virus entry: molecular mechanisms and biomedical applications, Nature Reviews Microbiology 2(2) (2004) 109-122.

[8] L. Zhang, J.-C. Leroux, Current and forthcoming approaches for systemic detoxification, Advanced drug delivery reviews (2015).

[9] Y. Hoshino, H. Koide, K. Furuya, W.W. Haberaecker III, S.-H. Lee, T. Kodama, H. Kanazawa, N. Oku, K.J. Shea, The rational design of a synthetic polymer nanoparticle that neutralizes a toxic peptide in vivo, Proceedings of the National Academy of Sciences 109(1) (2012) 33-38.

[10] J.A. Maynard, C.B. Maassen, S.H. Leppla, K. Brasky, J.L. Patterson, B.L. Iverson, G. Georgiou, Protection against anthrax toxin by recombinant antibody fragments correlates with antigen affinity, Nature biotechnology 20(6) (2002) 597-601.

[11] D. Hering, W. Thompson, J. Hewetson, S. Little, S. Norris, J. Pace-Templeton, Validation of the anthrax lethal toxin neutralization assay, Biologicals 32(1) (2004) 17-27.

[12] T.C. Bulfone, S.P. Samuel, P.E. Bickler, M.R. Lewin, Developing Small Molecule Therapeutics for the Initial and Adjunctive Treatment of Snakebite, Journal of Tropical Medicine 2018 (2018).

[13] K. Chen, Y. Zhu, Y. Zhang, T. Hamza, H. Yu, A. Saint Fleur, J. Galen, Z. Yang, H. Feng, A probiotic yeast-based immunotherapy against Clostridioides difficile infection, Science translational medicine 12(567) (2020) eaax4905.

[14] S. Iwata, Y. Tanaka, Progress in understanding the safety and efficacy of Janus kinase inhibitors for treatment of rheumatoid arthritis, Expert review of clinical immunology 12(10) (2016) 1047-1057.

[15] J.S. Henkel, M.R. Baldwin, J.T. Barbieri, Toxins from bacteria, Molecular, Clinical and Environmental Toxicology: Volume 2: Clinical Toxicology (2010) 1-29.

[16] E. Bekerman, S. Einav, Combating emerging viral threats, Science 348(6232) (2015) 282-283.

[17] R.H. Fang, A.V. Kroll, W. Gao, L. Zhang, Cell membrane coating nanotechnology, Advanced materials 30(23) (2018) 1706759.

[18] M.D. Peraro, F.G. Van Der Goot, Pore-forming toxins: ancient, but never really out of fashion, Nature reviews microbiology 14(2) (2016) 77-92.

[19] C.-M.J. Hu, R.H. Fang, J. Copp, B.T. Luk, L. Zhang, A biomimetic nanosponge that absorbs pore-forming toxins, Nature nanotechnology 8(5) (2013) 336-340.

[20] A.L. LaGrow, P.S. Coburn, F.C. Miller, C. Land, S.M. Parkunan, B.T. Luk, W. Gao, L. Zhang, M.C. Callegan, A novel biomimetic nanosponge protects the retina from the Enterococcus faecalis cytolysin, Msphere 2(6) (2017) e00335-17.

[21] V. Chhabria, S. Beeton, Development of nanosponges from erythrocyte ghosts for removal of streptolysin-O from mammalian blood, Nanomedicine 11(21) (2016) 2797-2807.

[22] T. Escajadillo, J. Olson, B.T. Luk, L. Zhang, V. Nizet, A red blood cell membrane-camouflaged nanoparticle counteracts streptolysin O-mediated virulence phenotypes of invasive group A Streptococcus, Frontiers in pharmacology 8 (2017) 477.

[23] J. Xie, Q. Shen, K. Huang, T. Zheng, L. Cheng, Z. Zhang, Y. Yu, G. Liao, X. Wang, C. Li, Oriented assembly of cell-mimicking nanoparticles via a molecular affinity strategy for targeted drug delivery, ACS nano 13(5) (2019) 5268-5277.

[24] Y. Chen, M. Chen, Y. Zhang, J.H. Lee, T. Escajadillo, H. Gong, R.H. Fang, W. Gao, V. Nizet, L. Zhang, Broad‐spectrum neutralization of pore‐forming toxins with human erythrocyte membrane‐coated nanosponges, Advanced healthcare materials 7(13) (2018) 1701366.

[25] S. Wang, D. Wang, Y. Duan, Z. Zhou, W. Gao, L. Zhang, Cellular Nanosponges for Biological Neutralization, Advanced Materials 34(13) (2022) 2107719.

[26] J.A. Copp, R.H. Fang, B.T. Luk, C.-M.J. Hu, W. Gao, K. Zhang, L. Zhang, Clearance of pathological antibodies using biomimetic nanoparticles, Proceedings of the National Academy of Sciences 111(37) (2014) 13481-13486.

[27] Z. Pang, C.-M.J. Hu, R.H. Fang, B.T. Luk, W. Gao, F. Wang, E. Chuluun, P. Angsantikul, S. Thamphiwatana, W. Lu, Detoxification of organophosphate poisoning using nanoparticle bioscavengers, ACS nano 9(6) (2015) 6450-6458.

[28] M. Holinstat, Normal platelet function, Cancer and Metastasis Reviews 36(2) (2017) 195-198.

[29] C.-M.J. Hu, R.H. Fang, K.-C. Wang, B.T. Luk, S. Thamphiwatana, D. Dehaini, P. Nguyen, P. Angsantikul, C.H. Wen, A.V. Kroll, Nanoparticle biointerfacing by platelet membrane cloaking, Nature 526(7571) (2015) 118-121.

[30] J. Li, P. Angsantikul, W. Liu, B. Esteban‐Fernández de Ávila, X. Chang, E. Sandraz, Y. Liang, S. Zhu, Y. Zhang, C. Chen, Biomimetic Platelet‐Camouflaged Nanorobots for Binding and Isolation of Biological Threats, Advanced Materials 30(2) (2018) 1704800.

[31] J.-K. Kim, S. Uchiyama, H. Gong, A. Stream, L. Zhang, V. Nizet, Engineered biomimetic platelet membrane-coated nanoparticles block staphylococcus aureus cytotoxicity and protect against lethal systemic infection, Engineering 7(8) (2021) 1149-1156.

[32] X. Wei, J. Gao, R.H. Fang, B.T. Luk, A.V. Kroll, D. Dehaini, J. Zhou, H.W. Kim, W. Gao, W. Lu, Nanoparticles camouflaged in platelet membrane coating as an antibody decoy for the treatment of immune thrombocytopenia, Biomaterials 111 (2016) 116-123.

[33] J.C. Rieckmann, R. Geiger, D. Hornburg, T. Wolf, K. Kveler, D. Jarrossay, F. Sallusto, S.S. Shen-Orr, A. Lanzavecchia, M. Mann, Social network architecture of human immune cells unveiled by quantitative proteomics, Nature immunology 18(5) (2017) 583-593.

[34] S. Thamphiwatana, P. Angsantikul, T. Escajadillo, Q. Zhang, J. Olson, B.T. Luk, S. Zhang, R.H. Fang, W. Gao, V. Nizet, Macrophage-like nanoparticles concurrently absorbing endotoxins and proinflammatory cytokines for sepsis management, Proceedings of the national academy of

sciences 114(43) (2017) 11488-11493.

[35] S. Shen, F. Han, A. Yuan, L. Wu, J. Cao, J. Qian, X. Qi, Y. Yan, Y. Ge, Engineered nanoparticles disguised as macrophages for trapping lipopolysaccharide and preventing endotoxemia, Biomaterials 189 (2019) 60-68.

[36] M. Shi, K. Shen, B. Yang, P. Zhang, K. Lv, H. Qi, Y. Wang, M. Li, Q. Yuan, Y. Zhang, An electroporation strategy to synthesize the membrane-coated nanoparticles for enhanced anti-inflammation therapy in bone infection, Theranostics 11(5) (2021) 2349.

[37] Z. Ou, H. Zhong, L. Zhang, M. Deng, W. Zhang, J. Wang, H. Feng, J. Gong, C. Miao, Z. Yi, Macrophage membrane-coated nanoparticles alleviate hepatic ischemia-reperfusion injury caused by orthotopic liver transplantation by neutralizing endotoxin, International Journal of Nanomedicine (2020) 4125-4138.

[38] C. Yin, Q. Zhao, W. Li, Z. Zhao, J. Wang, T. Deng, P. Zhang, K. Shen, Z. Li, Y. Zhang, Biomimetic anti-inflammatory nano-capsule serves as a cytokine blocker and M2 polarization inducer for bone tissue repair, Acta Biomaterialia 102 (2020) 416-426.

[39] C. Gao, Q. Huang, C. Liu, C.H. Kwong, L. Yue, J.-B. Wan, S.M. Lee, R. Wang, Treatment of atherosclerosis by macrophage-biomimetic nanoparticles via targeted pharmacotherapy and sequestration of proinflammatory cytokines, Nature communications 11(1) (2020) 2622.

[40] Q. Zhang, D. Dehaini, Y. Zhang, J. Zhou, X. Chen, L. Zhang, R.H. Fang, W. Gao, L. Zhang, Neutrophil membrane-coated nanoparticles inhibit synovial inflammation and alleviate joint damage in inflammatory arthritis, Nature nanotechnology 13(12) (2018) 1182-1190.

[41] G. Zhang, G.R. Campbell, Q. Zhang, E. Maule, J. Hanna, W. Gao, L. Zhang, S.A. Spector, CD4+ t cell-mimicking nanoparticles broadly neutralize hiv-1 and suppress viral replication through autophagy, MBio 11(5) (2020) 10.1128/mbio. 00903-20.

[42] Q. Zhang, A. Honko, J. Zhou, H. Gong, S.N. Downs, J.H. Vasquez, R.H. Fang, W. Gao, A. Griffiths, L. Zhang, Cellular nanosponges inhibit SARS-CoV-2 infectivity, Nano letters 20(7) (2020) 5570-5574.

[43] L. Rao, S. Xia, W. Xu, R. Tian, G. Yu, C. Gu, P. Pan, Q.-F. Meng, X. Cai, D. Qu, Decoy nanoparticles protect against COVID-19 by concurrently adsorbing viruses and inflammatory cytokines, Proceedings of the National Academy of Sciences 117(44) (2020) 27141-27147.

[44] Y. Zhang, Y. Chen, C. Lo, J. Zhuang, P. Angsantikul, Q. Zhang, X. Wei, Z. Zhou, M. Obonyo, R.H. Fang, Inhibition of pathogen adhesion by bacterial outer membrane‐coated nanoparticles, Angewandte Chemie International Edition 58(33) (2019) 11404-11408.

[45] R.H. Fang, C.-M.J. Hu, K.N.H. Chen, B.T. Luk, C.W. Carpenter, W. Gao, S. Li, D.-E. Zhang, W. Lu, L. Zhang, Lipid-insertion enables targeting functionalization of erythrocyte membrane-cloaked nanoparticles, Nanoscale 5(19) (2013) 8884-8888.

[46] X. Ai, S. Wang, Y. Duan, Q. Zhang, M.S. Chen, W. Gao, L. Zhang, Emerging approaches to

functionalizing cell membrane-coated nanoparticles, Biochemistry 60(13) (2020) 941-955.

[47] Q. Jiang, Y. Liu, R. Guo, X. Yao, S. Sung, Z. Pang, W. Yang, Erythrocyte-cancer hybrid membrane-camouflaged melanin nanoparticles for enhancing photothermal therapy efficacy in tumors, Biomaterials 192 (2019) 292-308.

[48] C. Ding, C. Zhang, S. Cheng, Y. Xian, Multivalent aptamer functionalized Ag2S nanodots/hybrid cell membrane-coated magnetic nanobioprobe for the ultrasensitive isolation and detection of circulating tumor cells, Advanced functional materials 30(16) (2020) 1909781.

[49] C. Chi, F. Li, H. Liu, S. Feng, Y. Zhang, D. Zhou, R. Zhang, Docetaxel-loaded biomimetic nanoparticles for targeted lung cancer therapy in vivo, Journal of nanoparticle research 21(7) (2019) 144.

[50] X. Ai, D. Wang, A. Honko, Y. Duan, I. Gavrish, R.H. Fang, A. Griffiths, W. Gao, L. Zhang, Surface glycan modification of cellular nanosponges to promote SARS-CoV-2 inhibition, Journal of the american chemical society 143(42) (2021) 17615-17621.

[51] P. Angsantikul, S. Thamphiwatana, Q. Zhang, K. Spiekermann, J. Zhuang, R.H. Fang, W. Gao, M. Obonyo, L. Zhang, Coating nanoparticles with gastric epithelial cell membrane for targeted antibiotic delivery against Helicobacter pylori infection, Advanced therapeutics 1(2) (2018) 1800016.

[52] P. Lv, X. Liu, X. Chen, C. Liu, Y. Zhang, C. Chu, J. Wang, X. Wang, X. Chen, G. Liu, Genetically engineered cell membrane nanovesicles for oncolytic adenovirus delivery: a versatile platform for cancer virotherapy, Nano letters 19(5) (2019) 2993-3001.

[53] S. Krishnamurthy, P. Muthukumaran, M.K.G. Jayakumar, D. Lisse, N.D. Masurkar, C. Xu, J.M. Chan, C.L. Drum, Surface protein engineering increases the circulation time of a cell membrane-based nanotherapeutic, Nanomedicine: nanotechnology, biology and medicine 18 (2019) 169-178.

[54] M.J.H. Gerritzen, D.E. Martens, R.H. Wijffels, L. van der Pol, M. Stork, Bioengineering bacterial outer membrane vesicles as vaccine platform, Biotechnology advances 35(5) (2017) 565-574.

[55] J.H. Park, Y. Jiang, J. Zhou, H. Gong, A. Mohapatra, J. Heo, W. Gao, R.H. Fang, L. Zhang, Genetically engineered cell membrane–coated nanoparticles for targeted delivery of dexamethasone to inflamed lungs, Science advances 7(25) (2021) eabf7820.

[56] H. Peng, Z. Xu, Y. Wang, N. Feng, W. Yang, J. Tang, Biomimetic mesoporous silica nanoparticles for enhanced blood circulation and cancer therapy, ACS applied bio materials 3(11) (2020) 7849-7857.

[57] C.-M.J. Hu, R.H. Fang, K.-C. Wang, B.T. Luk, S. Thamphiwatana, D. Dehaini, P. Nguyen, P. Angsantikul, C.H. Wen, A.V. Kroll, C. Carpenter, M. Ramesh, V. Qu, S.H. Patel, J. Zhu, W. Shi, F.M. Hofman, T.C. Chen, W. Gao, K. Zhang, S. Chien, L. Zhang, Nanoparticle biointerfacing by platelet membrane cloaking, Nature 526(7571) (2015) 118-121.

[58] E. Ben-Akiva, R.A. Meyer, H. Yu, J.T. Smith, D.M. Pardoll, J.J. Green, Biomimetic anisotropic polymeric nanoparticles coated with red blood cell membranes for enhanced circulation and toxin removal, Science advances 6(16) (2020) eaay9035.

[59] J.-G. Piao, L. Wang, F. Gao, Y.-Z. You, Y. Xiong, L. Yang, Erythrocyte membrane is an alternative coating to polyethylene glycol for prolonging the circulation lifetime of gold nanocages for photothermal therapy, ACS nano 8(10) (2014) 10414-10425.

[60] H. Gong, F. Chen, Z. Huang, Y. Gu, Q. Zhang, Y. Chen, Y. Zhang, J. Zhuang, Y.-K. Cho, R.H. Fang, W. Gao, S. Xu, L. Zhang, Biomembrane-modified field effect transistors for sensitive and quantitative detection of biological toxins and pathogens, ACS nano 13(3) (2019) 3714-3722.

[61] W. Chen, Q. Zhang, B.T. Luk, R.H. Fang, Y. Liu, W. Gao, L. Zhang, Coating nanofiber scaffolds with beta cell membrane to promote cell proliferation and function, Nanoscale 8(19) (2016) 10364-70.

[62] W.-L. Liu, M.-Z. Zou, T. Liu, J.-Y. Zeng, X. Li, W.-Y. Yu, C.-X. Li, J.-J. Ye, W. Song, J. Feng, X.-Z. Zhang, Expandable immunotherapeutic nanoplatforms engineered from cytomembranes of hybrid cells derived from cancer and dendritic cells, Advanced materials 31(18) (2019) 1900499.

Chapter 2 Neuronal cell membrane coated nanoparticles for detoxification of neurotoxins

2.1 Introduction

Neurotoxins are an extensive group of chemical and biological compounds that inhibit or destroy the proper functions of the nervous system. [1, 2] Some neurotoxins impair nerve signal transmission by binding with voltage-dependent ion channels and disrupting the channel functions. [3, 4] Some bind with neuron surface receptors, initiating cellular processes that block synaptic vesicle release and neuron communications. [5, 6] Some act as agonists or antagonists of the neuron membrane receptors, inhibiting regular neurotransmitter binding and signal transmission. [7, 8] Numerous types of neurotoxins, together with their close association with bacterial infection, animal envenomation, and bioweaponry, cause serious public health concerns and security threats, underscoring the importance of developing effective detoxification strategies against neurotoxins. [9-11]

Currently, neutralizing antibodies represent the primary detoxification approach against neurotoxins. [12] However, antibody development requires the identification and isolation of target toxins. Given the enormous diversity of neurotoxins, neutralizing antibody development has been lagging. In addition, antibodies developed for individual neurotoxins often show highly variable cross-reactivity among congeners, and such cross-reactivity is typically associated with degeneracy and mimicry in immune recognition that reduces the potency. [13] Therefore, a cocktail of antibodies is necessary to cover the wide range of toxic congeners, and the cross-reactivity with less potent congeners often reduces the effectiveness. [14] The difficulties are further exacerbated by toxin profiles in natural sources that vary geographically or change under different [15] environmental conditions. [16] As a result, the efficacy of antibody cocktails remains highly limited. [17] Other antitoxin platforms that rely on toxin structure as the design

cue, such as small molecule inhibitors, also suffer from restricted selectivity against enormously diverse neurotoxins. [18, 19]

Recently, "cellular nanosponges" or CNPs, referring to nanoparticles made by coating natural cell membranes onto synthetic nanoparticle cores, have emerged as an attractive broad-spectrum detoxification strategy. [20, 21] The hallmark of this detoxification strategy is the host cell mimicry that allows nanoparticles to act as host cell decoys and intercept harmful toxins regardless of the toxin's molecular structure and mechanism of action. The CNPs strategy focuses on host cells instead of causative toxins for detoxification, and thus, it can overcome the challenge of toxin diversity. By choosing an appropriate type of cell membrane that is susceptible to a group of toxins, the resulting cellular CNPs can ensure specificity against that group of toxins for detoxification. Following the early success of using CNPs to detoxify bacterial toxins, [22, 23] the technology has also shown effective binding and neutralization against numerous harmful agents such as small molecule toxicants, [24, 25] autoimmune antibodies, [26] inflammatory cytokines, [27] bacteria, [28] and viruses. [29]

2.2 Results and discussion

2.2.1 Preparation and characterization

Neurotoxins must bind with neuronal membrane-associated receptors for bioactivity despite their enormous structural diversity. Such a shared property motivated us to develop neuronal membrane-coated CNPs (denoted "Neuron-NS") as a function-based detoxification platform. To fabricate Neuron-NS, we choose Neuro-2a cells, a mouse neural crest-derived cell line, as a model cell line to fabricate Neuron-NS since this cell line has been extensively used for neurotoxin studies (Figure 2.1). We first derived a neuronal membrane from Neuro-2a cells by using an established process that involved mechanical disruption and differential centrifugation.

[30, 31] Meanwhile, we prepared polymeric cores using poly(lactic-co-glycolic) acid (PLGA) through a nanoprecipitation method. Lastly, we coated the neuronal membrane onto the PLGA cores with sonication.

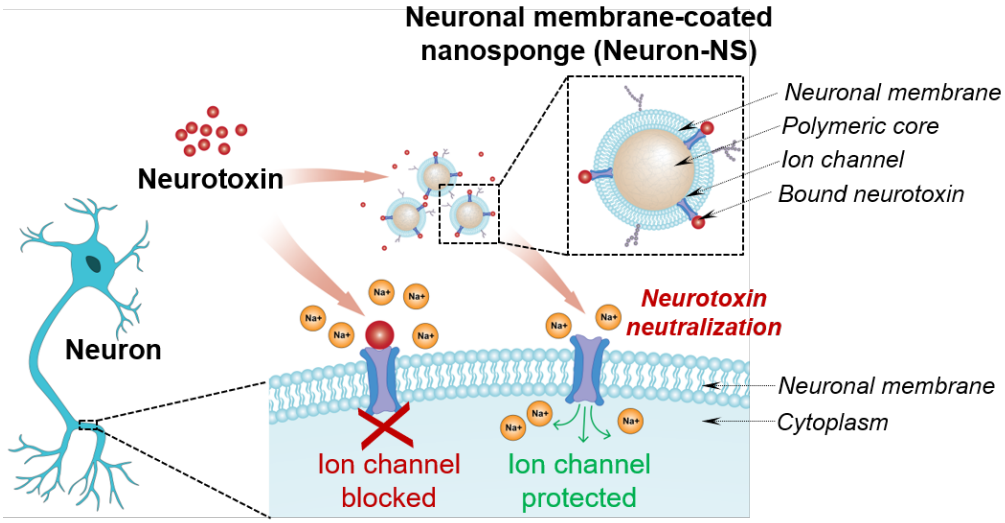

Figure 2.1 Schematic of neuronal membrane-coated nanoparticles.
Neuron-NS are constructed by coating polymeric nanoparticle cores with natural neuronal membrane. Neuron-NS can function as decoys of source neurons, bind with neurotoxins, and divert them away from attacking the neurons.

The membrane coating led to an increase in the diameter and a less negative surface ζ potential from the PLGA cores, suggesting the addition of a lipid bilayer membrane shell onto the polymeric cores (Figure 2.2A). [32] When visualized with transmission electron microscopy (TEM), Neuron-NS showed a spherical core−shell structure (Figure 2.2B). The shell thickness was comparable to that of a single lipid bilayer. When suspended in 1× PBS, the size of Neuron-NS remained unchanged within 48 h, indicating high colloidal stability (Figure 2.2C). The presence of voltage-gated sodium channels was confirmed with antibody staining. We also examined the sidedness of Neuron-NS. The right-side-out membrane orientation was confirmed by comparing the level of neural cell adhesion molecule (NCAM) on Neuron-NS and on the source Neuro-2a cells containing an equal amount of membrane proteins (Figure 2.2D).

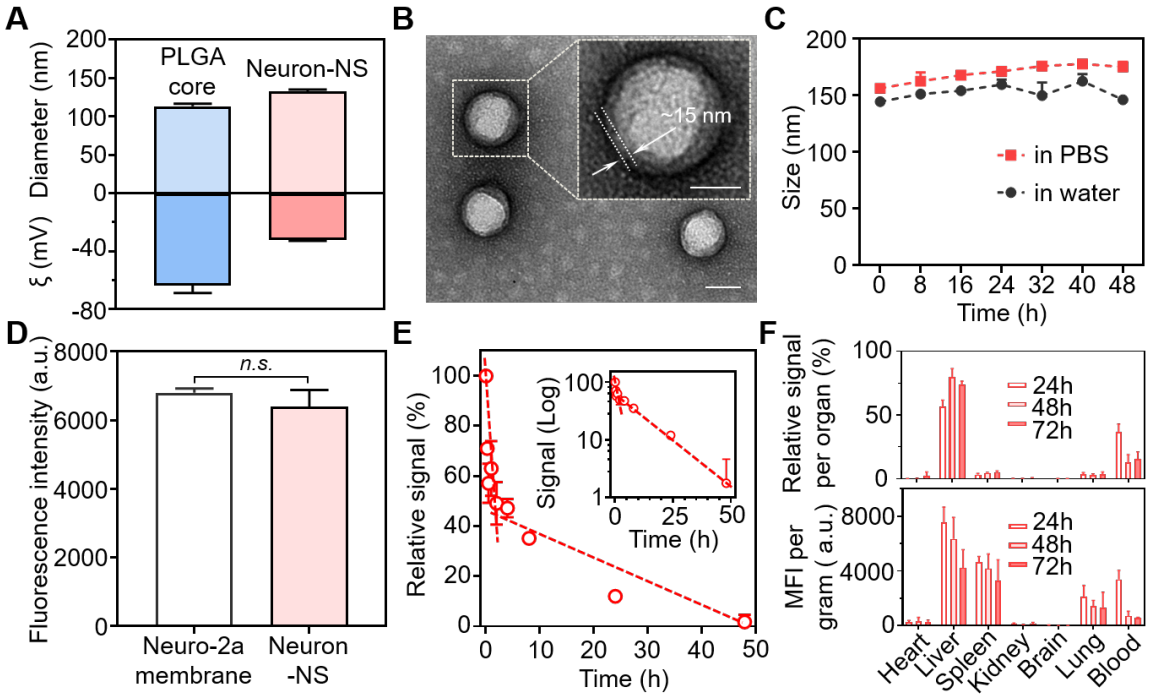

Figure 2.2 Characterization of Neuron-NS.

Characterization of Neuron-NS. (A) Neuron-NS were made with the membrane of Neuro-2a cells. Their hydrodynamic size (diameter, nm) and surface zeta potential (ζ, mV) were measured with dynamic light scattering (DLS). (B) A representative image of Neuron-NS examined with transmission electron microscopy (TEM). (Scale bar: 100 nm.) Inset: the zoomed-in view of a single Neuron-NS. (Scale bar: 50 nm.) Samples were stained with uranyl acetate. (C) Neuron-NS stability in 1X PBS or water measured with DLS for their sizes over 48 h. (D) Comparison of fluorescence intensity measured from Neuro-2a cells (100 μL, approximately 2 × 106 cells) and Neuron-NS (100 μL of suspension, 0.4 mg/mL protein content) containing equivalent amounts of the cell membrane. The samples were stained with Alexa 488-labeled anti-mouse neural cell adhesion molecule 1 (NCAM-1) antibody. MFI: mean fluorescence intensity; n.s.: not significant. (E) Neuron-NS, labeled with DiD were injected intravenously into mice through the tail vein. At different time points, blood was collected and measured for fluorescence to evaluate the systemic circulation lifetime of the Neuron-NS. Inset: the semilog plot of fluorescence signal at different time points. Statistical analysis was performed using a paired two-tailed t-test. Data presented as mean + s.d. In all datasets, n = 3 independent experiments using the same batch of Neuron-NS. (F) Biodistribution profile of Neuron-NS measured by intravenously injecting DiD-labeled Neuron-NS into mice. At 24, 48, and 72 h time points, the organs from a randomly grouped subset of mice were collected, homogenized, and quantified for fluorescence. Fluorescence intensity per gram of tissue and relative signal per organ were compared (n = 6)

To examine the pharmacokinetics of Neuron-NS, we labeled the CNPs with a fluorescent dye and injected them into mice through the tail vein. As shown in Figure 2.2E, the Neuron-NS

signal from the blood decreased steeply in the first 2 h after the injection but more gradually after the 2 h time point. Based on a two-compartment model, an elimination half-life was calculated to be about 14.9 h. [33] The organ distribution of Neuron-NS was also analyzed at 24, 48, and 72 h time points following systemic administration. When the signal was normalized to the organ weight, Neuron-NS were largely retained in the liver and spleen, two primary organs of the reticuloendothelial system (RES, Figure 2.2F). When analyzed for distribution per organ, Neuron-NS were largely distributed in the blood and the liver. Meanwhile, a significant level of Neuron-NS was also found in the blood. As the level of Neuron-NS in blood decreased with time, the level in the liver increased accordingly. This distribution pattern implied an uptake of these CNPs by the RES over the study period.

2.2.2 Neuron-NS neutralize TTX in a cytotoxicity assay

After fabricating the Neuron-NS, we examined their neutralization capacity against TTX in a cytotoxicity assay. [34, 35] The study has three steps. In the first step, we incubated the cells with a veratridine (VTD) and ouabain (O) mixture. VTD opens the voltage-gated sodium channel (VGSC), enhancing Na^+ influx into the cells. This process was exacerbated by O, which prevents Na+ efflux by blocking the action of Na^+/K^+-ATPase. Our study showed that the viability of Neuro-2a cells reduced as the VTD and O concentrations increased (Figure 2.3A). A VTD concentration of 50 μM and an O concentration of 1 mM were chosen for the subsequent studies. We added TTX into the VTD and O mixture in the second step. TTX was reported to block VGSC, inhibiting VTD- and O-induced Na+ influx and the associated cytotoxicity. Indeed, in our study, cell viability recovered as the TTX dosage increased, reaching a maximum of approximately 40% with a TTX concentration of 50 nM (Figure 2.3B). In the third step, we allowed a fixed initial concentration of TTX to incubate with Neuron-NS before mixing with

VTD and O. As shown in Figure 2.3C, increasing Neuron-NS concentration led to a dose-dependent decrease of Neuro-2a cell viability. Such a correlation indicated that TTX was neutralized by the Neuron-NS, which prevented TTX from suppressing VTD- and O-induced cytotoxicity. Under our experimental conditions, 10 mg/mL Neuron-NS effectively neutralized 50 nM TTX, as the CNPs at this concentration were able to fully reverse cell viability recovery induced by TTX. In contrast, CNPs made with red blood cell membrane or macrophage membrane were unable to neutralize TTX, suggesting that the neutralization is due to specific proteins in the neuronal membrane. We also found that incubating Neuron-NS with saxitoxin, a potent blocker against the voltage-gated sodium channel, demolished their neutralization capability against TTX. These results indicate that Neuron-NS neutralizing TTX is likely through their voltage-gated sodium channels in the neuronal membrane.

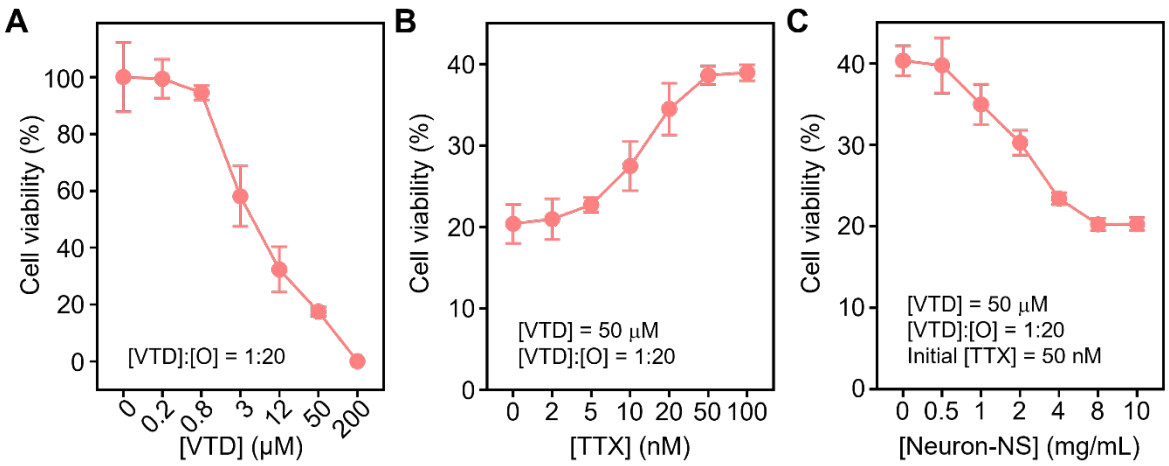

Figure 2.3 Neuron-NS neutralize TTX in a cytotoxicity assay.

(A) Cell viability measured from Neuro-2a cells incubated with the mixture of veratridine (VTD) and ouabain (O). The molar concentration of VTD to O was 1:20. The mixture caused cytotoxicity to Neuro-2a cells in a concentration-dependent manner. (B) Cell viability measured from Neuro-2a cells incubated with the mixture of VTD, O, and TTX. VTD was kept at 50 μM and O was kept at 1 mM. TTX prevented the cytotoxicity induced by VTD and O in a dose-dependent manner. (C) Cell viability measured from Neuro-2a cells incubated with the mixture of VTD, O, and Neuron-NS-treated TTX. VTD was kept at 50 μM and O was kept at 1 mM. TTX initial concentration was 50 nM. Neuron-NS neutralized TTX, resulting in a dose-dependent decrease in cell viability. Data presented as mean ± s.d. In all datasets, n = 3 independent experiments using the same batch of Neuron-NS.

2.2.3 Neuron-NS neutralize TTX in a calcium flux assay

Next, we used a calcium flux assay to evaluate Neuron-NS for TTX neutralization. [36, 37] As shown in Figure 2.4A, we first loaded Neuro-2a cells with Fluo-4, a Ca^{2+}-sensitive dye, and used these cells as the control. We added VTD to the next group. VTD opened the VGSC, causing a rapid entry of Ca^{2+} into the cells, reflected by a brighter green fluorescence. However, when we treated the cells first with TTX and then added VTD, they maintained a low fluorescence signal comparable to the control group, suggesting that TTX abolished VTD-induced Ca^{2+} influx. We then mixed TTX with Neuron-NS. After removing the CNPs, we added the solution containing unbound TTX to the cells and then added the VTD. We observed the recovery of the green fluorescence, suggesting the neutralization of TTX by Neuron-NS.

To demonstrate the TTX neutralization with Neuron-NS in real-time, we monitored cell fluorescence continuously and plotted the relative fluorescence change ($\Delta F/F_0$) versus time (Figure 2.4B). Herein, F_0 is the mean fluorescence intensity before adding VTD, and ΔF is the fluorescence intensity change at given time points. After 50 s, 1× PBS was added to the cells in the control group. We observed a slight fluorescence increase, likely due to the disturbance when the samples were added to the cells. We next added VTD to the cells and observed a significant fluorescence increase. Such an increase reached a maximum (ΔF_{max}) at 100 s. We then incubated the cells with TTX and then added VTD. This time, the fluorescence change remained low, comparable to that of the control group, suggesting that TTX inhibited VTD from inducing Ca^{2+} influx. We next incubated TTX with the Neuron-NS. After removing the Neuron-NS, we added the solution to the cells and then added VTD. We observed a fluorescence increase to a level comparable to that of the VTD group, suggesting the neutralization of TTX by the CNPs. Using the same experimental setup, we fixed TTX concentration but incubated it with Neuron-NS

ranging from 0 to 40 mg/mL and plotted the maximum fluorescence change($\Delta F_{max}/F_0$) versus Neuron-NS concentration. As shown in Figure 2.4C, Neuron-NS neutralized TTX in a dose-dependent manner.

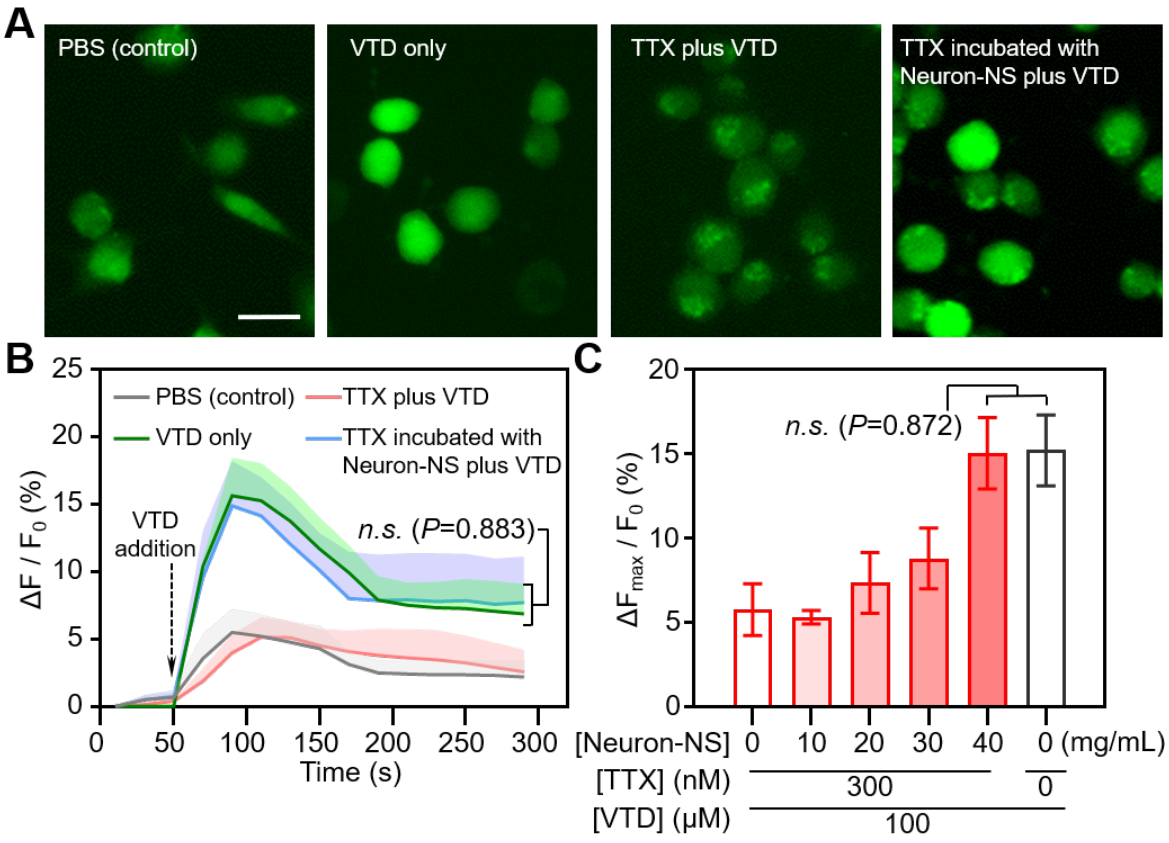

Figure 2.4 Neuron-NS neutralize TTX in a calcium flux assay.

(A) Representative fluorescence images of Neuro-2a cells co-incubated with Fluo-4, a Ca^{2+} sensitive dye. Cells were exposed to PBS (control), VTD only, TTX plus VTD, and TTX incubated with Neuron-NS plus VTD. (B) Timelapse fluorescence change of Neuro-2a cells as an indication of Ca^{2+} influx after adding various concentrations of VTD. F_0 is the mean fluorescence intensity of the cells without VTD. ΔF is the difference between the fluorescence intensity at given time points and F_0. (C) Neuron-NS neutralize TTX, reflected by a dose-dependent recovery of VTD-induced Ca^{2+} influx in Neuro-2a cells. ΔF_{max} is the maximum increase of fluorescence intensity due to Ca^{2+} influx. Data presented as mean ± s.d. In (A-C), VTD was 100 μM and TTX was 300 nM; in (A-B), Neuron-NS was 40 mg/mL; n.s.: not significant; statistical analysis by paired t-test. In all datasets, n = 3 independent experiments using the same batch of Neuron-NS.

2.2.4 Neuron-NS neutralize TTX in a cell osmotic swelling assay

We further tested Neuron-NS for their ability to neutralize TTX in a cell osmotic swelling assay. [38, 39] As shown in Figure 2.5A, Neuro-2a cells exhibited a typical ellipsoidal shape with short neuritis under normal culture conditions. However, a mixture of VTD and O added to the culture elicited swelling and rounding up of the cells. Such a morphology change is due to a combined effect of VTD and O. Specially, VTD opens VGSC, causing uncontrolled Na^+ influx, and O inhibits Na^+/K^+-ATPase that would otherwise keep intracellular Na^+ concentration low. TTX is known to counteract the effects of VTD and O by blocking VGSC.

When cells were treated with the mixture of TTX, VTD, and O, they maintained their typical morphology. We then incubated TTX with Neuron-NS. After removing the Neuron-NS, we mixed the remaining TTX with VTD and O and added the mixture to the cells. This time, we observed cell rounding similar to the morphology when VTD and O were added without TTX. This experiment further demonstrated the neutralization of TTX by Neuron-NS. Based on this observation, we quantified TTX neutralization with Neuron-NS by measuring the cell roundness factor defined as $4\pi \times \text{area/perimeter2}$. A cell roundness factor value closer to zero indicates a more elongated morphology, whereas a value closer to 1 indicates a more rounded morphology. As shown in Figure 2.5B, the roundness factor of Neuro-2a cells increased with VTD/O concentrations, indicating a dose-dependent cell rounding. The roundness factor reached a plateau when the VTD concentration was higher than 25 μM (or when the O concentration was higher than 500 μM; VTD/O = 1/20). We then mixed VTD/O at these concentrations with various concentrations of TTX.

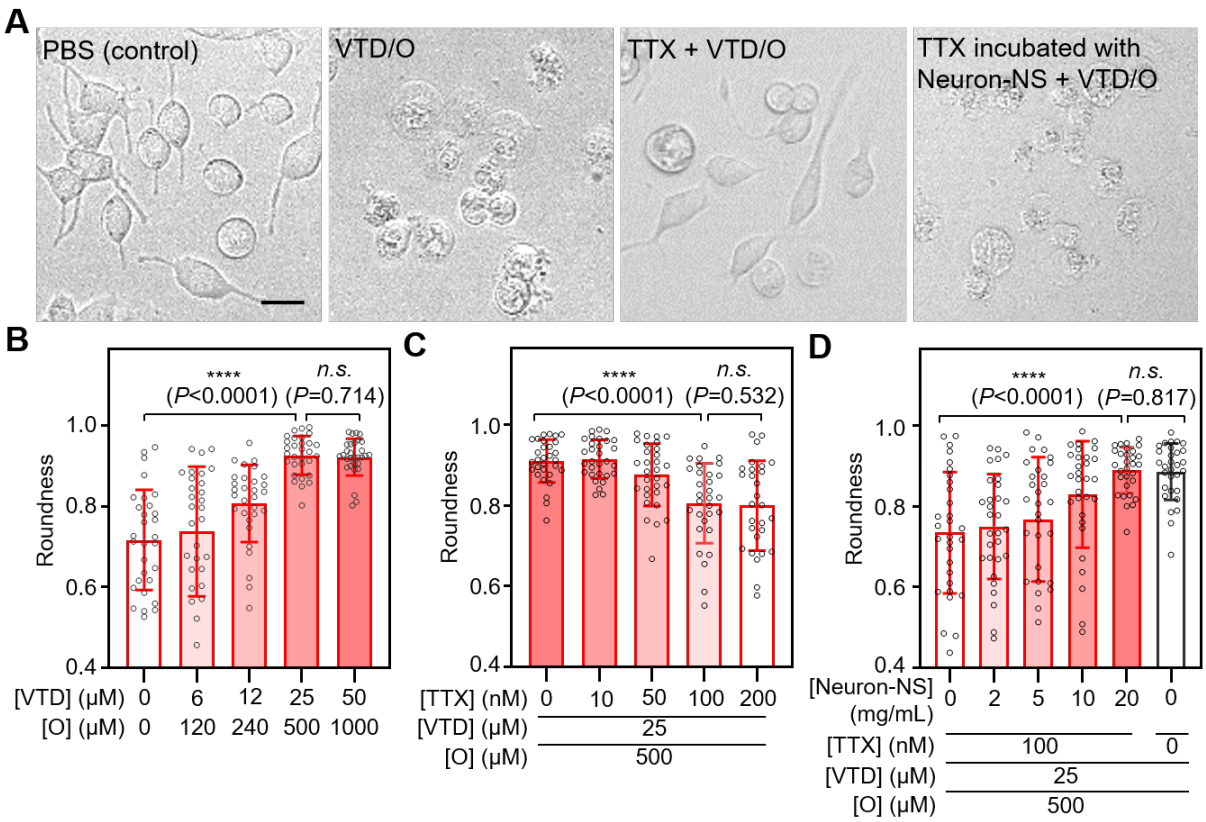

Figure 2.5 Neuron-NS neutralize TTX in a cell osmotic swelling assay.

(A) Representative images of Neuro-2a cells exposed to 1X PBS, mixture of VTD/O, mixture of TTX and VTD/O, and mixture of TTX incubated with Neuron-NS and VTD/O, respectively. Scale bar = 20 μm. (B) Comparison of the roundness among Neuro-2a cells treated with different concentrations of VTD/O. The molar ratio of VTD/O concentrations was kept at 1:20. (C) Comparison of the roundness among Neuro-2a cells treated with mixtures containing VTD/O and various concentrations of TTX. The concentration of VTD was 25 μM and the concentration of O was 500 μM. (D) Comparison of the roundness among Neuro-2a cells added with the mixture of VTD/O and TTX incubated with various concentrations of Neuron-NS. The concentration of VTD was 25 μM and O was 500 μM. Initial TTX concentration was 100 nM before mixing and incubation with different concentrations of Neuron-NS. Data presented as mean ± s.d. *n.s.*: not significant; statistical analysis by paired *t*-test. All experiments used the same batch of Neuron-NS.

When the mixture was added to the cells, the value of the roundness factor decreased as the TTX concentration increased, indicating the inhibition of cell rounding (Figure 2.5C). The value of the cell roundness factor reached a plateau when TTX concentration was higher than 100 nM. Lastly, we incubated 100 nM TTX with different concentrations of Neuron-NS. After

removing the CNPs, we mixed unbound TTX with VTD/O and added the mixture to the cells. As shown in Figure 2.5D, when the Neuron-NS concentration increased, the roundness factor increased accordingly, indicating TTX neutralization by Neuron-NS in a dose-dependent manner. When the Neuron-NS reached 20 mg/mL, the roundness factor became comparable to that of cells treated with VTD/O but without TTX, indicating a complete neutralization of 100 nM TTX by 20 mg/mL Neuron-NS.

2.2.5 Neuron-NS neutralize TTX in vivo

Next, we examined the efficacy of Neuron-NS for neutralizing TTX in vivo. In the study, we injected TTX subcutaneously and tested a range of TTX dosages (Figure 2.6A). We selected the dosage of 9.5 μg/kg to perform the in vivo efficacy study. At this dosage, two-thirds of the mice died from TTX intoxication within 40 min. Using this dosage, we first tested Neuron-NS efficacy in a treatment regimen, where TTX was administered subcutaneously, followed by a single intravenous injection of Neuron-NS. We did not observe a survival benefit when the mouse group received 20 mg/kg Neuron-NS (Figure 2.6B). However, when the Neuron-NS dosage was increased to 40 mg/kg, the survival rate also increased from 70% to 80%. All mice survived when the dosage was further increased to 80 mg/kg. To further demonstrate Neuron-NS efficacy, we also conducted the test in a preventative regimen, where Neuron-NS was first injected into mice intraperitoneally, followed by a single subcutaneous injection of TTX at the dosage of 9.5 μg/kg. In this experiment, mice injected with 50, 100, and 200 mg/kg Neuron-NS showed 70%, 80%, and 100% survival rates, respectively, demonstrating a dose-dependent survival benefit (Figure 2.6C). Overall, the tests in both treatment and preventative regimens showed effective protection from Neuron-NS against TTX intoxication in vivo.

2.2.6 In vivo biosafety of Neuron-NS

Finally, we evaluated the acute toxicity of Neuron-NS after in vivo administration in mice. Neuron-NS were injected intravenously through the tail vein into the mice at a dosage of 80 mg/kg. We first examined red blood cell, platelet, and white blood cell counts 24 h after the Neuron-NS administration. Their values were comparable to the baseline levels (Figure 2.7A).

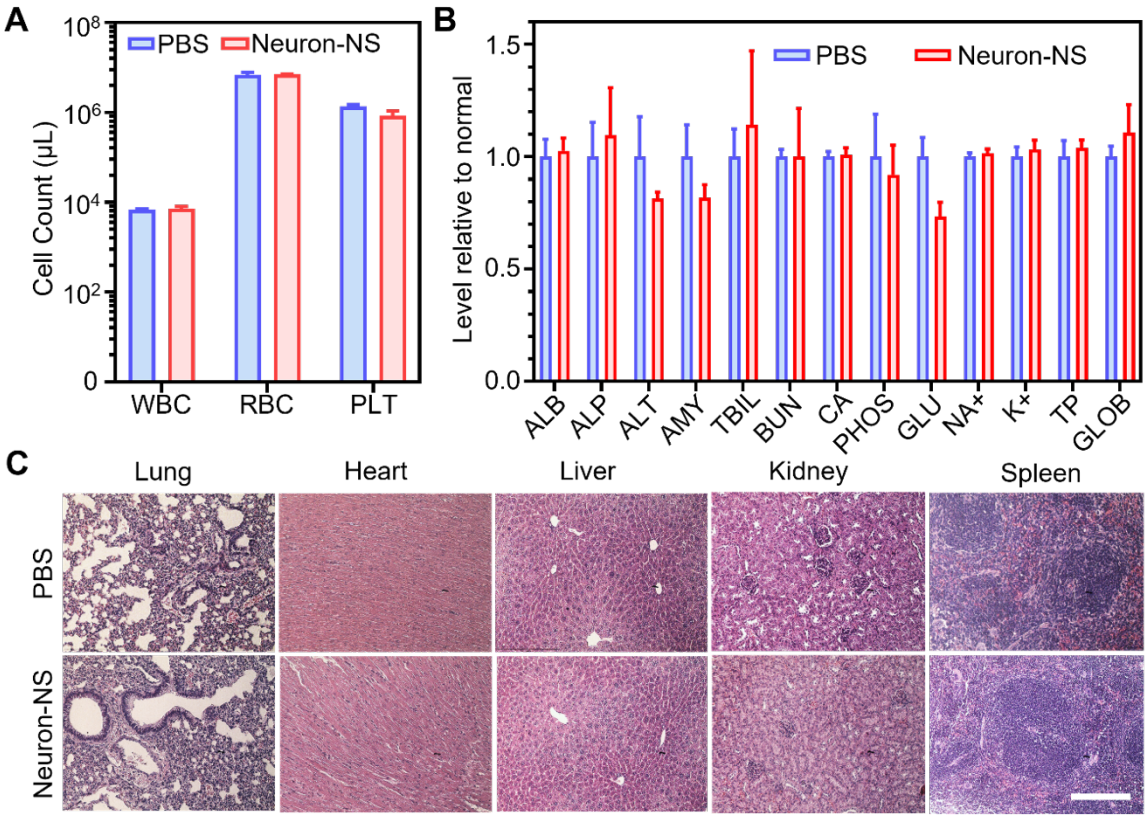

Figure 2.6 In vivo biosafety of Neuron-NS.

(A) Counts of various blood cells 24h after intravenous injection of PBS or Neuron-NS (n = 3; data represents geometric mean + SD). WBC, white blood cells; RBC, red blood cells; PLT, platelets. (B) Blood biochemistry panel analysis after 24h administration of PBS or Neuron-NS intravenously (n = 3; mean + SD). ALB, albumin; ALP, alkaline phosphatase; ALT, alanine transaminase; AMY, amylase; TBIL, total bilirubin; BUN, blood urea nitrogen; CA, calcium; PHOS, phosphorus; GLU, glucose; NA+, sodium; K+, potassium; TP, total protein; GLOP, globulin. (C) H&E staining of histology sections from major organs (lung, heart, liver, kidney, and spleen) one day after PBS or Neuron-NS administration. Scale bar = 250 μm. In (A) and (B), statistical analysis was performed by using the paired Student's t-test, and comparison between PBS and Neuron-NS groups was not statistically significant ($P > 0.05$).

We also tested a panel of additional blood markers shown in Figure 2.7B and found their levels consistent with the baseline levels. Therefore, blood analysis implied short-term safety of Neuron-NS. We also collected the major organs of the mice and performed histopathological analysis. Tissue sections of major organs, including the lungs, heart, liver, kidneys, and spleen, showed no histological lesions compared to those in the control group (Figure 2.7C). These results confirmed the absence of acute toxicity of Neuron-NS.

2.3 Methods

Neuron Membrane Derivation

Neuro-2a cells, a mouse neuroblastoma cell line, were obtained from American Type Culture Collection (ATCC, CCL-131) and cultured in Dulbecco's modified Eagle's medium (DMEM, Corning) supplemented with 10% fetal bovine serum (FBS, Hyclone) and 1% penicillin–streptomycin (Gibco). The cells were maintained at 37 °C with 5% CO_2 in a humidity-controlled incubator. The cells were cultured in T175 culture flasks to full confluency and were detached with trypsin-ethylenediaminetetraacetic acid (EDTA, Hyclone). The cell suspension was centrifuged at 700g for 5 min, and the collected cells were washed three times with 1× phosphate-buffered saline (PBS, Hyclone) with centrifugation at the same settings. After the centrifugation, the supernatant was discarded, and the pellet was suspended in isolation buffer consisting of 100 mM ethylene glycol-bis(2-aminoethyl ether)-N,N,N',N'-tetraacetic acid (EGTA, Sigma) and 100 μL of phosphatase inhibitor and protease inhibitor cocktail (100×, Millipore-Sigma). Cells were then disrupted using a Kinematica Polytron PT 10/35 probe homogenizer (at 70% power and 20 passes). The homogenized solution was centrifuged at 20 k ×g for 25 min at 4 °C. The pellet was discarded, and the supernatant was centrifuged again at 100 k ×g for 35 min at 4 °C. The cell membrane was finally collected as the pellet and washed

twice with 0.2 mM EDTA in water. Membrane protein content was quantified by a bicinchoninic acid (BCA) protein assay kit (Pierce, Thermo Fisher Scientific) and bovine serum albumin (BSA) as a standard reference. Approximately 1×10^8 Neuro-2a cells were able to yield 2 mg of membrane material (protein weight). The membrane was suspended in 0.2 mM EDTA at 4 mg/mL (protein concentration, 1 mg of CNPs $\approx 1 \times 10^{12}$ CNPs) and stored at −80 °C for subsequent studies.

Preparation of Neuron-NS

Neuron-NS were formulated with a two-step process. In the first step, the polymeric nanoparticle core was prepared by a nanoprecipitation process. Specifically, 1 mL of poly(d,l-lactide-co-glycolide) acid (PLGA, 50:50 PLGA, 0.67 dL/g, Lactel Absorbable Polymers) in acetone (10 mg/mL) was added rapidly into 2 mL of DI water. For fluorescently labeled PLGA cores, 1,1'-dioctadecyl-3,3,3',3'-tetramethylindodicarbocyanine perchlorate (DiD, excitation/emission = 644 nm/665 nm; Life Technologies) or 1,1'-dioctadecyl-3,3,3',3'-tetramethylindotricarbocyanine iodide (DiR, excitation/emission = 750 nm/778 nm; Life Technologies) was loaded into the polymeric cores at 0.1 wt %. The solution was stirred under a vacuum aspirator to remove the organic solvent. In the second step, the Neuro-2a cell membrane was mixed with PLGA cores at a polymer-to-membrane protein weight ratio of 1:1. The mixture was then sonicated in a bath sonicator (Thermo Fisher Scientific) for 2 min.

Neuron-NS Physicochemical Characterization

The hydrodynamic diameter and the surface ζ potential of Neuron-NS were measured with dynamic light scattering (DLS, Malvern ZEN 3600 Zetasizer). In the long-term colloidal stability study, nanoparticle suspensions were adjusted to 1× PBS with a 0.5 mg/mL final protein concentration. Samples were stored at 4 °C, and the hydrodynamic diameter was measured every

8 h for 48 h. In the morphological study, nanoparticles were stained with uranyl acetate (0.2 wt %) and visualized using transmission electron spectroscopy (FEI 200 kV Sphera). In the membrane sidedness study, Neuro-2a cells (2×10^6 cells) and Neuron-NS (100 μL, 0.2 mg/mL, membrane protein) containing an equal amount of membrane content were blocked with 2 wt % BSA for 1 h. The cells and Neuron-NS were then incubated with Alexa Fluor 647-conjugated antimouse neural cell adhesion molecule (NCAM, Bio-Techne) for 30 min at 37 °C followed by centrifugation (20 k ×g, 10 min) to pellet the nanoparticles. The fluorescence intensity of the unbound antibody was measured by a plate reader (BioTek Synergy Mx) and was used to calculate the number of antibodies bound to Neuron-NS and Neuro-2a cells.

Animal Care and Injections

All animal studies were approved under the guidelines of the University of California San Diego (UCSD) Institutional Animal Care and Use Committee (IACUC). In all animal studies, 4-week-old ICR mice (Harlan Laboratories, male and female) were used. Mice were housed in an animal facility at UCSD under federal, state, local, and NIH guidelines for animal care. In the study, no inflammation or any abnormal appearance was observed at the sites of injection.

Pharmacokinetics, Biodistribution, and Retention Studies of Neuron-NS

In the pharmacokinetics study, 150 μL of DiD-labeled Neuron-NS (25 mg/kg, protein weight) was injected through the tail vein. At 1, 15, and 30 min and 1, 2, 4, 8, 24, and 48 h after the injection, one drop of blood (∼30 μL) was collected from each mouse via submandibular puncture with heparin (Millipore-Sigma) coated microtubes. Then, 20 μL of blood was mixed with 180 μL of PBS in a 96-well plate for fluorescence measurement with a plate-reader (BioTek Synergy Mx, Agilent). Pharmacokinetic parameters were calculated to fit a two-compartment model. For the biodistribution study, 150 μL of DiD-labeled Neuron-NS (25 mg/kg, protein

concentration) was injected intravenously through the tail vein. At 24, 48, and 72 h after the injection, major organs, including the liver, kidneys, spleen, brain, lungs, heart, and blood, were collected from the mice (n = 3). The collected organs were then weighed and homogenized in 1× PBS for fluorescence measurement with the plate reader.

Neuro-2a Cytotoxicity Assay

Neuro-2a cells were seeded 1 day before the experiment in a 96-well plate (Corning) at a 8000 cells/well density. The plate was maintained under the same conditions as described for cell maintenance. On the day of the experiment, a stock solution of ouabain (O) and veratridine (VTD) in dimethyl sulfoxide (DMSO, Millipore-Sigma) was first made. This stock solution contained 200 mM O and 10 mM VTD. From this stock solution, a working solution of DMEM, containing 4000 μM O, 200 μM VTD, 10% v/v fetal bovine serum (FBS, Thermo Fisher Scientific), and 1% v/v penicillin–streptomycin (PS, Thermo Fisher Scientific), was prepared. Serial dilutions of the working solution containing O at 4, 16, 60, 240, 1000, and 4000 μM or VTD at 0.2, 0.8, 3, 12, 50, and 200 μM were made. After preparing the serial dilutions, the culture medium in the 96-well plate was removed, and 100 μL of the above serial dilutions was added to each well. The plate was then incubated for 24 h followed by a viability test with a 3-(4,5-dimethylthiazol-2-yl)-5-(3-carboxymethoxyphenyl)-2-(4-sulfophenyl)-2H-tetrazolium (MTS) assay (Promega). To study the effect of tetrodotoxin (TTX, R&D Systems) on cytotoxicity, the diluted working solutions containing O at a final concentration of 1000 μM, VTD at a final concentration of 50 μM, and TTX at final concentrations ranging from 0 to 100 nM were added to the cells. Cell viability was measured by following the same procedure as described above. To study how TTX neutralization by Neuron-NS affected the cytotoxicity, 180 μL of Neuron-NS in DMEM was mixed with 180 μL of TTX in DMEM. The concentrations of

Neuron-NS in the mixture ranged from 0 to 10 mg/mL (protein concentration), and the TTX concentration in the mixture was kept at 50 nM. The mixtures were incubated for 1 h, and then, the nanoparticles were removed by using Amicon Ultra-4 centrifugal filters (Millipore, 30 kDa molecular weight cutoff, centrifuged at 6000g for 10 min). Then, 267 μL of the filtrate was mixed with 3 μL of O-VTD DMSO stock solution, 27 μL of FBS, and 3 μL of PS. The mixture contained O with a final concentration of 1 mM and VTD with a final of concentration of 50 μM. Then, 100 μL of the mixture was added to the cells. Cell viability was measured by following the same procedure described above. In all measurements, the viability measured from cells cultured without O, VTD, or TTX was used as 100%.

Neuro-2a Cell Calcium Flux Assay

Neuro-2a cells were seeded in a 96-well tissue culture plate at a density of 1×10^4 cells/well. The plate was cultured for 24 h before the study under the same conditions as described for cell maintenance. On the day of the study, cells were incubated with 4 μM Fluo-4-AM dye (Abcam, excitation/emission = 494 nm/516 nm) in 1× Hank's balanced salt solution (HBSS, Gibco) at 37 °C for 30 min. Then, the cells were washed three times with 1× PBS. For the fluorescence imaging, cells with 100 μL of 1× PBS added were used as the control. To study the effect of VTD, 100 μL of VTD in 1× PBS to a final concentration of 100 μM was added to cells. To study the effect of TTX, 100 μL of TTX in 1× HBSS was added to cells, which were incubated 15 min at room temperature, and then, 100 μL of VTD in 1× PBS was added to a final VTD concentration of 100 μM. To study TTX neutralization with Neuron-NS, 300 nM TTX was mixed with 40 mg/mL Neuron-NS (protein concentration) in 1× HBSS. The mixture was incubated for 1 h; then, the nanoparticles were removed with Amicon Ultra-4 centrifugal filters (Millipore, 30 kDa molecular weight cutoff, centrifuged at 6000g for 10 min). After the

centrifugation, 100 μL of the filtrate containing unbound TTX was added to the cells, which were incubated at room temperature for 15 min. Then, VTD was added into the well to a final concentration of 100 μM. All images were taken with an EVOS inverted microscope (Thermo Fisher Scientific). To collect time-lapse fluorescence images, images were taken every 20 s for 300 s at room temperature. The fluorescence intensity of time-lapse images was calculated with ImageJ. F_0 is the mean baseline fluorescence intensity. ΔF is the fluorescence intensity change at given time points relative to F_0. To study dose-dependent neutralization, 300 nM TTX was incubated with nanoparticles of 0, 10, 20, 30, and 40 mg/mL (protein concentration), separately. ΔFmax is the maximum increase of fluorescence intensity change relative to F_0.

Neuron-NS Cell Osmotic Swelling Assay

Neuro-2a cells were seeded 1 day before the experiment in a 96-well plate (Corning) at a density of 8000 cells/well. The plate was maintained under the same conditions as described for cell maintenance. In the study, cells with 1× PBS added were used as a control group. To induce cell rounding, 500 μM O and 25 μM VTD were added to cells. To study the effect of TTX, 500 μM O, 25 μM VTD, and 100 nM TTX were added to cells. To study TTX neutralization, 100 nM TTX was mixed with 20 mg/mL Neuron-NS (protein concentration). After incubation for 1 h, the nanoparticles were removed by Amicon Ultra-4 centrifugal filters (30 kDa molecular weight cutoff, centrifuged at 6000g for 10 min). The unbound TTX with 500 μM O and 25 μM VTD was added into the wells. In all groups, bright-field images were taken after incubation of the cells for 12 h with the EVOS inverted microscope (Thermo Fisher Scientific). To evaluate VTD and O dose-dependent cell rounding, the final concentrations of VTD were 0, 6, 12, 25, and 50 μM. The final concentrations of O were 120, 240, 500, and 1000 μM. To evaluate TTX dose-dependent inhibition of cell rounding, the final concentrations of TTX were 0, 10, 50, 100, and

200 nM; the VTD final concentration was 25 μM, and the O final concentration was 500 μM. To study dose-dependent neutralization, Neuron-NS with concentrations of 0, 5, 10, 20, and 40 mg/mL (protein concentration) were incubated with 100 nM TTX. The VTD final concentration was 25 μM, and the O final concentration was 500 μM. Bright-field images of the cells were taken with the EVOS microscope and then analyzed with ImageJ to quantify cell roundness. Specifically, the cell roundness was calculated on manually segmented cells using the free-hand tool in ImageJ. In the program, the cell roundness is defined as $4\pi \times \text{area/perimeter}^2$. Values approaching 0 indicate a more elongated cell morphology, whereas values approaching 1 indicate a more circular cell morphology. Three images were used in each group, and 10 cells were analyzed for each image.

In Vivo Treatment of TTX Intoxication with Neuron-NS

In the TTX lethality study, free TTX of various dosages (8–12 μg/kg) was injected subcutaneously into ICR mice (n = 10 mice per group). Mice were observed for 24 h, and the survival time was recorded. To examine the neutralization effect of Neuron-NS, TTX (9.5 μg/kg) was first injected subcutaneously (injection volume = 0.2 mL, n = 10 mice per group). After 1 min of TTX injection, various dosages of Neuron-NS were injected intravenously (injection volume = 0.2 mL). Mice were observed for 24 h, and their survival time was recorded.

In Vivo Prevention of TTX Intoxication with Neuron-NS

To examine the efficacy of preventing TTX intoxication, ICR mice (n = 10 mice per group) were first injected with Neuron-NS at various dosages through intraperitoneal administration (injection volume: 0.5 mL). 2 min after the administration of Neuron-NS, mice were injected with TTX at 9.5 μg/kg subcutaneously. The experiment was terminated 24 h after the TTX injection. Mice were observed for 24 h, and their survival time was recorded.

Neuron-NS Safety Evaluation

In the study, Neuron-NS (10 mg/mL, protein concentration) were injected intravenously through the tail vein into the mice at a dosage of 80 mg/kg (n = 3 mice). At 24 h after the injection, approximately 250 μL of whole blood was collected into Eppendorf tubes and allowed to coagulate. Then, the samples were centrifuged at 2000g for 6 min to collect serum for the comprehensive metabolic panel analysis. Meanwhile, 100 μL of the whole blood was collected into an EDTA-coated microtube for the complete blood count. All blood samples were tested at the UCSD Animal Care Program Diagnostic Services Laboratory. Immediately after blood collection, mice were euthanized to collect major organs, including the lungs, heart, liver, kidneys, and spleen. Organs were fixed in 10% formalin (Fisher Scientific), sectioned, and stained with hematoxylin and eosin (H&E) for histological analysis. Histology slides were imaged with a Micromaster II microscope (Fisher Scientific)

2.4 Conclusion

In summary, we derived the membrane of neuronal cells and coated it onto polymeric nanoparticles, forming Neuron-NS for neurotoxin detoxification. Using cell-based assays, we showed that Neuron-NS neutralized TTX, effectively reversing the adverse effects of TTX on cell viability, calcium flux, and cell osmotic swelling. In mouse models challenged with TTX intoxication, the Neuron-NS enhanced the mouse survival rate in both treatment and prevention regimens. In addition, mice injected with Neuron-NS showed an absence of acute toxicity. Neuron-NS leverages the binding interactions with the neuron membrane shared by all neurotoxins regardless of their molecular structures. This strategy overcomes the limitations of current structure-based detoxification approaches. Besides TTX, Neuron-NS also neutralized botulinum toxin and saxitoxin, two additional neurotoxins with distinct working mechanisms,

demonstrating broad-spectrum detoxification capabilities of Neuron-NS. [40, 41] Although the Neuron-NS reported here is largely a proof-of-concept study, its success demonstrates the feasibility and allows for more efficient neurotoxin detoxification in the future. For example, the neuron membrane can be coated onto nanoscale oil droplets. The membrane and the oil core can work together to neutralize toxins. Alternatively, the membrane can be coated onto enzymatic nanoparticles for continuous detoxification, as the toxin degradation will no longer be limited by membrane–toxin binding stoichiometry. [42] The membrane can also be modified through metabolic or genetic methods to further enhance detoxification capacity. [43] Bulk materials such as hydrogels can imbed Neuron-NS and enhance their local retention for a prolonged detoxification ability. [44, 45] So far, antibodies are the main detoxification platform against TTX. However, the effectiveness of anti-TTX antibodies varies dramatically in different studies. In addition, Neuron-NS differ from the antibodies in their composition and working mechanism, making a direct comparison of their efficacy challenging. [46, 47] Nevertheless, the reported Neuron-NS formulation is expected to join current detoxification research and become a promising biomimetic nanoparticle system for the effective management of various types of neurotoxic poisoning.

Chapter 2, in full, is a reprint of the material as it appears in *ACS nano*, 2022, Dan Wang, Xiangzhao Ai, Yaou Duan, Nianfei Xian, Ronnie H. Fang, Weiwei Gao, and Liangfang Zhang. The dissertation author was the primary author of this paper.

2.5 Reference

[1] C.G. Goetz, E. Meisel, Biological neurotoxins, Neurologic clinics 18(3) (2000) 719-740.

[2] B.P. Lanphear, R.O. Wright, K.N. Dietrich, Environmental neurotoxins, Pediatrics in Review 26(6) (2005) 191-198.

[3] S. Cestèle, W.A. Catterall, Molecular mechanisms of neurotoxin action on voltage-gated sodium channels, Biochimie 82(9-10) (2000) 883-892.

[4] M. Stevens, S. Peigneur, J. Tytgat, Neurotoxins and their binding areas on voltage-gated sodium channels, Frontiers in pharmacology 2 (2011) 14152.

[5] A. Brunger, R. Jin, M. Breidenbach, Highly specific interactions between botulinum neurotoxins and synaptic vesicle proteins, Cellular and Molecular Life Sciences 65 (2008) 2296-2306.

[6] C. Colasante, O. Rossetto, L. Morbiato, M. Pirazzini, J. Molgó, C. Montecucco, Botulinum neurotoxin type A is internalized and translocated from small synaptic vesicles at the neuromuscular junction, Molecular Neurobiology 48 (2013) 120-127.

[7] V. Hassan-Puttaswamy, D.J. Adams, R.M. Kini, A distinct functional site in Ω-neurotoxins: novel antagonists of nicotinic acetylcholine receptors from snake venom, ACS Chemical Biology 10(12) (2015) 2805-2815.

[8] P. Yasawardene, U. Jayarajah, I. De Zoysa, S.L. Seneviratne, Mechanisms of star fruit (Averrhoa carambola) toxicity: a mini-review, Toxicon 187 (2020) 198-202.

[9] O. Cenciarelli, P.W. Riley, A. Baka, Biosecurity threat posed by botulinum toxin, Toxins 11(12) (2019) 681.

[10] M. Tiemensma, R.W. Byard, Fatal sea snake envenomation, The American Journal of Forensic Medicine and Pathology 42(4) (2021) 401-404.

[11] S. Cai, R. Kumar, B.R. Singh, Clostridial neurotoxins: Structure, function and implications to other bacterial toxins, Microorganisms 9(11) (2021) 2206.

[12] T. Minamitani, K. Kiyose, R. Otsubo, T. Ito, H. Akiba, R.A. Furuta, T. Inoue, K. Tsumoto, M. Satake, T. Yasui, Novel neutralizing human monoclonal antibodies against tetanus neurotoxin, Scientific Reports 11(1) (2021) 12134.

[13] M. Cohn, Degeneracy, mimicry and crossreactivity in immune recognition, Molecular immunology 42(5) (2005) 651-655.

[14] D.M. Snow, R.R. Cobb, J. Martinez, I. Finger-Baker, L. Collins, S. Terpening, E.S. Syar, N. Niemuth, D. Kobs, R. Barnewall, A monoclonal antibody combination against both serotypes A and B botulinum toxin prevents inhalational botulism in a guinea pig model, Toxins 13(1) (2021) 31.

[15] C.-M.J. Hu, R.H. Fang, J. Copp, B.T. Luk, L. Zhang, A biomimetic nanosponge that absorbs pore-forming toxins, Nature nanotechnology 8(5) (2013) 336-340.

[16] K.K. Hill, G. Xie, B.T. Foley, T.J. Smith, Genetic diversity within the botulinum neurotoxin-producing bacteria and their neurotoxins, Toxicon 107 (2015) 2-8.

[17] W. Pradidarcheep, W.T. Labruyère, N.F. Dabhoiwala, W.H. Lamers, Lack of specificity of commercially available antisera: better specifications needed, Journal of Histochemistry & Cytochemistry 56(12) (2008) 1099-1111.

[18] M. Pirazzini, O. Rossetto, Challenges in searching for therapeutics against Botulinum Neurotoxins, Expert opinion on drug discovery 12(5) (2017) 497-510.

[19] C. Quezada, M. Vera, L.F. Barraza, Y. García, E.D. Pereira, Molecularly imprinted nanoparticle-based assay (MINA): Potential application for the detection of the neurotoxin domoic acid, Analytica Chimica Acta 1181 (2021) 338887.

[20] R.H. Fang, A.V. Kroll, W. Gao, L. Zhang, Cell membrane coating nanotechnology, Advanced materials 30(23) (2018) 1706759.

[21] S. Wang, D. Wang, Y. Duan, Z. Zhou, W. Gao, L. Zhang, Cellular nanosponges for biological neutralization, Advanced Materials 34(13) (2022) 2107719.

[22] Y. Chen, M. Chen, Y. Zhang, J.H. Lee, T. Escajadillo, H. Gong, R.H. Fang, W. Gao, V. Nizet, L. Zhang, Broad‐spectrum neutralization of pore‐forming toxins with human erythrocyte membrane‐coated nanosponges, Advanced healthcare materials 7(13) (2018) 1701366.

[23] Y. Chen, Y. Zhang, M. Chen, J. Zhuang, R.H. Fang, W. Gao, L. Zhang, Biomimetic nanosponges suppress in vivo lethality induced by the whole secreted proteins of pathogenic bacteria, Small 15(6) (2019) 1804994.

[24] Y. Chen, Y. Zhang, J. Zhuang, J.H. Lee, L. Wang, R.H. Fang, W. Gao, L. Zhang, Cell-membrane-cloaked oil nanosponges enable dual-modal detoxification, Acs Nano 13(6) (2019) 7209-7215.

[25] Z. Pang, C.-M.J. Hu, R.H. Fang, B.T. Luk, W. Gao, F. Wang, E. Chuluun, P. Angsantikul, S. Thamphiwatana, W. Lu, Detoxification of organophosphate poisoning using nanoparticle bioscavengers, ACS nano 9(6) (2015) 6450-6458.

[26] J.A. Copp, R.H. Fang, B.T. Luk, C.-M.J. Hu, W. Gao, K. Zhang, L. Zhang, Clearance of pathological antibodies using biomimetic nanoparticles, Proceedings of the National Academy of Sciences 111(37) (2014) 13481-13486.

[27] Q. Zhang, D. Dehaini, Y. Zhang, J. Zhou, X. Chen, L. Zhang, R.H. Fang, W. Gao, L. Zhang, Neutrophil membrane-coated nanoparticles inhibit synovial inflammation and alleviate joint damage in inflammatory arthritis, Nature nanotechnology 13(12) (2018) 1182-1190.

[28] Y. Zhang, Y. Chen, C. Lo, J. Zhuang, P. Angsantikul, Q. Zhang, X. Wei, Z. Zhou, M. Obonyo, R.H. Fang, Inhibition of pathogen adhesion by bacterial outer membrane‐coated nanoparticles, Angewandte Chemie International Edition 58(33) (2019) 11404-11408.

[29] Q. Zhang, A. Honko, J. Zhou, H. Gong, S.N. Downs, J.H. Vasquez, R.H. Fang, W. Gao, A. Griffiths, L. Zhang, Cellular nanosponges inhibit SARS-CoV-2 infectivity, Nano letters 20(7) (2020) 5570-5574.

[30] R.H. Fang, C.-M.J. Hu, B.T. Luk, W. Gao, J.A. Copp, Y. Tai, D.E. O'Connor, L. Zhang, Cancer cell membrane-coated nanoparticles for anticancer vaccination and drug delivery, Nano letters 14(4) (2014) 2181-2188.

[31] H. Gong, Q. Zhang, A. Komarla, S. Wang, Y. Duan, Z. Zhou, F. Chen, R.H. Fang, S. Xu, W. Gao, Nanomaterial biointerfacing via mitochondrial membrane coating for targeted detoxification and molecular detection, Nano Letters 21(6) (2021) 2603-2609.

[32] C.-M.J. Hu, L. Zhang, S. Aryal, C. Cheung, R.H. Fang, L. Zhang, Erythrocyte membrane-camouflaged polymeric nanoparticles as a biomimetic delivery platform, Proceedings of the National Academy of Sciences 108(27) (2011) 10980-10985.

[33] S.E. Gratton, P.D. Pohlhaus, J. Lee, J. Guo, M.J. Cho, J.M. DeSimone, Nanofabricated particles for engineered drug therapies: A preliminary biodistribution study of PRINT™ nanoparticles, Journal of Controlled Release 121(1-2) (2007) 10-18.

[34] S. Saruhashi, K. Konoki, M. Yotsu-Yamashita, The voltage-gated sodium ion channel inhibitory activities of a new tetrodotoxin analogue, 4, 4a-anhydrotetrodotoxin, and three other analogues evaluated by colorimetric cell-based assay, Toxicon 119 (2016) 72-76.

[35] Y. Kudo, J. Finn, K. Fukushima, S. Sakugawa, Y. Cho, K. Konoki, M. Yotsu-Yamashita, Isolation of 6-deoxytetrodotoxin from the pufferfish, Takifugu pardalis, and a comparison of the effects of the C-6 and C-11 hydroxy groups of tetrodotoxin on its activity, Journal of Natural Products 77(4) (2014) 1000-1004.

[36] K. Sugimoto, I. Kissin, G. Strichartz, A high concentration of resiniferatoxin inhibits ion channel function in clonal neuroendocrine cells, Anesthesia & Analgesia 107(1) (2008) 318-324.

[37] I. Vetter, C.A. Mozar, T. Durek, J.S. Wingerd, P.F. Alewood, M.J. Christie, R.J. Lewis, Characterisation of Nav types endogenously expressed in human SH-SY5Y neuroblastoma cells, Biochemical pharmacology 83(11) (2012) 1562-1571.

[38] K. Kogure, M.L. Tamplin, U. Simidu, R.R. Colwell, A tissue culture assay for tetrodotoxin, saxitoxin and related toxins, Toxicon 26(2) (1988) 191-197.

[39] G.S. Offeddu, C.E. Tanase, S. Toumpaniari, M.L. Oyen, R.E. Cameron, Stiffening by osmotic swelling constraint in cartilage‐like cell culture scaffolds, Macromolecular Bioscience 18(11) (2018) 1800247.

Chapter 3 Surface-modified CNPs for biological neutralization

3.1 Glycan-modified CNPs for enhanced neutralization of botulinum toxin

3.1.1 introduction

Botulinum neurotoxin (BoNT) is a protein toxin produced by the bacterium Clostridium botulinum (C. botulinum) and other related clostridial species [1]. BoNT includes seven distinct serotypes, designated as A-G, and belongs to the clostridial neurotoxin family along with tetanus neurotoxin [2]. All BoNT serotypes interfere with neural transmission by inhibiting the release of acetylcholine, a critical neurotransmitter at the neuromuscular junction, resulting in paralysis of the skeletal and autonomic nervous systems [3]. While BoNT has found numerous medical applications, it possesses characteristics that also make it a potential biowarfare weapon and bioterrorist agent [4]. Notably, BoNT is highly potent and lethal, often considered the deadliest substance known [5]. Additionally, it remains stable in complex forms and aerosolized formulations, facilitating its deliberate release in populated areas [6,7]. Moreover, the bacterium C. botulinum, an anaerobic spore-former, is relatively easy to culture, making unauthorized production of BoNT relatively straightforward [8]. The medical use of BoNT also raises concerns about its unlawful possession, transport, and misuse [9]. Furthermore, there is currently no effective treatment for BoNT intoxication. Recent efforts have focused on developing small molecule inhibitors [10,11], neutralizing antibodies [12], and vaccines [13,14]. However, progress has been slow due to the substantial diversity of BoNT structures. Given these characteristics, the threat posed by BoNT is significant, necessitating the development of an effective and broad-spectrum countermeasure against BoNT.

Over the past decade, CNPs composed of synthetic cores wrapped with natural cell membranes have emerged as a biomimetic detoxification platform [15-17]. One example is the

use of CNPs made with red blood cell (RBC) membrane, which mimic the properties of source RBCs and exhibit susceptibility to pore-forming toxins (PFTs) [18]. This susceptibility enables CNPs to intercept PFTs regardless of the molecular structures of the toxins [19,20]. Importantly, CNPs rely on the functionalities of host cells rather than the toxin structure for detoxification. This unique feature allows them to overcome the diversity of toxins and achieve broad-spectrum efficacy. Furthermore, by selecting specific types of cell membranes for coating, CNPs have demonstrated successful detoxification against various classes of harmful agents, including small molecule neurotoxicants [21,22], autoimmune antibodies [23,24], inflammatory cytokines [25], bacteria [26], and viruses [27]. Building upon these studies, researchers have also explored modifications to natural cell membrane composition or structure for enhanced detoxification [28,29]. For example, intrigued by the binding interactions between SARS-CoV-2 spike glycoprotein (S protein) and cell glycosaminoglycans like heparin, researchers have modified the cell surface glycans and increased the membrane heparin density on CNPs [30]. As a result, CNPs with a higher heparin density showed a greater binding capacity with viral S proteins and significantly increased inhibitory efficacy against SARS-CoV-2 infectivity.

Due to their unique biomimetic design, CNPs are capable of neutralizing BoNT, as the toxin relies on binding to host cells for its harmful effects. Although the exact mechanism of BoNT cellular entry is not fully understood, studies have revealed that ubiquitous polysialylated gangliosides, including GM1 and GT1b on the cell surface, are critical receptors responsible for the initial BoNT binding [31,32]. Given the crucial role of gangliosides, we hypothesized that increasing the expression level of gangliosides on the CNPs could enhance BoNT binding and neutralization capacity. To investigate this hypothesis, we chose THP-1 cells (MΦs), a human leukemia monocytic cell line with macrophage-like functions, as the source cells, in combination

with glycan modification, to fabricate CNPs for BoNT detoxification. MΦ CNPs have been extensively studied for various detoxification applications [27,30,33]. Like neurons, MΦs also possess complex glycolipids that are essential for initial BoNT binding and are targets of BoNT [34]. In this study, we first used unmodified MΦs (denoted 'un-MΦs') and increased the expression levels of gangliosides using a metabolic glycan-engineering approach [35]. Subsequently, we collected the membrane from these modified MΦs (denoted 'gan-MΦs') and utilized it to prepare CNPs (denoted 'gan-MΦ-NS') by coating the membrane onto polymeric cores made from poly(lactic-co-glycolic acid) (PLGA). Our findings demonstrate that gan-MΦ-NS exhibit an enhanced capacity for BoNT binding and higher detoxification efficacy compared to CNPs prepared from unmodified MΦs (denoted 'un-MΦ-NS').

3.1.1 Preparation and characterization of gan-MΦ-NS

In the study, we increased ganglioside expression on THP-1 cells (MΦ) by culturing these cells in media with high concentrations of N-acetyl-d-mannosamine-tetraacylated (Ac4ManNAc). Ac4ManNAc is a monosaccharide precursor known for its ability to increase cell surface ganglioside levels through sialic acid metabolism and glycosylation [42,43]. Following the glycanmodification of the THP-1 cells, we derived their membrane using disruption together with differential centrifugation [44]. Meanwhile, we prepared PLGA cores using an established nanoprecipitation method. Lastly, we coated the cell membrane onto PLGA cores using sonication, forming gan-MΦ-NS formulation with overexpressed gangliosides on the surface. DLS measurements showed that gan-MΦ-NS and un-MΦ-NS had comparable hydrodynamic diameters (Figure 3.1A). These values were larger than the bare PLGA cores, indicating the coating of a bilayered cell membrane onto the polymeric cores. In addition, the CNPs showed less negative surface zeta potential (ξ) values than the PLGA cores, likely due to the charge

screening by the coated cell membrane. Notably, the zeta potential value of gan-MΦ-NS was slightly more negative than that of un-MΦ-NS, attributable to the higher sialic acid levels on gan-MΦ-NS [45]. The gan-MΦ-NS was further visualized by TEM. We observed a typical spherical core-shell structure consistent with the unilamellar membrane coating surrounding a solid core (Figure 3.1B). Moreover, the hydrodynamic sizes of CNPs showed minor changes over 72 h in water, 1X phosphate-buffered saline (PBS), and 50% serum, suggesting their excellent colloidal stability (Figure 3.1C). These results demonstrate the successful fabrication of gan-MΦ-NS.

We next verified ganglioside expression on gan-MΦ-NS. We selected GM1 and GT1b, two key ganglioside receptors responsible for BoNT binding, and measured their expression levels. It was shown that gan-MΦ-NS had 2.4 folds higher GM1 expression and 2.2 folds higher GT1b expression than un-MΦ-NS (Figure 3.1D). Notably, gan-MΦ-NS and un-MΦ-NS showed negligible cytotoxicity. We further compared the pharmacokinetic profiles of these two CNP formulations. Specifically, we loaded a hydrophobic fluorophore (DiD) into the PLGA cores and prepared the DiD-labeled gan-MΦ-NS or DiD-labeled un-MΦ-NS. At all times, serum concentrations of gan-MΦ-NS were higher than those of un-MΦ-NS. At 48 h after intravenous injection, gan-MΦ-NS showed 8.3% overall retention in the blood compared to the 2% of the un-MΦ-NS (Figure 3.1E). Based on a two-compartment model that has been applied to fit the circulation results of CNPs in previous studies, the elimination half-life was calculated as 20.1 h for gan-MΦ-NS and 12.6 h for un-MΦ-NS in the blood [36]. The prolonged circulation of gan-MΦ-NS is attributable to the increased ganglioside levels on the membrane, which suppress CNP clearance by the mononuclear phagocyte system (MPS)[46, 47].

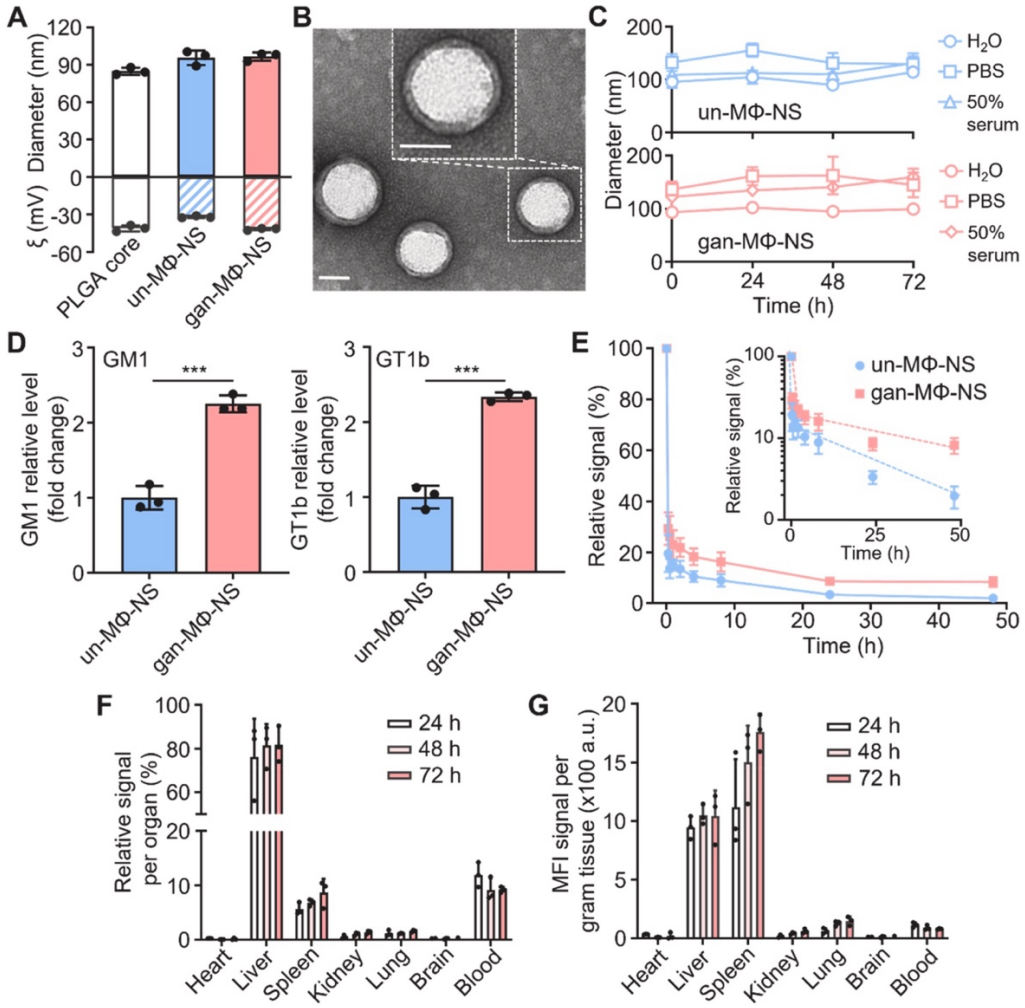

Figure 3.1 Preparation and characterization of gan-MΦ-NS.

(A) Hydrodynamic diameter (top, nm) and zeta potential (bottom, mV) of gan-MΦ-NS. The PLGA cores and un-MΦ-NS were used as controls. (B) A representative image of gan-MΦ-NS examined with transmission electron microscopy. Scale bar = 50 nm. (C) The hydrodynamic diameter of gan-MΦ-NS and un-MΦ-NS in H2O, 1X PBS, and 50% serum over 72 h. (D) GM1 and GT1b expression levels on gan-MΦ-NS in comparison with un-MΦ-NS. (E) DiD-loaded un-MΦ-NS and gan-MΦ-NS were injected intravenously through the tail vein of mice. At various time points, blood was withdrawn intraorbitally and measured for fluorescence at 670 nm to evaluate the systemic circulation lifetime of the CNPs. (F, G) The biodistribution profile of gan-MΦ-NS at 24, 48, and 72 h after the intravenous injection of DiD-labeled gan-MΦ-NS in mice. (F) Relative signals per organ. (G) Mean fluorescent intensities (MFI) per gram of tissue (n = 3 per group). In (A, C, D), data are presented as mean ± s.d. and n = 3 independent experiments using the same batch of gan-MΦ-NS or un-MΦ-NS. The data in (E) are presented as mean ± s.d. and n = 6 independent experiments using the same batch of gan-MΦ-NS or un-MΦ-NS. The data in (F) and (G) are presented as mean + s.d. and n = 3 independent experiments using the same batch of gan-MΦ-NS. ***$p < 0.001$; statistical analysis was performed using a two-tailed paired t-test.

We also tested gan-MΦ-NS biodistribution in mice at 24, 48, and 72 h after the intravenous injection. The analysis of the proportion of signals per organ shows a decrease in signals in the blood over time and a corresponding increase in signals in the liver and spleen (Figure 3.1F). Meanwhile, the analysis of signals per organ weight shows that gan-MΦ-NS accumulated mostly in the liver and spleen, the two primary organs in the reticuloendothelial system (RES, Figure 3.1G). Additionally, the blood showed significant levels of gan-MΦ-NS. These results suggest that gan-MΦ-NS, despite their enhanced ganglioside pression, are most likely cleared through RES.

3.1.2 BoNT binding capacity and specificity of gan-MΦ-NS

Following the characterization of gan-MΦ-NS, we then examined their binding capacity against BoNT. We first kept the CNP concentration constant and varied the toxin concentration. As shown in Figure 3.2A, gan-MΦ-NS showed a higher binding capacity with BoNT than un-MΦ-NS. Based on this experiment, the dissociation constant of BoNT with gan-MΦ-NS and un-MΦ-NS were measured to be 1.03×10^{-12} M and 4.14×10^{-12} M, respectively. Additionally, serial dilutions of un-MΦ-NS or gan-MΦ-NS were mixed with BoNT at a fixed concentration. After the incubation, CNPs were removed by ultracentrifugation, and the unbound BoNT concentration in the supernatant was quantified by ELISA. As shown in Figure 3.2B, as the CNP concentration increased, the concentration of the remaining BoNT decreased, suggesting a dose-dependent binding interaction between CNPs and BoNT. At all concentrations tested, gan-MΦ-NS exhibited lower levels of remaining BoNT in the supernatants than un-MΦ-NS counterparts, indicating a higher BoNT binding capacity of gan-MΦ-NS than un-MΦ-NS. We further treated

the CNPs with NA to test whether the enhanced BoNT binding capacity was due to the overexpressed gangliosides. This enzyme degrades gangliosides by cleaving the terminal sialic acid residues. After NA treatment, we washed the CNPs and repeated the binding study. As shown in Figure 3.2C, after the NA treatment, the remaining BoNT concentrations in both groups were near the baseline, suggesting the loss of BoNT binding capacity. This result confirmed that the enhanced BoNT binding of gan-MΦ-NS was due to a higher level of gangliosides on the CNP surfaces. We also measured bound BoNT release from the CNPs for 60 h and found negligible BoNT release during the period.

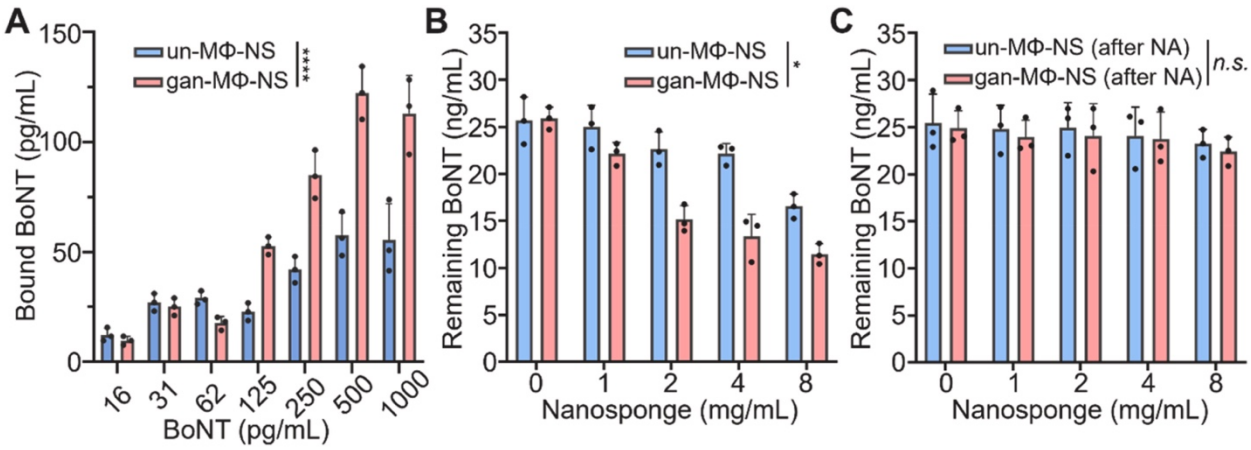

Figure 3.2 BoNT binding capacity and specificity of gan-MΦ-NS.

(A) Quantification of BoNT binding to un-MΦ-NS or gan-MΦ-NS with fixed CNP concentrations. In this experiment, a fixed concentration of 100 μg/mL of un-MΦ-NS or gan-MΦ-NS was mixed with BoNT at various concentrations, ranging from 0 to 1000 pg/mL. After a 30-min incubation period, concentrations of unbound BoNT were determined using ELISA. (B) BoNT was mixed with different concentrations of un-MΦ-NS or gan-MΦ-NS and incubated for 30 min. Then the mixture was ultracentrifuged, and the remaining BoNT concentrations in the supernatant were measured by ELISA. (C) The un-MΦ-NS and gan-MΦ-NS were pre-treated with neuraminidase A (NA, 100 units) overnight, followed by the binding capacity measurements as described in (C). Data presented as mean + standard deviation (n = 3 independent experiments using the same batch of the CNPs); n.s.: not significant; *$p < 0.01$; ****$p < 0.0001$; statistical analysis was performed using a two-tailed paired t-test

3.1.3 In vitro neutralization of BoNT by gan-MΦ-NS

We next tested BoNT neuralization by gan-MΦ-NS in vitro using a synaptic vesicle recycling assay. In this assay, Neuro-2a cells, a murine neuroblastoma cell line, were first fluorescently stained for their synaptic vesicles with a styryl FM dye. After washing, the cells were treated with high K^+ and Ca^{2+}, which depolarized the cells and quickly released the vesicles through exocytosis. The depolarization led to the loss of the dye to the extracellular space and a concomitant loss of fluorescence (Figure 3.3A) [48, 49]. When BoNT was added to the cells, it blocked synaptic vesicle release. Therefore, the depolarization treatment caused negligible fluorescence change. However, when BoNT was first mixed with gan-MΦ-NS and then added to the cells, the fluorescence loss appeared after the depolarization treatment, implying that gan-MΦ-NS neutralized the biofunction of BoNT. However, if gan-MΦ-NS was first treated with NA and then mixed with BoNT, the fluorescence loss was not detected, suggesting that the observed BoNT neutralization was mediated by the gangliosides on the gan-MΦ-NS surface.

We used the same assay to compare gan-MΦ-NS and un-MΦ-NS for their dose-dependent neutralization against BoNT. The study was carried out in two regimens. In a pre-incubation regimen, we first mixed BoNT with CNPs and then added the supernatants to the cells for testing. When the CNP concentration increased, the percentage of synaptic inhibition decreased accordingly, indicating a dose-dependent BoNT neutralization by both CNP formulations (Figure 3.3B). However, synaptic inhibition by gan-MΦ-NS was consistently lower than un-MΦ-NS, indicating a higher BoNT neutralization capacity of gan-MΦ-NS than un-MΦ-NS.

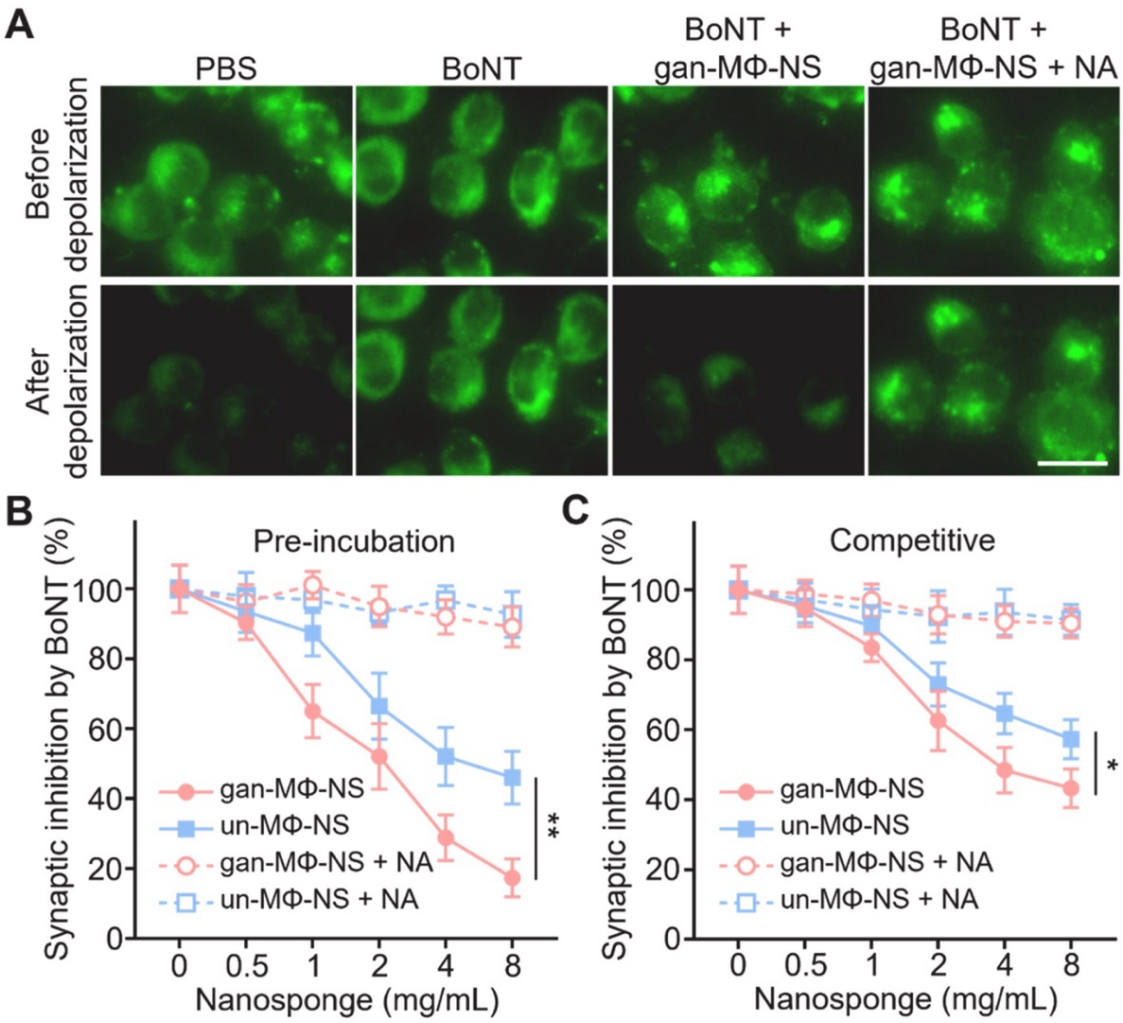

Figure 3.3 *In vitro* neutralization of BoNT by Gan-MΦ-NS.

(A) Representative fluorescence images of Neuro-2a cells before and after depolarization treatment for synaptic vesicle release. Gan-MΦ-NS (8 mg/mL) or NA-treated gan-MΦ-NS (8 mg/mL) were incubated with the BoNT (12.5 ng/mL) for 30 min. After removing CNPs, the supernatants were incubated with the cells to test BoNT neutralization using a synaptic vesicle recycling assay. The green color represents synaptic vesicles stained with FM1-43 (a styryl fluorescent dye). Scale bar, 25 μm. (B) Synaptic inhibition with various concentrations of gan-MΦ-NS in a pre-incubation regimen, where the CNP and BoNT were mixed first. After removing the CNPs, the supernatants were added to the cells. (C) Synaptic inhibition with various concentrations of gan-MΦ-NS in a competitive regimen, where the CNP was added to the cells, followed by adding BoNT. In both regimens, un-MΦ-NS, NA-treated gan-MΦ-NS, and NA-treated un-MΦ-NS were used as controls. For the signal normalization, fluorescence from cells added with BoNT (12.5 ng/mL), but no CNP treatment, was defined as 0% of synaptic inhibition. Fluorescence from cells without BoNT or CNPs was defined as 100% of synaptic inhibition. Data presented as mean ± s.d. (n = 3); n.s.: not significant; *$p < 0.05$; **$p < 0.01$; statistical analysis was performed by using a two-tailed paired t-test.

When the two CNP formulations were treated with NA, both lost their BoNT neutralization capability, confirming the specific role played by the gangliosides in neutralizing BoNT. In a competitive regimen, we added CNPs to the cells, followed by adding BoNT to the mixture solution. In this regimen, CNPs must compete with the cells to bind the toxin for neutralization. As a result, their neutralization capacity became lower than the pre-incubation regimen (Figure 3.3C). However, like in the pre-incubation regimen, gan-MΦ-NS showed a higher neutralization capacity than un-MΦ-NS at all tested concentrations, and BoNT neutralization was mediated by the gangliosides on the CNP surface.

3.1.4 In vivo neutralization of BoNT by gan-MΦ-NS

Before testing the in vivo neutralization of BoNT using a mouse BoNT intoxication model, we first determined the lethal dosage of BoNT in a single intravenous injection. As shown in Figure 3.4A, BoNT induced a dose-dependent lethality. Under our experimental conditions, we found that 0.75 ng/kg was the lowest dosage to cause 100% of death (LD100), and 0.65 ng/kg was the median lethal dosage to cause 50% of mouse death (LD50). Next, we examined CNP efficacy using a treatment regimen where an LD100 (0.75 ng/kg) of BoNT was administered intravenously first, followed by an intravenous injection of the CNP 1 min later. As shown in Fig. 3.4B, all mice injected with gan-MΦ-NS (100 mg/kg) survived. In contrast, only 40% of mice injected with the same dose of un-MΦ-NS survived within 7 days, and all mice treated with PBS died. Notably, this study chose a 1-min time interval between BoNT and CNPs injections. The detoxification efficacy of CNP is likely to decrease as this interval increases owing to the extremely potent BoNT neurovirulence. Besides the treatment regimen, we also evaluated the CNP efficacy in a preventive regimen, where the CNP was first administered intravenously, followed by injecting LD50 (0.65 ng/kg) of BoNT 1 min later. As shown in

Figure 3.4C, all mice treated with gan-MΦ-NS (100 mg/kg) survived. In contrast, 83.3% of mice treated with un-MΦ-NS survived, and only 50% of mice treated with PBS survived. Similar to the treatment regimen, the detoxification efficacy of CNPs is likely to decrease as this interval increases in the preventative regimen due to the continuous clearance of the CNP in vivo. Nevertheless, these results demonstrated a significantly enhanced protection of gan-MΦ-NS against BoNT intoxication in vivo.

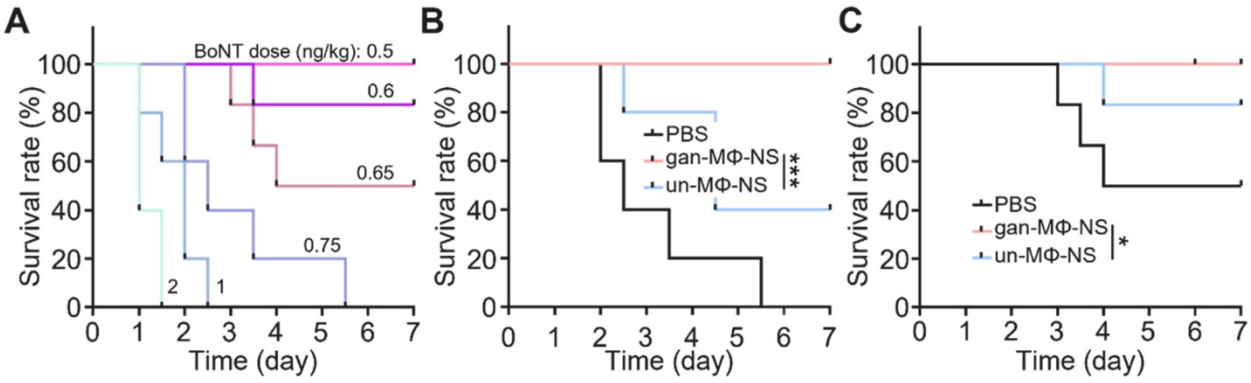

Figure 3.4 *In vivo* neutralization of BoNT by Gan-MΦ-NS.

(A) Survival rates of mice within 7 days after intravenous injection of BoNT (0.5-1 ng/kg, n = 6). (B) Survival rates of mice treated with gan-MΦ-NS in a treatment regimen where BoNT (0.75 ng/kg) was first injected intravenously into mice, followed by the intravenous injection of gan-MΦ-NS (0.2 mL, 100 mg/kg) 1 min later. Mice treated with PBS (0.2 mL) or un-MΦ-NS (0.2 mL, 100 mg/kg) were used as controls. (C) Survival rates of mice treated with gan-MΦ-NS in a prophylactic regimen, where gan-MΦ-NS (0.2 mL, 100 mg/kg) was first injected intravenously into mice, followed by BoNT injection (0.65 ng/kg) 1 min later. Mice treated with PBS (0.2 mL) or un-MΦ-NS (0.2 mL, 100 mg/kg) were used as controls. In all groups, n = 6, *$p < 0.05$, ***$p < 0.001$. Statistical analysis was performed by using a Log-rank test.

3.1.5 In vivo safety of gan-MΦ-NS

Lastly, we investigated the acute toxicity of gan-MΦ-NS in vivo. In this experiment, our primary objective was to test possible adverse effects at the therapeutic dosages used in the in vivo efficacy studies. Therefore, we used the highest therapeutic dosage, 100 mg/kg, for the toxicity evaluation. In the study, the healthy mice were injected with gan-MΦ-NS intravenously

(100 mg/kg, n = 3). A blood count and a comprehensive metabolic panel were performed 1 day after the CNP injection. It was shown that the hemocytes, including red blood cells (RBC), white blood cells (WBC), and platelets (PLT), of mice injected with gan-MΦ-NS, were comparable to those of the control mice injected with PBS (Figure 3.5A). Meanwhile, all blood markers were consistent with baseline levels, confirming the excellent biosafety profile of gan-MΦ-NS in mice (Figure 3.5B).

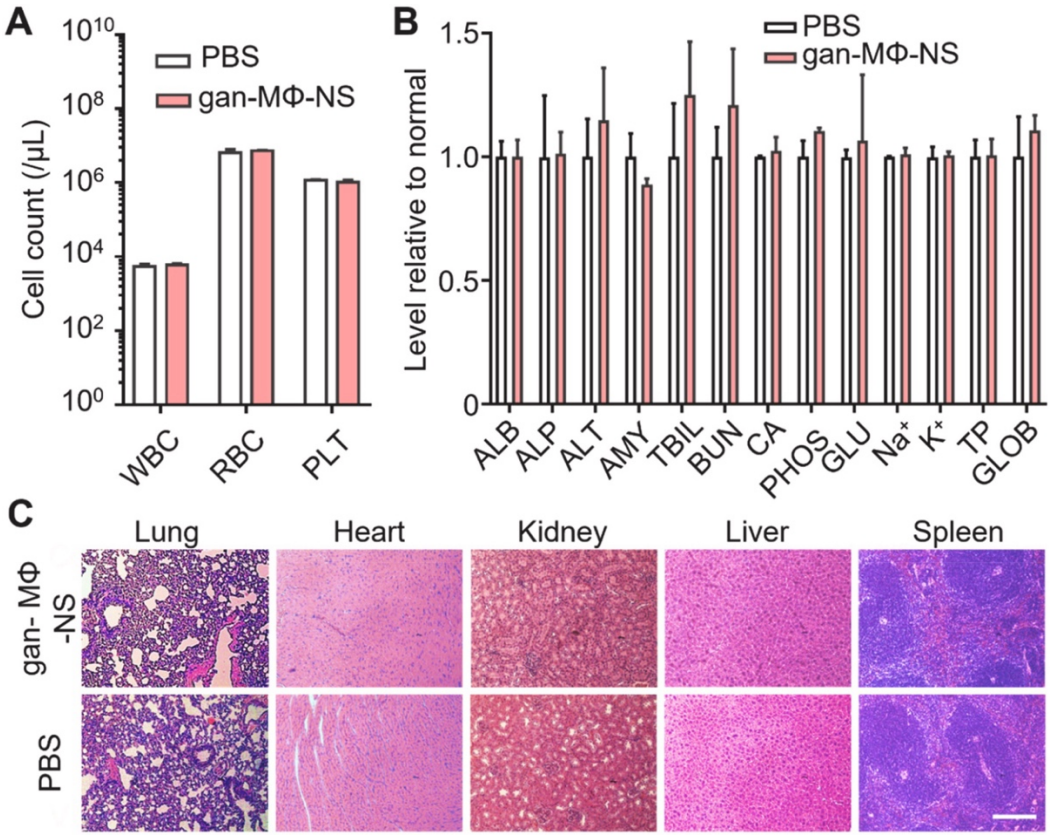

Figure 3.5 *In vivo* biosafety of gan-MΦ-NS.

(A) Counts of various blood cells 1 day after intravenous injection of PBS or gan-MΦ-NS (n = 3; data represents the geometric mean + SD). WBC, white blood cells; RBC, red blood cells; PLT, platelets. (B) A blood biochemistry panel analysis after 1 day of PBS or gan-MΦ-NS injection (n = 3; mean + SD). ALB, albumin; ALP, alkaline phosphatase; ALT, alanine transaminase; AMY, amylase; TBIL, total bilirubin; BUN, blood urea nitrogen; CA, calcium; PHOS, phosphorus; GLU, glucose; NA+, sodium; K+, potassium; TP, total protein; GLOP, globulin. (C) H&E staining of histology sections from major organs, including the heart, liver, spleen, lung, and kidney, 1 week after PBS or gan-MΦ-NS administration. Scale bar = 250 μm.

Seven days after the CNP injection, the mice were sacrificed, and the major organs were collected, sectioned, and stained with hematoxylin and eosin (H&E) for histological analysis. As shown in Figure 3.5C, the organ tissues in the mice, including the liver, spleen, heart, lungs, and kidneys, appeared normal compared to the mice injected with PBS. Overall, these results demonstrate the absence of short-term toxicity of gan-MΦ-NS.

3.1.6 Methods

Cell culture

THP-1 cells, a human monocytic leukemia cell line, were obtained from American Type Culture Collection (ATCC, TIB-202). The cells were seeded in T175 suspension flasks (Olympus Plastics) at 2×10^5 cells/mL and cultured in RPMI 1640 medium supplemented with 10% fetal bovine serum (FBS) and 1% penicillin-streptomycin (Thermo Fisher Scientific) at 37 °C with 5% CO_2 in a humidity-controlled incubator. For glycol modification, 100 μM N-acetylmannosamine-tetraacylated (Ac4ManNAc, Chem-Impex) were added to the cell culture. After 72 h, cells were harvested by centrifugation at 800×g and washed twice with 1X PBS (pH = 7.4). The cells were resuspended in a 1:1 mixture of serum-free RPMI and HyCryo 2X cryopreservation medium (GE Healthcare) and stored at -80 °C for subsequent studies.

Preparation and characterization of CNPs

Cell membranes from un-MΦs and gan-MΦs were harvested with a previously published protocol [36]. Briefly, thawed cells were washed with 1X PBS and resuspended in a hypotonic lysing buffer containing 30 mM Tris-HCl (pH = 7.5), 225 mM D-mannitol, 75 mM sucrose, 0.2 mM ethylene glycol-bis(β-aminoethyl ether)-N,N,N’,N’-tetraacetic acid (EGTA), and a protease and phosphatase inhibitor cocktail (all reagents from Millipore-Sigma). Cells were then disrupted with a probe homogenizer (Kinematica Polytron PT 10/35 GT). The homogenate was

centrifuged at 20 k × g for 25 min at 4 °C. The pellet was discarded, and the supernatant was centrifuged again at 100 k × g for 35 min at 4 °C. The cell membrane was collected as the pellet and washed with 0.2 mM ethylenediaminetetraacetic acid (EDTA) in water by ultracentrifugation. Membrane protein was quantified with a bicinchoninic acid (BCA) protein assay (ThermoFisher Scientific) in reference to bovine serum albumin (BSA). Approximately 1 × 10^8 cells yield 2 mg membrane (protein weight). The membrane was suspended in 0.2 mM EDTA and stored at -80 °C for subsequent studies.

The cell membranes were coated onto polymeric cores with a sonication method. Briefly, the polymeric cores were synthesized by adding 1 mL poly(lactic-co-glycolic acid) (50:50 PLGA, 0.67 dl/g; Lactel Absorbable Polymers) in acetone (10 mg/mL) to 2 mL water. After evaporation of acetone, membranes from un-MΦs or gan-MΦs were mixed with the cores at a polymer-to-membrane protein weight ratio of 1:1. The mixture was then sonicated in a bath sonicator (Thermo Fisher Scientific) for 2 min. The size and zeta potential were measured with dynamic light scattering (DLS, Malvern ZEN 3600 Zetasizer). CNP microscopic morphology was visualized with transmission electron microscopy (TEM, FEI 200 KV Sphera) with uranyl acetate staining. Colloidal stability was studied by suspending CNPs in 1X PBS or 50% serum at a protein concentration of 0.5 mg/mL. The samples were stored at 4 °C. The hydrodynamic diameter was measured with DLS daily for 3 d.

Quantification of ganglioside levels on gan-MΦ and gan-MΦ-NS

For GM1 quantification, gangliosides were first extracted from the MΦs or CNPs by following an established protocol [37,38]. The extraction was performed with 1 × 10^8 cells or 2 mg CNPs (membrane protein weight). The cells or CNPs suspensions were suspended in 560 μL ultrapure water and mixed with 800 μL methanol. Then 400 μL chloroform was added to the

mixture. The sample was stirred for 2 h at room temperature and then centrifuged at 500×g for 5 min. The upper phase containing gangliosides was collected. After evaporation of the residue solvents, the gangliosides in the water were extracted by a Sep-Pak tC18 solid-phase extraction cartridge (Waters). Briefly, the cartridge was first washed with 3 mL methanol, followed by 3 mL chloroform-methanol-water mixture (2:43:55, v%). Then the sample was loaded onto the cartridge. The flow-through was collected and reloaded onto the column for optimized adsorption. After the adsorption, the cartridge was washed with 3 mL of a chloroform-methanol-water mixture (2:43:55, v%) and 3 mL of methanol-water (50:50, v%). Gangliosides were eluted with 3 mL methanol. After evaporation of the solvent, ganglioside powder was dissolved in 50 μL methanol for high-performance liquid chromatography (HPLC, Agilent) analysis with a C18 analytical column (Brownlee, 2 μL injection volume). The mobile phase consisted of an acetonitrile-water gradient (20%-100% acetonitrile for 20 min at 0.3 mL/min). The gangliosides were monitored at 215 nm. A standard curve was obtained with known concentrations of GM1 (2–0.125 mM, Fisher Scientific) and used to calculate GM1 concentrations in the sample.

For GT1b quantification, 10 mg/mL NHS-Fluorescein (Thermo Scientific) DMSO stock solution was prepared. An NHS-Fluorescein working solution was prepared by adding 5 μL stock solution into 45 μL sodium bicarbonate buffer (pH = 8.2, Millipore-Sigma). Then, 5 μL working solution was mixed with 50 μL anti-GT1b ganglioside antibody (1 mg/mL, Millipore-Sigma) and 45 μL sodium bicarbonate buffer. The mixture was incubated at room temperature for 1 h and washed with 1X PBS by using Amicon Ultra-4 Centrifugal Filters (Millipore, 10 kDa molecular weight cutoff). After the centrifugation, the dye-labeled antibody was resuspended in 50 μL 1X PBS. To examine GT1b level, 400 μL CNP suspensions (1 mg/mL, un-MΦ-NS or gan-MΦ-NS, membrane protein concentration) were blocked by adding BSA (final concentration 1

w/v%) in 400 μL 1X PBS for 30 min, followed by mixing with 4 μL dye labeled-antibody (1 mg/mL) and incubating for 30 min. CNPs were pelleted by centrifugation at 20 k × g for 5 min and then resuspended in 1X PBS (400 μL) to measure the fluorescence intensity with an Infinite M200 plate reader (Tecan, excitation/emission = 494/518 nm).

In vivo pharmacokinetics and biodistribution studies

All animal studies were approved under the Institutional Animal Care and Use Committee (IACUC) guidelines at the University of California San Diego (UCSD). The 6-week-old ICR male and female mice were purchased from Harlan Laboratories and housed in an animal facility at UCSD under federal, state, local, and National Institutes of Health guidelines for animal care. To label the CNPs, DiD dye (excitation/emission = 645/665 nm, Thermo Fisher Scientific) was mixed with PLGA in acetone (0.1 wt%), followed by CNP preparation with the above procedure. For the pharmacokinetic study, DiD-labeled gan-MΦ-NS (100 μL, 20 mg/kg, n = 3) was injected intravenously via the tail vein. At 0.02, 0.25, 0.5, 1, 2, 4, 8, 24, and 48 h postinjection, one drop of blood (~30 μL) was collected from each mouse via submandibular puncture with heparin-coated tubes. Then 20 μL blood was mixed with 180 μL 1X PBS in a 96-well plate for fluorescence measurement with an Infinite M200 plate reader (Tecan). The DiD-labeled un-MΦ-NS was also prepared as a control group. For the biodistribution study, DiD-labeled gan-MΦ-NS (200 μL, 100 mg/kg, n = 3) was injected through the tail vein. At 24, 48, and 72 h postinjection, organs, including the liver, kidneys, spleen, brain, lungs, heart, and blood, were collected, and homogenized using a mini bead-beater (Biospec) in 1X PBS. All fluorescence measurements were performed with an Infinite M200 plate reader (Tecan).

BoNT binding capacity and specificity of gan-MΦ-NS

BoNT and CNP binding was first investigated by maintaining constant CNP concentration while varying the toxin concentration. Specifically, 100 μg/mL un-MΦ-NS or gan-MΦ-NS was mixed with BoNT ranging from 0 to 1000 pg/mL (final concentration) in 1X PBS containing 1w/v% BSA. The mixtures were incubated for 30 min at 37 °C and then centrifuged at 20 k × g for 10 min to pellet the CNPs. The remaining BoNT in the supernatants was quantified with ELISA assay to calculate the amount of BoNT that bound to the CNPs. BoNT and CNP binding was also examined by keeping toxin concentration constant while varying the CNP concentration. Specifically, 25 ng/mL (0.5 U/mL, U is the toxin amount that causes 50% of mice death within 4 days) BoNT type A1 from Clostridium botulinum (List labs) was mixed with 100 μL various concentrations of un-MΦ-NS or gan-MΦ-NS (0-8 mg/mL) in 1XPBS containing 1w/v% BSA. The mixtures were incubated at room temperature for 30 min under vortexing and then centrifuged at 20 k × g for 10 min to pellet the CNPs. The remaining BoNT in the supernatants was quantified with an enzyme-linked immunosorbent assay (ELISA, R&D Systems). To verify the binding specificity, 100 units of α2-3,6,8,9 Neuraminidase A (NA, New England Biolabs) in a storage buffer (50 mM NaCl, 20 mM Tris-HCl, 1 mM EDTA, pH 7.5) were first mixed with 2 mg un-MΦ-NS or gan-MΦ-NS in 50 μL reaction buffer (5 mM $CaCl_2$ and 50 mM sodium acetate at pH 5.5) overnight to degrade the gangliosides. NA-treated CNP binding with BoNT was quantified by using the same procedure.

In vitro neutralization of BoNT by gan-MΦ-NS

BoNT cellular activities were examined by using a synaptic vesicle recycling assay [39,40]. In this assay, Neuro-2a cells (a murine neuroblastoma cell line, ATCC) were washed twice with Hank's balanced salt solution (HBSS) and incubated with 10 μM N-(3-Triethylammoniumpropyl)-4-(4-(Dibutylamino) Styryl) Pyridinium Dibromide (FM1-43,

excitation/emission = 480/520 nm, Thermo Fisher Scientific) in HBSS containing 2 mM $CaCl_2$ and 56 mM KCl for 10 min. The cells were then washed twice in Ca^{2+}/K+-free HBSS containing 0.5 mM EGTA to remove the free dye. The cells were kept in 100 μL Ca^{2+}/K^+-free HBSS and depolarized by adding 2 μL Ca^{2+}/K^+ solution (2 mM Ca^{2+} and 56 mM K^+). Cells were imaged with an inverted fluorescence microscope (EVOS, Thermo Fisher Scientific) for 15 min with 1 min intervals. The images were analyzed with ImageJ to quantify the fluorescence. The intensity from cells without the treatment and with FM1-43 but without depolarization was normalized as 0 and 100% intensity.

To evaluate BoNT neutralization, 0-25 ng/mL of BoNT were incubated with Neuro-2a cells (15,000 cells/well in a 96-well plate) for 3 h. The cells were washed with HBSS twice, followed by depolarization and fluorescence imaging. The lowest BoNT concentration that reached maximum inhibition was determined (12.5 ng/mL), and this inhibition was defined as 100%. To evaluate BoNT neutralization, two regimens were tested. In a pre-incubation regimen, BoNT (12.5 ng/mL final concentration) was incubated with un-MΦ-NS or gan-MΦ-NS at various concentrations (0-8 mg/mL) for 30 min. Then the CNP was removed with centrifugation at 20 k × g for 10 min. The supernatant was tested for BoNT activity. In a competitive regimen, the Neuro-2a cells were first added with un-MΦ-NS or gan-MΦ-NS (0–8 mg/mL in 100 μL medium), followed by adding BoNT (12.5 ng/mL final concentration). Cells were incubated for 30 min. Then the media were replaced, and the cells were used in the above assay to examine the BoNT activity. For the specificity studies, the CNPs were treated with α2-3,6,8,9 Neuraminidase A (NA, 100 units) 12 h to cleave gangliosides, followed by an inhibition test.

In vivo neutralization of BoNT by gan-MΦ-NS

To determine the lethal dosage of BoNT in vivo, the BoNT stock was first diluted in gelatin-phosphate buffer (30 mM, pH 6.2, 0.2 w/v% gelatin) [41]. Then, BoNT solutions were injected intravenously through the tail vein into ICR mice (~20 g) at various dosages (0-2 ng/kg, n = 6). Mouse survival was monitored twice daily over 7 d. The values of LD100 (the lowest dosage to cause 100% of death) and LD50 (the dosage to cause 50% of death) were derived from the variable slope model using GraphPad Prism 7. Two dosing regimens were used to examine the CNP therapeutic efficacy. In a treatment regimen, BoNT at the LD100 dose (0.75 ng/kg) was injected intravenously into mice. After 1 min, un-MΦ-NS or gan-MΦ-NS (0.2 mL, 100 mg/kg, n = 6) were injected intravenously. In a prevention regimen, mice were first injected with un-MΦ-NS or gan-MΦ-NS (0.2 mL, 100 mg/kg, n = 6) through the tail vein. Two minutes after the injection, mice were injected with BoNT at LD50 dose (0.65 ng/kg) through the tail vein. Mice were monitored twice daily for euthanasia criteria, which included morbidity exceeding 24 h, weight loss exceeding 30%, or the emergence of agonal breathing. In both regimens, 100 mg/kg was chosen as it was the minimum dosage of gan-MΦ-NS leading to 100% of mice survival.

In vivo biosafety study

For the biosafety evaluation, gan-MΦ-NS (200 μL, 100 mg/kg, n = 3) were injected intravenously into the mice through the tail vein. At 7 d postinjection, the whole blood (~400 μL) was collected through the submandibular puncture and coagulated in an Eppendorf tube. After centrifugation at 3 k × g for 5 min, the serum was collected for comprehensive metabolic panel analysis. Meanwhile, 80 μL of whole blood was collected into an EDTA-coated anticoagulant microtube for the complete blood count. All blood samples were tested at the UCSD Animal Care Program Diagnostic Services Laboratory. Major organs, including the liver, heart, spleen, lungs, and kidneys, were harvested, fixed in 10% formalin for 24 h, and sectioned

for hematoxylin and eosin (H&E) staining. The UCSD Moores Cancer Center Tissue Technology Shared Resource performed histological preparation. Images were taken with a Micromaster II Microscope (Fisher Scientific).

3.1.7 Conclusion

In summary, this study focuses on utilizing glycan-modified MΦ cells to fabricate cellular CNPs and demonstrates that increasing their surface ganglioside expression is an effective strategy for enhancing the binding and neutralization of BoNT. MΦs play crucial roles in various diseases, and their unique properties enable MΦ CNPs to neutralize a wide range of biological agents [16]. Meanwhile, cell surface glycans serve as a major target for toxins or pathogens to gain entry into cells [50,51]. In this work, we achieved glycan modification by solely utilizing metabolic engineering without the need for additional biochemistry. Both in vitro and in vivo experiments showed that glycan-modified MΦ CNPs had superior efficacy in neutralizing BoNT as compared to the CNPs made from wild-type MΦ cell membrane. Notably, BoNT cellular entry requires the cooperation of two independent cellular receptors. While gangliosides are well-known as one of the receptors, the other receptor, likely specific to neuronal membrane, is still under investigation [52,53]. The complexity involved in understanding BoNT cellular entry poses challenges in the development of traditional BoNT countermeasures. However, the CNP platform offers a unique solution by effectively neutralizing BoNT regardless of its mechanisms of action, as the cellular CNPs capitalize on the shared functions of BoNT serotypes. Overall, this study demonstrates that combining CNP technique with cell surface glycan engineering holds great promise in the development of nanomedicines that can serve as broad-spectrum countermeasures against emerging threats posed by BoNT and other neurotoxins.

Chapter 3.1, in full, is a reprint of the material as it appears in *Journal of the American Chemical Society*, 2021, Xiangzhao Ai, Dan Wang, Anna Honko, Yaou Duan, Igor Gavrish, Ronnie H. Fang, Anthony Griffiths, Weiwei Gao, and Liangfang Zhang; The dissertation author was a major contributor and co-author of this paper.

3.1.8 References

[1] M. Pirazzini, O. Rossetto, R. Eleopra, C. Montecucco, Botulinum neurotoxins: biology, pharmacology, and toxicology, Pharmacological Reviews 69(2) (2017) 200-235.

[2] C. Verastegui, G. Lalli, S. Bohnert, F.A. Meunier, G. Schiavo, Clostridial neurotoxins, J. Toxicol., Toxin Reviews. 21(3) (2002) 203-227.

[3] L.L. Simpson, Identification of the major steps in botulinum toxin action, Annual Review of Pharmacology and Toxicology 44 (2004) 167-193.

[4] O. Cenciarelli, P.W. Riley, A. Baka, Biosecurity threat posed by botulinum toxin, Toxins (Basel) 11(12) (2019) 681.

[5] M. Pohanka, Botulinum toxin as a biological warfare agent: poisoning, diagnosis and countermeasures, Mini-Reviews in Medicinal Chemistry 20(10) (2020) 865-874.

[6] S.S. Arnon, R. Schechter, T.V. Inglesby, D.A. Henderson, J.G. Bartlett, M.S. Ascher, E. Eitzen, A.D. Fine, J. Hauer, M. Layton, S. Lillibridge, M.T. Osterholm, T. O'Toole, G. Parker, T.M. Perl, P.K. Russell, D.L. Swerdlow, K. Tonat, B. Working Grp Civilian, Botulinum toxin as a biological weapon - medical and public health management, Journal of the American Medical Informatics Association. 285(8) (2001) 1059-1070.

[7] J. Frevert, D. Dressler, Complexing proteins in botulinum toxin type A drugs: a help or a hindrance?, Biologics: Targets & Therapy 4 (2010) 325-332.

[8] P. Capek, T.J. Dickerson, Sensing the deadliest toxin: technologies for botulinum neurotoxin detection, Toxins (Basel) 2(1) (2010) 24-53.

[9] D.C. Hooper, M.S. Hirsch, Novel clostridium botulinum toxin and dual use research of concern issues, The Journal of Infectious Diseases 209(2) (2014) 167-167.

[10] E. Kiris, J.C. Burnett, C.D. Kane, S. Bavari, Recent advances in botulinum neurotoxin inhibitor development, Current Topics in Medicinal Chemistry 14(18) (2014) 2044-2061.

[11] B. Li, N.P. Peet, M.M. Butler, J.C. Burnett, D.T. Moir, T.L. Bowlin, Small molecule inhibitors as countermeasures for botulinum neurotoxin intoxication, Molecules 16(1) (2011) 202-220.

[12] M. Fabbri, G. Leodori, R.M. Fernandes, R. Bhidayasiri, M.J. Marti, C. Colosimo, J.J. Ferreira, Neutralizing antibody and botulinum toxin therapy: a systematic review and meta-analysis, Neurotoxicity Research 29(1) (2016) 105-117.

[13] J.M. Rusnak, L.A. Smith, Botulinum neurotoxin vaccines: past history and recent developments, Human Vaccines 5(12) (2009) 794-805.

[14] L.A. Smith, Botulism and vaccines for its prevention, Vaccine 27 (2009) D33-D39.

[15] R.H. Fang, A.V. Kroll, W. Gao, L. Zhang, Cell membrane coating nanotechnology, Advanced Materials 30(23) (2018) 1706759.

[16] S.Y. Wang, D. Wang, Y.O. Duan, Z.D. Zhou, W. Gao, L. Zhang, Cellular nanosponges for biological neutralization, Advanced Materials. 34(13) (2022) 2107719.

[17] C.M.J. Hu, L. Zhang, S. Aryal, C. Cheung, R.H. Fang, L. Zhang, Erythrocyte membrane-camouflaged polymeric nanoparticles as a biomimetic delivery platform, Proceedings of the National Academy of Sciences 108(27) (2011) 10980-10985.

[18] C.M.J. Hu, R.H. Fang, J. Copp, B.T. Luk, L. Zhang, A biomimetic nanosponge that absorbs pore-forming toxins, Nature Nanotechnology 8(5) (2013) 336-340.

[19] Y.J. Chen, M.C. Chen, Y. Zhang, J.H. Lee, T. Escajadillo, H. Gong, R.H. Fang, W. Gao, V. Nizet, L. Zhang, Broad-spectrum neutralization of pore-forming toxins with human erythrocyte membrane-coated nanosponges, Advanced. Healthcare. Matererials. 7(13) (2018) 1701366.

[20] Y.J. Chen, Y. Zhang, M.C. Chen, J. Zhuang, R.H. Fang, W. Gao, L. Zhang, Biomimetic nanosponges suppress in vivo lethality induced by the whole secreted proteins of pathogenic bacteria, Small 15(6) (2019) 1804994.

[21] Z.Q. Pang, C.M.J. Hu, R.H. Fang, B.T. Luk, W. Gao, F. Wang, E. Chuluun, P. Angsantikul, S. Thamphiwatana, W.Y. Lu, X.G. Jiang, L. Zhang, Detoxification of organophosphate poisoning using nanoparticle bioscavengers, ACS Nano 9(6) (2015) 6450-6458.

[22] Y.J. Chen, Z. Jia, J. Zhuang, J.H. Lee, L.C. Wang, R.H. Fang, W. Gao, L. Zhang, Cell-membrane-cloaked oil nanosponges enable dual-modal detoxification, ACS Nano 13(6) (2019) 7209-7215.

[23] Y. Jiang, R.H. Fang, L. Zhang, Biomimetic nanosponges for treating antibody-mediated autoimmune diseases, Bioconjugate Chemistry 29(4) (2018) 870-877.

[24] J.A. Copp, R.H. Fang, B.T. Luk, C.M.J. Hu, W. Gao, K. Zhang, L. Zhang, Clearance of pathological antibodies using biomimetic nanoparticles, Proceedings of the National Academy of Sciences 111(37) (2014) 13481-13486.

[25] Q.Z. Zhang, D. Dehaini, Y. Zhang, J.L. Zhou, X.Y. Chen, L. Zhang, R.H. Fang, W. Gao, L. Zhang, Neutrophil membrane-coated nanoparticles inhibit synovial inflammation and alleviate joint damage in inflammatory arthritis, Nature Nanotechnology. 13(12) (2018) 1182-1190.

[26] Y. Zhang, Y.J. Chen, C. Lo, J. Zhuang, P. Angsantikul, Q.Z. Zhang, X.L. Wei, Z.D. Zhou, M. Obonyo, R.H. Fang, W. Gao, L. Zhang, Inhibition of pathogen adhesion by bacterial outer membrane-coated nanoparticles, Angewandte Chemie International Edition58(33) (2019) 11404-11408.

[27] Q.Z. Zhang, A. Honko, J.R. Zhou, H. Gong, S.N. Downs, J.H. Vasquez, R.H. Fang, W. Gao, A. Griffiths, L. Zhang, Cellular nanosponges inhibit SARS-CoV-2 infectivity, Nano Letters 20(7) (2020) 5570-5574.

[28] X.Z. Ai, S.Y. Wang, Y.O. Duan, Q.Z. Zhang, M.S. Chen, W. Gao, L. Zhang, Emerging approaches to functionalizing cell membrane-coated nanoparticles, Biochemistry 60(13) (2021) 941-955.

[29] N. Krishnan, F.-X. Peng, A. Mohapatra, R.H. Fang, L. Zhang, Genetically engineered cellular nanoparticles for biomedical applications Biomaterials 296 (2023) 122065

[30] X.Z. Ai, D. Wang, A. Honko, Y.O. Duan, I. Gavrish, R.H. Fang, A. Griffiths, W. Gao, L. Zhang, Surface glycan modification of cellular nanosponges to promote SARS-CoV-2 inhibition, Journal of the American Chemical Society 143(42) (2021) 17615-17621.

[31] A. Rummel, K. Hafner, S. Mahrhold, N. Darashchonak, M. Holt, R. Jahn, S. Beermann, T. Karnath, H. Bigalke, T. Binz, Botulinum neurotoxins C, E and F bind gangliosides via a conserved binding site prior to stimulation-dependent uptake with botulinum neurotoxin F utilising the three isoforms of SV2 as second receptor, Journal of Neurochemistry 110(6) (2009) 1942-1954.

[32] S. Kozaki, Y. Kamata, S. Watarai, T. Nishiki, S. Mochida, Ganglioside GT1b as a complementary receptor component for Clostridium botulinum neurotoxins, Microbial Pathogenesis 25(2) (1998) 91-99.

[33] Q.Z. Zhang, J.L. Zhou, J.R. Zhou, R.H. Fang, W. Gao, L. Zhang, Lure-and-kill macrophage nanoparticles alleviate the severity of experimental acute pancreatitis, Nature Communication. 12(1) (2021) 4136.

[34] H. Barth, S. Fischer, A. Moglich, C. Fortsch, Clostridial C3 toxins target monocytes/macrophages and modulate their functions, Frontiers in Immunology 6 (2015) 339.

[35] C.T. Saeui, A.V. Nairn, M. Galizzi, C. Douville, P. Gowda, M. Park, V. Dharmarha, S.R. Shah, A. Clarke, M. Austin, K.W. Moremen, K.J. Yarema, Integration of genetic and metabolic features related to sialic acid metabolism distinguishes human breast cell subtypes, PLoS One 13(5) (2018) e0195812.

[36] S. Thamphiwatana, P. Angsantikul, T. Escajadillo, Q.Z. Zhang, J. Olson, B.T. Luk, S. Zhang, R.H. Fang, W. Gao, V. Nizet, L. Zhang, Macrophage-like nanoparticles concurrently absorbing endotoxins and proinflammatory cytokines for sepsis management, Proc. Natl. Acad. Sci. U. S. A. 114(43) (2017) 11488-11493.

[37] M.J. Porter, G.L. Zhang, R.L. Schnaar, Ganglioside extraction, purification and profiling, Journal of Visualized Experiments (169) (2021) e62385.

[38] C.M. Whitman, F. Yang, J.J. Kohler, Modified GM3 gangliosides produced by metabolic oligosaccharide engineering, Bioorganic & Medicinal Chemistry Letters 21(17) (2011) 5006-5010.

[39] M.A. Tegenge, H. Bohnel, F. Gessler, G. Bicker, Neurotransmitter vesicle release from human model neurons (NT2) is sensitive to botulinum toxin A, Cellular and Molecular Neurobiology 32(6) (2012) 1021-1029.

[40] B. Farrow, M. Wong, J. Malette, B. Lai, K.M. Deyle, S. Das, A. Nag, H.D. Agnew, J.R. Heath, Epitope targeting of tertiary protein structure enables target-guided synthesis of a potent in-cell inhibitor of botulinum neurotoxin, Angewandte Chemie International Edition 54(24) (2015) 7114-7119.

[41] L.W. Cheng, L.H. Stanker, T.D. Henderson, J.L. Lou, J.D. Marks, Antibody protection against botulinum neurotoxin intoxication in mice, Infection and Immunity 77(10) (2009) 4305-4313.

[42] E. Saxon, C.R. Bertozzi, Cell surface engineering by a modified Staudinger reaction, Science 287(5460) (2000) 2007-2010.

[43] E.J. Kim, S.G. Sampathkumar, M.B. Jones, J.K. Rhee, G. Baskaran, S. Goon, K.J. Yarema, Characterization of the metabolic flux and apoptotic effects of O-hydroxyl- and N-acyl-modified N-acetylmannosamine analogs in Jurkat cells, Journal of Biological Chemistry 279(18) (2004) 18342-18352.

[44] R.H. Fang, C.M.J. Hu, B.T. Luk, W. Gao, J.A. Copp, Y.Y. Tai, D.E. O'Connor, L. Zhang, Cancer cell membrane-coated nanoparticles for anticancer vaccination and drug delivery, Nano Letter 14(4) (2014) 2181-2188.

[45] E.H. Eylar, M.A. Madoff, O.V. Brody, J.L. Oncley, The contribution of sialic acid to the surface charge of the erythrocyte, The Journal of Biological Chemistry 237 (1962) 1992-2000.

[46] A. Chonn, P.R. Cullis, Ganglioside GM1 and hydrophilic polymers increase liposome circulation times by inhibiting the association of blood proteins, Journal of Liposome Research 2 (1992) 397-410.

[47] T. Zhang, S.L. Zhou, L. Kang, X. Luo, Y. Liu, Y.Z. Song, X.R. Liu, Y.H. Deng, The effect of monosialylganglioside mix modifying the PEGylated liposomal epirubicin on the accelerated blood clearance phenomenon, Asian Journal of Pharmaceutical Sciences 12(2) (2017) 134-142.

[48] B.C. Yowler, R.D. Kensinger, C.L. Schengrund, Botulinum neurotoxin A activity is dependent upon the presence of specific gangliosides in neuroblastoma cells expressing synaptotagmin I, Journal of Biological Chemistry 277(36) (2002) 32815-32819.

[49] S. Iwabuchi, Y. Kakazu, J.Y. Koh, K.M. Goodman, N.C. Harata, Examination of synaptic vesicle recycling using FM dyes during evoked, spontaneous, and miniature synaptic activities, Journal of Visualized Experiments (85) (2014) e50557.

[50] M. Cohen, Notable aspects of glycan-protein interactions, Biomolecules 5(3) (2015) 2056-2072.

[51] A. Rek, E. Krenn, A.J. Kungl, Therapeutically targeting protein-glycan interactions, British Journal of Pharmacology 157(5) (2009) 686-694.

[52] R. Jahn, Neuroscience - a neuronal receptor for botulinum toxin, Science 312(5773) (2006) 540-541.

[53] S.C. Zhang, G. Masuyer, J. Zhang, Y. Shen, D. Lundin, L. Henriksson, S.I. Miyashita, M. Martinez-Carranza, M. Dong, P. Stenmark, Identification and characterization of a novel botulinum neurotoxin, Nature Communication 8 (2017) 14130.

3.2 Surface glycan modification of CNPs to promote SARS-CoV-2 inhibition

3.2.1 introduction

The severe acute respiratory syndrome coronavirus 2 (SARS-CoV-2) is responsible for the current pandemic of coronavirus disease 2019 (COVID-19), a crisis with an unprecedented threat to global public health. [1-3] So far, the antiviral drugs such as remdesivir, [4] monoclonal antibodies such as bamlanivimab and etesevimab, [5] and vaccines manufactured by Pfizer-BioNTech, Moderna, and Janssen [6] have been approved as emergency-use authorization in the United States for COVID-19 treatment and prevention. However, SARS-CoV-2 can undergo genetic mutations over time, resulting in the unpredictable evolutions of new viral strains resistant to the current therapeutics or vaccines. [7-9] Therefore, innovative strategies that can inhibit the infectivity of SARS-CoV-2 and its potential mutated strains are highly demanded. Nanomedicine platforms have shown high potential in the diagnosis, treatment, and prevention of viral infections. [10-13] Among them, cell-membrane-coated nanoparticles, namely, “cellular nanosponges”, have attracted much attention. CNPs are made by cloaking plasma membranes of the host cells onto synthetic cores. They inherit natural protein and glycan receptors from the

host cells, either known or unknown, to bind with viral proteins and divert the viruses away from the intended cellular targets. [14] Such a working mechanism shifts the focus from the causative viruses to the hosts and thus overcomes virus diversity, limiting the traditional antiviral approach. CNPs effectively capture and inactivate pathogenic viruses such as human immunodeficiency virus (HIV), [15] influenza virus, [16] Zika virus, [17] and recently SARS-CoV-2, [18, 19] unlocking a broad-spectrum antiviral strategy.

During the infection, SARS-CoV-2 viruses use their spike-like proteins (S proteins) on the surface to attach to the cellular angiotensin-converting enzyme 2 (ACE2) for entering the host cells. Recent studies suggest that, before the ACE2 binding, the receptor-binding domain (RBD) of the viral S protein first interacts with the glycocalyx components of the membranes such as heparin or heparan sulfate (HS). [20] Such interactions lead to an open conformation of the S protein that enhances its subsequent binding to the ACE2. [21] This observation is further supported by SARS-CoV-2 inhibition in vitro using heparin or heparan sulfate. [22, 23] Therefore, alteration of heparan sulfate on the host cell surface presents potential therapeutic opportunities against SARS-CoV-2 infection.

3.2.2 Preparation and characterization of heparin-modified CNPs

Metabolic labeling of an azido group (N3) onto THP-1 cells, a human macrophage (MΦ) cell line, was achieved by incubating the cells with N-azidoacetylmannosamine-tetraacylated (Ac4ManNAz). In this process, Ac4ManNAz was metabolized into N-azidoacetyl neuraminic acid and then incorporated into glycans for expression. [24] To confirm the expression, we measured the N3 level on the cells before and after the incubation by tagging the N3 group with dibenzocyclooctyne-cyanine 3 (DBCO-Cy3) via copper-free click chemistry. The cell surface N3 level increased significantly when the cells were incubated with Ac4ManNAz (Figure 3.6A).

However, despite a high level of N3 expression, the cell viability showed no detectable change (Figure 3.6B).

After the N3 expression, we first derived the membranes of N3-expressing THP-1 cells and purified them using mechanical disruption and differential centrifugation. [25] Meanwhile, PLGA cores were made with a nanoprecipitation procedure by adding the polymer in an organic solvent to an aqueous phase followed by evaporation. [26] Then, cell membranes were coated onto PLGA cores with bath sonication, forming azido-expressing CNPs (denoted "N3-NS"). CNPs were also made with unmodified THP-1 cells (denoted "NS") as a control.

Following the formulation, dynamic light scattering (DLS) measurements revealed that NS and N3-NS had similar hydrodynamic diameters of 95.8 ± 3.6 and 99.7 ± 3.4 nm, respectively. These values are higher than that of the uncoated PLGA cores (82.7 ± 2.2 nm), suggesting the addition of a bi-layered cell membrane onto the polymeric cores (Figure 3.6C). Meanwhile, the surface zeta-potential of the N3-NS (−30.4 ± 1.9 mV) was less negative than that of the PLGA cores (−50.5 ± 1.4 mV) but comparable to that of the NS (−32.4 ± 2.2 mV) (Figure 3.6D), likely due to the charge screening by the membrane coating. To examine the membrane-sidedness, we stained the N3-expressing THP-1 source cells and N3-NS containing equal amounts of membrane content by using DBCO-Cy3 dye for the surface N3 levels. After removal of the free dye, the two samples showed comparable N3 levels (Figure 3.6E). This result indicated that the N3-NS adopted a right-side-out membrane orientation because an inside-out membrane coating would have reduced the levels of N3-labeled glycans. When suspended in water, phosphate-buffered saline (PBS, 1×), and 50% serum, the sizes of NS and N3-NS remained unchanged over 72 h, suggesting their good colloidal stability (Figure 2F). Together, these results demonstrated the successful preparation of N3-NS.

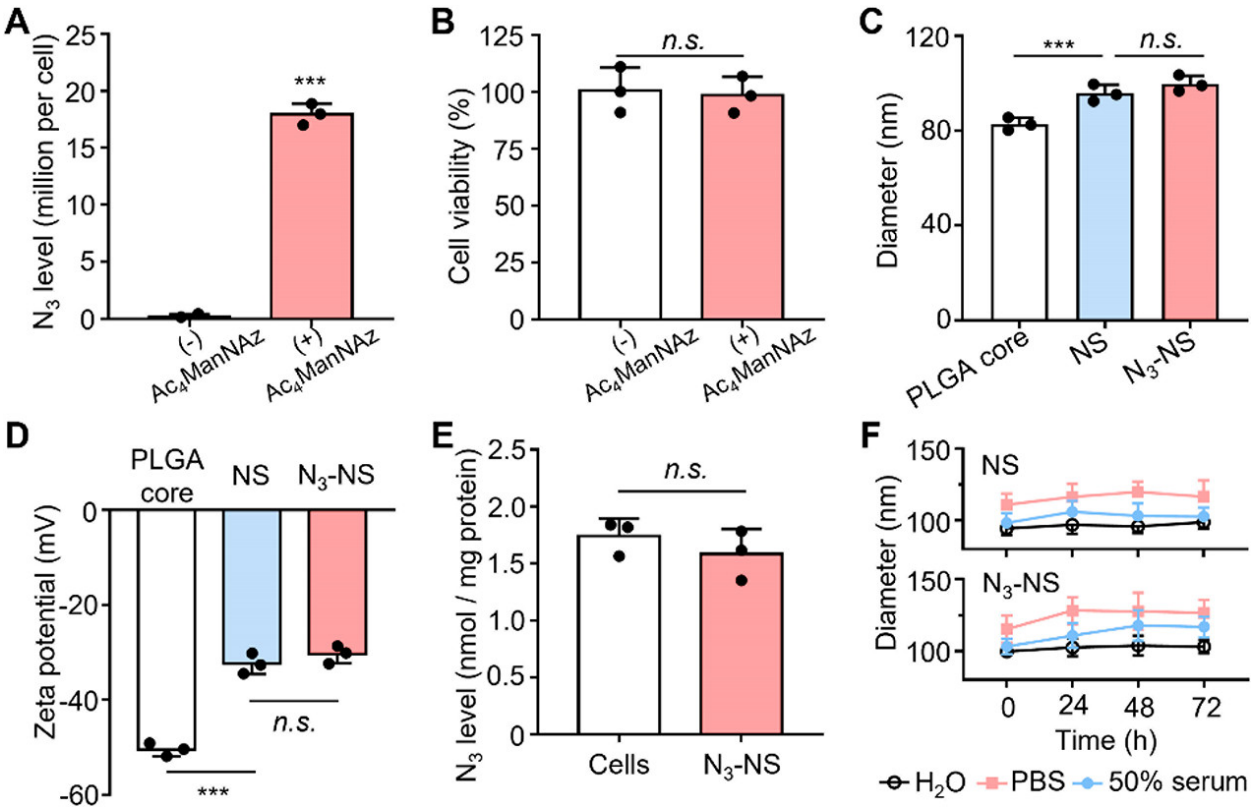

Figure 3.6 Formulation and characterization of N3-NS

(A) Surface N3 levels of the THP-1 cells cultured with or without Ac4ManNAz. (B) Cell viability of THP-1 cells cultured with or without Ac4ManNAz. (C, D) Hydrodynamic size (C, diameter) and surface zeta potential (D, mV) of the PLGA core, CNPs made with unmodified THP-1 membranes ("NS"), and N3-NS. (E) Comparison of the N3 levels on N3-NS (100 μL, 1 mg/mL of membrane proteins) and source cells (100 μL, approximately 1 × 107 cells) containing equal amounts of membrane content. The N3 levels were measured by staining the samples with DBCO-Cy3 (10 μM). (F) Hydrodynamic sizes of NS and N3-NS in H2O, 1× PBS, and 50% serum over 72 h. Data presented as mean + s.d. (n = 3); n.s.: not significant; ***$p < 0.001$; statistical analysis by paired t-test.

3.2.3 Enhanced binding of SARS-CoV-2 S protein by HP-NS

To fabricate HP-NS, we first functionalized heparin with DBCO by conjugating DBCO-NH2 to the carboxylic groups of the heparin, followed by purification with dialysis. In 1H NMR analysis, the product spectrum showed additional peaks around approximately 7.5 ppm, consistent with DBCO (Figure 3.7A). [27] When analyzed with UV absorption spectroscopy, the product showed DBCO absorption at about 290–310 nm (Figure 3.7B). [28] Moreover, in the

analysis with high-performance liquid chromatography (HPLC), the elution time of the DBCO signal (at 290 nm) from the product shifted when compared with that of DBCO-NH2, suggesting the conjugation to the heparin polymer chain (Figure 3.7C). Together, these results confirm the successful synthesis of DBCO-heparin. The DBCO density (the weight percentage of DBCO in the DBCO-functionalized heparin product) was determined to be 2.3 ± 0.1 wt % based on the UV absorption spectroscopy.

Next, we formulated HP-NS by conjugating DBCO-heparin onto N3-NS through a copper-free click chemistry reaction. When DBCO-heparin input was increased from 0 to 15 mg/mL, the heparin density on HP-NS increased but reached a plateau at an input of 10 mg/mL (Figure 3.7D). Based on this study, we selected three HP-NS formulations with low, middle, and high heparin densities (denoted “HP-NS/L”, “HP-NS/M”, and “HP-NS/H”, respectively). The heparin density of the three formulations (the weight percentage of the conjugated heparin compared to the total membrane protein weight) was 0.6, 3.8, and 6.8 wt %, respectively. Heparin conjugation had little effect on the HP-NS hydrodynamic sizes (Figure 3.7E). However, as the heparin content increased, the zeta potential of the nanoparticles became less negative, likely due to the increased contribution of the negative charge from the heparin backbone. In addition, all three HP-NS formulations showed excellent colloidal stability in water, 1× PBS, and 50% serum, respectively (Figure 3.7F).

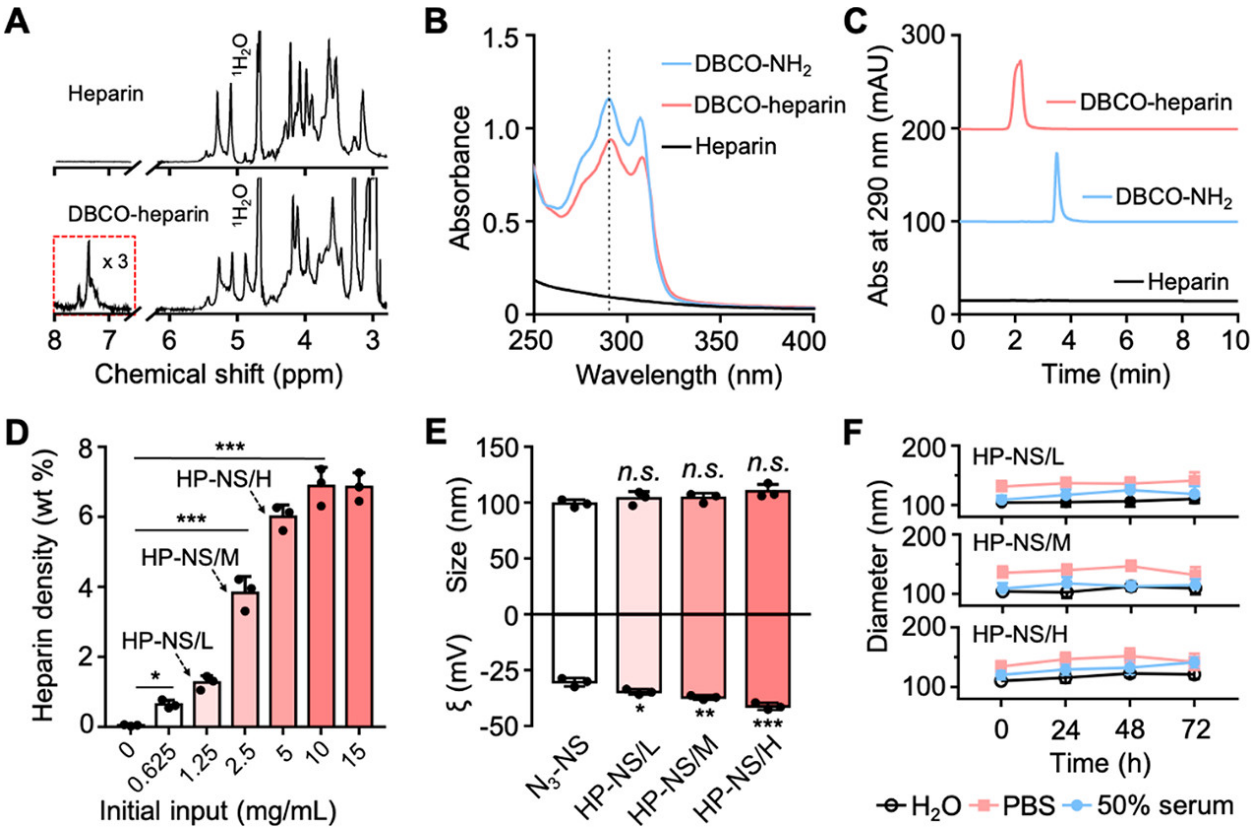

Figure 3.7 Fabrication and characterization of heparin-modified CNPs (HP-NS)

(A) 1H NMR spectrum (500 MHz) of heparin (top) and DBCO-heparin (bottom). The broad signal at 7–8 ppm corresponds to the DBCO moiety. (B, C) UV absorbance spectrum (B) and HPLC analysis (C) of heparin, DBCO-NH2, and DBCO-heparin. (D) Relationship between DBCO-heparin initial input and heparin density on NS surfaces. Three HP-NS formulations with low, middle, and high heparin densities (denoted "HP-NS/L", "HP-NS/M", and "HP-NS/H") were chosen for the subsequent studies. (E) DLS measurements of hydrodynamic size (diameter) and zeta potential (ζ) for N3-NS, HP-NS/L, HP-NS/M, and HP-NS/H. (F) Hydrodynamic size of HP-NS/L, HP-NS/M, and HP-NS/H in H_2O, 1× PBS, and 50% serum over 72 h. Data presented as mean + s.d. (n = 3); n.s.: not significant; ***$p < 0.001$; statistical analysis by one-way ANOVA.

3.2.4 Neutralization of SARS-CoV-2 pseudovirus infectivity by HP-NS

After formulating HP-NS, we then evaluated their binding capability with SARS-CoV-2 S proteins. In the study, serial dilutions of HP-NS were mixed with the S proteins (recombinant S1 subunit). After the incubation, HP-NS were removed with ultracentrifugation, and the unbound S protein concentration in the supernatant was quantified. As shown in Figure 3.8A,

when the amounts of HP-NS increased, the concentration of the unbound S protein decreased, suggesting a dose-dependent S protein neutralization of all three HP-NS formulations. At each HP-NS concentration, the amount of S proteins removed correlated with the heparin density on the HP-NS surfaces: the higher the heparin density was, the more S proteins were bound and removed. Based on these experimental results, we calculated the CNP concentrations needed to remove 50% of S proteins (denoted "IC50") under our experimental conditions (Figure 3.8B). We found that the IC50 values of N3-NS, HP-NS/L, HP-NS/M, and HP-NS/H were 2.69 ± 0.18, 1.60 ± 0.15, 0.80 ± 0.06, and 0.50 ± 0.02 mg/mL, respectively.

To verify that the enhanced S protein binding was indeed due to the surface-conjugated heparin, we treated HP-NS formulations (2 mg/mL) with heparinase that selectively cleaved the heparin (Figure 3.8C). After the enzyme digestion, the HP-NS were washed and collected by centrifugation. In the binding test, the HP-NS without the enzyme treatment showed S protein removal in correlation with their heparin density. In contrast, for all HP-NS formulations with heparinase treatment, S protein concentrations remained high and comparable to the baseline. This experiment confirms the specific role played by the conjugated heparin in binding and removing S proteins. CNPs made with THP-1 membranes inhibited SARS-CoV-2 infection by neutralizing multiple factors. For example, CNPs absorb S proteins through binding receptors such as ACE2 on the membrane. [29] Other receptors such as C type lectin domain family 10 (CLEC 10) and CD147 on the cell membrane may also bind with S proteins for removal. [30] Meanwhile, the membrane also contains various cytokine receptors such as CD120 for TNF-α. [31, 32] To confirm that heparin conjugation will not impact the binding capability of other cell membrane receptors on the CNP surface, we tested CNP binding with fluorescently labeled antibodies against proinflammatory cytokine receptors. In the study, phycoerythrin (PE)-labeled

anti-CD130 (IL-6 receptor), anti-CD120a (TNF-α receptor), and anti-CD119 (IFN-γ receptor) were incubated with HP-NS or N3-NS. After the incubation, the CNPs were removed. Supernatants from all HP-NS formulations showed fluorescence intensities comparable with that of N3-NS (Figure 3.8D). The results confirm that the heparin modification on the CNPs had a negligible impact on their inherent cytokine binding capabilities.

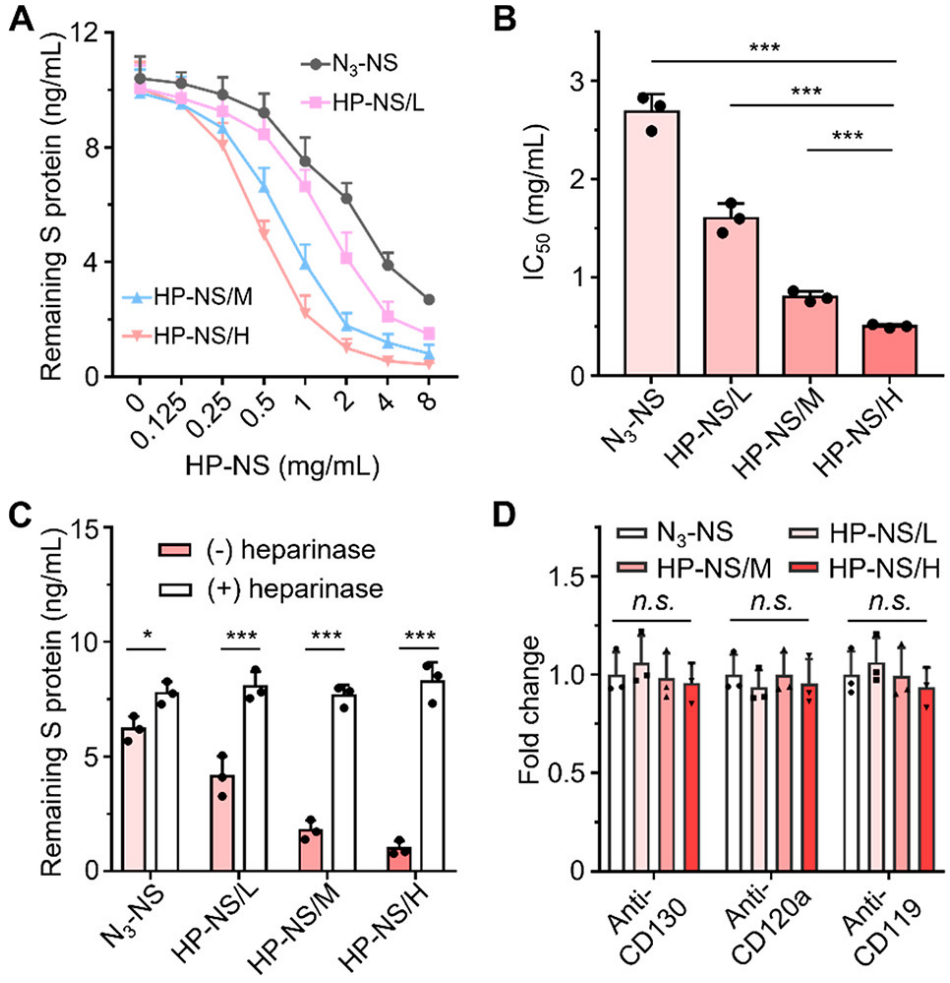

Figure 3.8 Enhanced binding of SARS-CoV-2 S protein by HP-NS.

(A) Dose-dependent binding of various HP-NS formulations with SARS-CoV-2 S proteins. The initial S protein concentration is 10 ng/mL. (B) Corresponding binding IC50 values calculated from (A). (C) S protein binding capacity of HP-NS with or without heparinase treatment. The initial S protein concentration was 10 ng/mL. (D) Comparison of CNP binding with antibodies against cell membrane surface receptors of three proinflammatory cytokines (IL-6, TNF-α, and IFN-γ). Data presented as mean + s.d. (n = 3); n.s.: not significant; ***$p < 0.001$; statistical analysis by one-way ANOVA.

3.2.5 Neutralization of live SARS-CoV-2 infectivity by HP-NS.

We next investigated the capability of HP-NS to inhibit SARS-CoV-2 pseudovirus infectivity. In the study, human lung epithelial cells were seeded in 96-well plates the day before the experiment. Serial dilutions of N3-NS or HP-NS and pseudotyped SARS-CoV-2 were added to the cell monolayers. After 24 h of incubation, the virus-infected cells were determined by the expression of genetically encoded green-fluorescent reporters inside the host cells. As shown in Figure 3.9A, control cells without adding the viruses or the CNPs showed no fluorescence. In contrast, cells added with viruses but not CNPs showed a strong green fluorescence, confirming the viral entry and infection in the epithelial cells. The fluorescence decreased obviously with the addition of N3-NS or HP-NS, suggesting the inhibition of viral infectivity by the CNPs. To quantify the inhibition of the infectivity, we varied the concentration of the CNPs added to the cell culture and measured the fluorescence intensity (Figure 3.9B). As the amounts of HP-NS increased, the fluorescence intensity from the host cells decreased, indicating a concentration-dependent inhibition effect. The percent of SARS-CoV-2 infectivity was correlated to the amounts of heparin on the HP-NS surfaces at all concentrations: the higher the heparin density, the less the SARS-CoV-2 infectivity. Based on these results, a half-maximal inhibitory concentration (IC50) of HP-NS to inhibit SARS-CoV-2 infectivity under our experimental conditions was calculated (Figure 3.9C). The IC50 values of N3-NS, HP-NS/L, HP-NS/M, and HP-NS/H were 193 ± 60, 43 ± 24, 17 ± 8, and 6 ± 3 mg/mL, respectively.

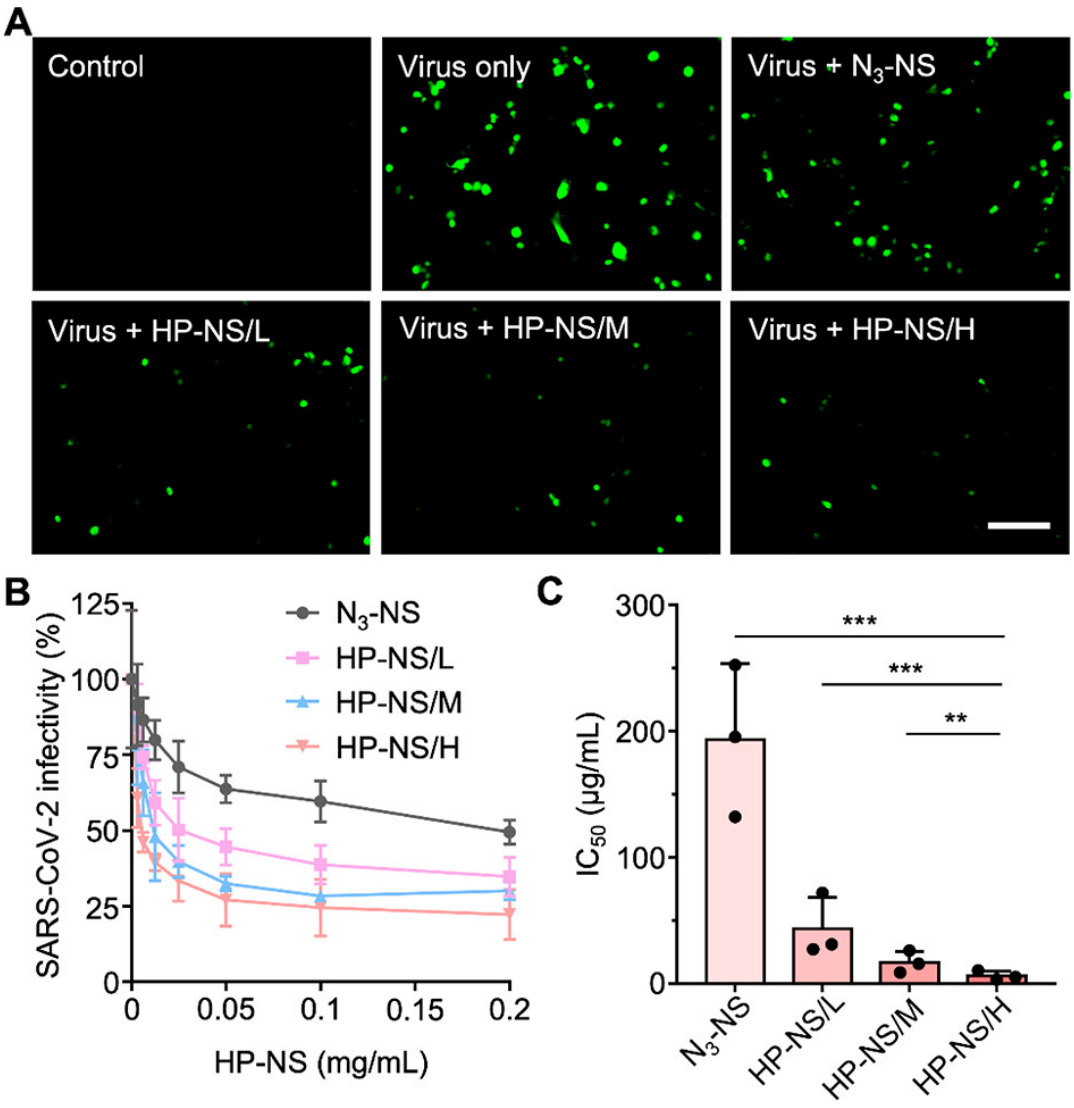

Figure 3.9 Neutralization of SARS-CoV-2 pseudovirus infectivity by HP-NS.

(A) Representative fluorescence images of NL-20 cells without or with HP-NS (25 μg/mL) under the infection of SARS-CoV-2 pseudovirus (5 × 107 viral genes per well) for 24 h. Green represents the fluorescent proteins in the nuclei (scale bars: 100 μm). (B) Dose-dependent inhibition of SARS-CoV-2 infectivity by N3-NS, HP-NS/L, HP-NS/M, and HP-NS/H. The cells with SARS-CoV-2 infection but without any treatment served as a control of 100% infectivity. (C) Corresponding inhibition IC50 values calculated from (B). Data presented as mean + s.d. (n = 3); n.s.: not significant; ***$p < 0.001$; statistical analysis by one-way ANOVA.

Finally, we evaluated the effects of heparin modification on CNP neutralization against live SARS-CoV-2 virus. Herein, we selected HP-NS/H (HP-NS lead formulation) and N3-NS (control group) to perform a plaque reduction neutralization assay. In the study, we first

amplified a low-passage sample of SARS-CoV-2 in Vero E6 cells to make a working stock of the virus. Then the Vero E6 cells were seeded at 8×10^5 cells per well in six-well plates the day before the experiment. In the experiment, serial half-log dilutions of the CNPs starting from 5 mg/mL were mixed with 200 plaque-forming units (PFU) of SARS-CoV-2. The mixture was incubated at 37 °C for 1 h and then added to the cell monolayers followed by another 1 h of incubation. Mock-infected and diluent-only infected wells served as negative and positive controls, respectively. Monolayers were overlaid and incubated for 2 days followed by viral plaque enumeration. Following the incubation, cultures without adding CNP samples showed a viral count comparable to that in the negative control, confirming viral entry and infection of the host cells. As shown in Figure 3.10A, inhibition of the infectivity increased as the concentration of N3-NS increased, suggesting a dose-dependent neutralization of the live virus. Based on the results, a half-maximal inhibitory concentration (IC50) value of 170 μg/mL for N3-NS was obtained. In parallel, a similar dose-dependent inhibition of the viral infectivity was observed with HP-NS/H (Figure 3.10B). In this case, an IC50 value of 0.0254 μg/mL was obtained. A significantly lower IC50 value of HP-NS/H indicates a much higher potency than N3-NS, confirming the effect of heparin modification on enhancing SARS-CoV-2 inhibition.

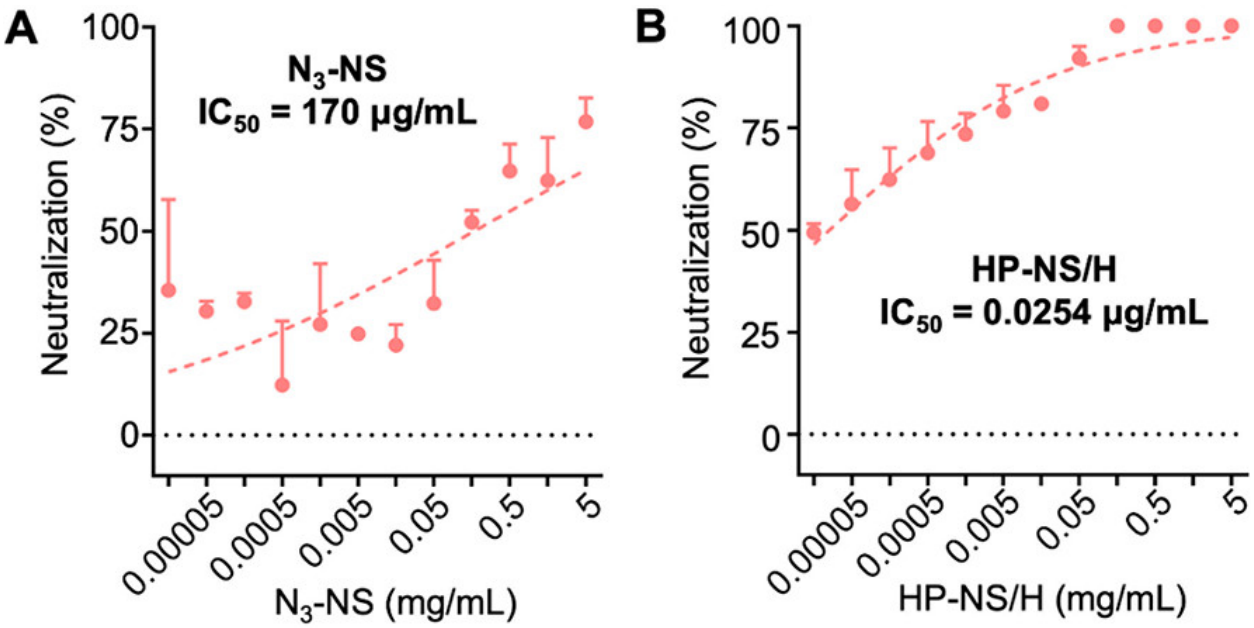

Figure 3.10 Neutralization of live SARS-CoV-2 infectivity by HP-NS. The neutralization against live SARS-CoV-2 infection by N3-NS (A) and HP-NS/H (B) was tested on Vero E6 cells. The IC50 values for N3-NS and HP-NS/H were determined to be 170 and 0.0254 µg/mL (membrane protein concentration), respectively. In all data sets, n = 3. Data are presented as mean + standard deviation. Horizontal dashed lines mark the zero levels. IC50 values were derived from the variable slope model using Graphpad Prism 8.

3.2.6 Methods

Metabolic labeling of azido groups (N3) on macrophages (MΦ). THP-1 cells, a human monocytic leukemia cell line, were obtained from American Type Culture Collection (ATCC, TIB-202), and cultured in RPMI 1640 medium supplemented with 10% fetal bovine serum (FBS) and 1% penicillin-streptomycin (all from Thermo Fisher Scientific). The cells were maintained at 37°C with 5% CO2 in a humidity-controlled incubator. For metabolic labeling, the cells were seeded in T175 suspension flasks (Olympus Plastics) at a density of 2×10^5 cells/mL, added with N-azidoacetylmannosamine-tetraacylated (Ac4ManNAz, Millipore-Sigma, final concentration 50 µM), and cultured for 72 h. After the culture, the cells were harvested by centrifugation at 800 ×g and washed three times with 1X PBS (pH = 7.4). To determine the N3 level on the membrane, cells were incubated with 10 µM dibenzocyclooctyne-cyanine 3 (DBCO-

Cy3, Millipore-Sigma, excitation = 540 nm, emission = 570 nm) for 1 h at 37 ^{o}C. After the incubation, the cells were washed with 1X PBS three times (centrifugation at 800 ×g) to remove the unreacted DBCO-Cy3. The cells were resuspended in 1X PBS at a concentration of 5×10^5 cells/mL. The fluorescence intensity of cell suspension was measured with a plate reader (TeCan Infinite M200). The average N3 amount on each cell was calculated by comparing the fluorescence intensity of cell suspension with DBCO-Cy3 solutions with known concentrations. The cell viability was determined by using a 3-(4,5-dimethylthiazol-2-yl)-5-(3-carboxymethoxyphenyl)-2-(4- sulfophenyl)-2H-tetrazolium (MTS) assay (BioVision) following the manufacturer's instruction. Cells without Ac4ManNAz treatment were used as the control group with 100% viability. Cells were stored at -80 ^{o}C for subsequent use.

Cell membrane derivation.

The MΦ membrane was harvested by following a previously published protocol. Briefly, frozen cells were thawed and washed with 1X PBS three times (centrifugation at 800 ×g). The cell pellet was resuspended in a hypotonic lysing buffer containing 30 mM Tris-HCl (pH = 7.5), 225 mM D-mannitol, 75 mM sucrose, 0.2 mM ethylene glycol-bis(β-aminoethyl ether)-N,N,N',N'-tetraacetic acid (EGTA), and a protease and phosphatase inhibitor cocktail (all reagents from Millipore-Sigma). Cells were then disrupted using a Kinematica Polytron PT 10/35 probe homogenizer (at 70% power and 20 passes). The homogenized solution was centrifuged at 20k ×g for 25 min at 4°C. The pellet was discarded, and the supernatant was centrifuged again at 100k ×g for 35 min at 4°C. The cell membranes were finally collected as the pellet and washed twice with 0.2 mM ethylenediaminetetraacetic acid (EDTA) in water. Membrane protein content was quantified by bicinchoninic acid (BCA) protein assay kit (Pierce, Thermo Fisher Scientific) and bovine serum albumin (BSA) as a standard reference.

Approximately 1×10^8 THP-1 cells were able to yield 1 mg of membrane material (protein weight). The membrane was suspended in 0.2 mM EDTA at 4 mg/mL (protein concentration) and stored at -80°C for subsequent studies.

Preparation and characterization of azido-modified cellular nanodecoys (N3-NS).

The cell membranes were coated onto polymeric cores by using a sonication method.1-2 Briefly, to synthesize the polymeric cores, 1 mL poly(DL-lactic-co-glycolic acid) (50:50 PLGA, 0.67 dl/g; Lactel Absorbable Polymers) in acetone (10 mg/mL) was added immediately into 2 mL water. The solution was placed below a vacuum aspirator until the acetone evaporated completely. For coating, unmodified or N3-labeled THP-1 membranes were mixed with PLGA cores at a polymer-to-membrane protein weight ratio of 1:1. The mixture was then sonicated in a bath sonicator (Thermo Fisher Scientific) for 2 minutes, resulting in NS and N3-NS, respectively. To determine the membrane sidedness, N3-NS was incubated with 10 μM DBCO-Cy3 (excitation/emission = 540/570 nm) for 1 h at 37 ^{o}C followed by centrifugation (20k ×g and 10 min) to pellet the nanoparticles. The pellet was washed with 1X PBS three times (centrifugation at 20k ×g) to remove the unreacted DBCO- Cy3, and further resuspended in 1X PBS (1 mg/mL) to measure the fluorescence intensity by a plate reader (TeCan Infinite M200). The fluorescence generated from N3-NS was compared to that from the equivalent number of azido-labeled cells. The hydrodynamic diameter and the surface zeta potential were measured with dynamic light scattering (DLS, Malvern ZEN 3600 Zetasizer). To study the long-term colloidal stability, nanoparticle suspensions were adjusted to 1X PBS or 50% serum at a final protein concentration of 0.5 mg/mL. Samples were stored at 37°C, and the hydrodynamic diameter was measured daily for three days.

Synthesis of DBCO-modified heparin (DBCO-heparin).

Heparin was conjugated with DBCO by following a previously published method. Briefly, 60 mg heparin sodium salt (Millipore-Sigma H3149, from porcine intestinal mucosa, average MW = 18 kDa) was dissolved in 1 mL 4-morpholineethanesulfonic acid (MES) buffer (50 mM, pH = 4.0), and the carboxylic acid groups were activated by adding 1-ethyl-3-(3-dimethylaminopropyl) carbodiimide hydrochloride (EDC, 65 mg) and N-hydroxysuccinimide (NHS, 38.5 mg) for 30 min. Then 0.55 mL DBCO-NH_2 in dimethylsulfoxide (DMSO, 10 mg/mL, all reagents from Millipore-Sigma) were added dropwise into the solution with stirring. After 24 h of the reaction, DBCO-heparin product was purified with dialysis in Slide-A-Lyzer MINI dialysis cups (with a 10 kDa molecular weight cut-off, Thermo Fisher Scientific) against 4 L DI water (3 days, replace the water once every 12 h). After the dialysis, the solution was lyophilized, and DBCO-heparin was obtained as white powders (38 mg, 63 wt% of yield, defined as the percentage of DBCO-heparin to the initial heparin input). Conjugation of DBCO to heparin was confirmed by 1H NMR (Varian INOVA-500M, Varian Inc., Palo Alto, USA) with deuterium oxide (D_2O, Millipore-Sigma) as the solvent. The amount of DBCO in the conjugates was determined by comparing the absorbance of DBCO-heparin at 290 nm with a standard curve consisting of various DBCO-NH_2 solutions with known concentrations. The conjugation and the purity of heparin-DBCO were also analyzed with a high-performance liquid chromatography (HPLC) system (Agilent 1220 Infinity II LC) using a C18 analytical column (Brownlee) and a mobile phase of acetonitrile in water starting at 5%(v/v) and ramping up to 40%(v/v) over 20 min. The flow rate was kept at 0.3 mL/min.

Preparation and characterization of heparin-modified CNPs (HP- NS).

The HP-NS were prepared by conjugating DBCO-heparin onto the N3-NS through a copper-free click chemistry reaction. Briefly, N3-NS suspensions (0.1 mL, 5 mg/mL in 1X PBS)

were mixed with 0.1 mL of DBCO-heparin solutions in 1X PBS. The mixtures had a N3- NS concentration of 2.5 mg/mL and DBCO-heparin concentrations of 0, 0.625, 1.25, 2.5, 5, 10, 15 mg/mL. The mixtures were placed on a shaker. After 2 h of reaction, nanoparticles were collected by centrifugation (20k ×g, 10 min at 4°C). The heparin concentration in the supernatant was quantified by a toluidine blue O (TBO) assay. Briefly, 50 μL of the supernatant was pipetted into a 96-well plate, followed by adding 50 μL of freshly TBO solution (Thermo Fisher Scientific, 100 μg/mL in 1X PBS). The absorbance at 630 nm was measured within one minute. The HP concentration was determined by comparing the absorbance with a standard curve made from various HP solutions of known concentrations. The amount of heparin conjugated onto HP-NS was calculated by subtracting the heparin in the supernatant from the initial heparin input. The value was used to calculate the heparin density.

Quantification of HP-NS binding with SARS-CoV-2 spike proteins (S proteins).

To study binding ability, recombinant SARS-CoV-2 spike protein S1 subunit (Sino Biological, 10 ng/mL) with a polyhistidine (His) tag at the C-terminus was mixed with HP-NS. The nanoparticle concentrations in the mixture ranged from 0 to 8 mg/mL. The mixtures were incubated for 2 h at 37°C and then centrifuged at 20k ×g for 10 min to pellet the nanoparticles. The S protein concentration in the supernatant was quantified by detecting the His-tag of the protein with an enzyme-linked immunosorbent assay (ELISA, GenScript Biotech). To verify the binding specificity, 10 units of heparinase I (New England Biolabs) were mixed with nanoparticles (2 mg/mL) in a reaction buffer containing 50 mM NaCl, 1 mM dithiothreitol, 1 mM $CaCl_2$, and 10 mM phosphate-citrate (pH = 6, all reagents from Millipore-Sigma). After 4 h of digestion, the nanoparticles were tested for binding with the S proteins using the same procedure as described above. To investigate the effect of heparin on membrane receptor

binding, CNPs were suspended in 1X PBS containing 1% BSA and added with phycoerythrin (PE)-labeled anti-CD119, anti-CD120a, or anti-CD130 (Biolegend). The volume of the mixture was 100 μL. The final concentration of the CNPs was kept at 5 mg/mL, and the concentration of the antibodies was 200 ng/mL. The mixtures were incubated for 30 min at 37°C. After the incubation, the CNPs were spun down by using centrifugation (20k ×g, 10 min). The fluorescence of the remaining PE-labeled antibodies in the supernatant was measured (excitation/emission = 550/575 nm). Their concentrations and bound antibodies were determined based on standard curves of the free antibodies.

Inhibition of SARS-CoV-2 pseudovirus infectivity.

Human lung epithelial cells (NL- 20) were obtained from ATCC (CRL-2503) and cultured in Ham's F-12 Medium (Invitrogen) supplemented with 4% FBS, 1% penicillin-streptomycin 0.1 mM nonessential amino acids, 1.5 g/L sodium bicarbonate, 2.7 g/L glucose, 5 μg/mL insulin, 10 ng/mL human epidermal growth factor, 10 μg/mL human transferrin, and 0.5 μg/mL hydrocortisone (all reagents from Millipore-Sigma). For pseudovirus inhibition studies, the NL-20 cells were seeded in a 96-well plate (Corning) at a density of 1.5×10^4 cells/well and maintained at 37°C with 5% CO_2 in a humidity-controlled incubator. After 24 h incubation, the culture media were replaced by 100 μL free media with serial dilutions of HP-NS ranged from 0 to 200 μg/mL. Then 50 μL free media containing 2.5 μL 2×10^{10} viral genes (VG)/mL SARS-CoV-2 pseudovirus (Montana Molecular) and 0.6 μL sodium butyrate (500 mM, Millipore-Sigma) were added to each well of the NL-20 cells. The plate was rocked gently 5-10 times to ensure uniform transduction across each well. After an additional 24 h incubation, the intensity of genetically encoded mNeonGreen fluorescent protein in the nucleus was determined by a microplate reader (excitation/emission = 485/515 nm), and the live-cell imaging was performed

using an EVOS inverted fluorescence microscope (Thermo Fisher Scientific). The percent inhibition of viral infectivity was calculated by comparing the fluorescence intensity of virus-only control wells with nanoparticles-treated wells at known concentrations.

Plaque reduction neutralization assay.

Vero E6 cells (BEI resources, NIAID, NIH: VERO C1008 (E6), African green monkey kidney, Working Bank #NR-596) were maintained in humidified incubators at 37°C and 5% CO2 in Dulbecco's modified Eagle medium (DMEM) with GlutaMAX and sodium pyruvate (Gibco) and 10% certified US- origin heat-inactivated fetal bovine serum (HI-FBS; Gibco). Cells were seeded on the day before the experiment at a density of 8×10^5 cells per well in 6-well plates. SARS-CoV-2 USA-WA1/2020 was propagated on Vero E6 cells in DMEM supplemented with GlutaMAX, sodium pyruvate, non-essential amino acids, Antibiotic-Antimycotic (Gibco), and 2% HI- FBS. The supernatant was harvested at 62 h and clarified by centrifugation, then the concentration of HI-FBS was brought up to 10% final concentration prior to cryopreservation at -80°C. The final passage was VERO+3, Vero E6+2. All experiments with infectious SARS-CoV-2 virus were performed under biosafety level-4 (BSL-4) conditions at the National Emerging Infectious Diseases Laboratories (NEIDL).

On the day of assay initiation, CNPs were vortexed for 10 seconds to resuspend and serially diluted by half-log in Dulbecco's PBS (Gibco) in a Nunc DeepWell polypropylene plate (Thermo Scientific) and covered with a sterile, breathable sealing film (CELLTREAT Scientific Products) for transport to biocontainment. SARS-CoV-2 was diluted in DMEM with GlutaMAX and sodium pyruvate supplemented with Antibiotic-Antimycotic and 2% HI-FBS to target 100 plaque-forming units (PFU) per well, and an equal volume added to the diluted test articles in the DeepWell plate. Samples were gently mixed and incubated for 1 h at 37°C before plating on 6-

well plates (200 μL in triplicate). Following 1 h incubation at 37°C with periodic rocking, a semi-solid overlay was added composed of a 1:1 mixture of 2× modified Eagle medium (Temin's modification; Gibco) supplemented with 10% HI-FBS, 2× GlutaMAX, and 2× Antibiotic-Antimycotic mixed with 2.5% Avicel RC-591 (kindly provided by DuPont Nutrition & Health) prepared in distilled water (Gibco). Plates were incubated for two days at 37°C and 5% CO2 and fixed with 10% neutral buffered formalin (Richard-Allan Scientific) for removal from biocontainment, where they were stained with a solution of 0.2% Gentian Violet (Ricca Chemical Company) and 10% neutral buffered formalin, rinsed, and then plaques were enumerated. Percent neutralization was calculated from virus-only control wells using the means of the triplicate wells. From these, the half-maximal inhibitory concentration values (IC50) were calculated in GraphPad Prism using a nonlinear regression from the log10 transformed concentrations. For these curves, the bottom was constrained to "constant equal to 0" and the top as "must be less than 100."

3.2.7 Conclusion

In summary, we showed that increasing the surface heparin density of CNPs promotes their binding capability with SARS-CoV-2 S proteins and enhances the potency of inhibiting viral infectivity. In our previous work, both wild-type THP-1 cell CNPs and lung epithelial cell CNPs inhibited SARS-CoV-2 infectivity with comparable potency. In the current study, we opted for THP-1 cells because their membranes were also able to neutralize various types of inflammatory cytokines, which would help suppress immune disorders in viral infections. Heparin has been shown to enhance S protein binding to ACE2, likely by stabilizing ACE2 during the virus-cell interactions, increasing the proportion of S proteins bound to ACE2, and increasing the occupancy of individual S proteins. Surface modification of CNPs brought heparin

to the proximity of ACE2, allowing the two moieties to cooperate and enhance binding to the viruses. The effect is remarkable, as reflected by over 3 orders of magnitude decrease of the IC50 value in live SARS-CoV-2 virus studies.

Besides SARS-CoV-2, other viruses such as dengue-2 virus, [33] Ebola virus, [34]) and Zika virus [35] also bind with heparin or heparin sulfate to initiate cell entry. The same glycoengineering approach is also applicable to other glycans such as terminal-linked sialic acid, known as the cellular receptors of viruses such as influenza virus, [36] Middle East respiratory syndrome coronavirus (MERS-CoV), [37] reovirus, [38] and rotavirus. [39] Therefore, increasing the density of these glycans is also anticipated to enhance viral inhibition by the CNPs. Previous studies using synthetic glycan nanoparticles showed that nanoparticle size and shape affect interligand spacing and thus affect nanoparticle–virus binding affinity. CNPs are expected to have similar properties. Therefore, optimizing CNP size and shape can be a way to modulate virus binding affinity toward neutralizing different viruses. Specific for lung delivery, some other factors to consider include the margination effect and lung deposition efficiency of the CNPs. Previous studies also showed the in vivo capability of macrophage CNPs (made with mouse J774 macrophages) to target multiple organs, including the lungs after intravenous or intraperitoneal injections. Membrane vesicles made from THP-1 macrophages were also tested for inhalation to inhibit SARS-CoV-2 infection. Based on these prior studies, we expect that different CNP formulations can be developed for various administration routes, including intravenous injection to neutralize plasma virus and inhalation to target damaged organs such as the lungs. Overall, combining the surface glycan engineering technology with the CNPs antiviral technology can create new opportunities for developing potent and broad-spectrum antiviral therapeutics.

Chapter 3.2, in full, is a reprint of the material as it appears in *Biomaterials*, 2023, Xiangzhao Ai, Dan Wang, Ilkoo Noh, Yaou Duan, Zhidong Zhou, Nilesh Mukundan, Ronnie H. Fang, Weiwei Gao, Liangfang Zhang. The dissertation author was a major contributor and co-author of this paper.

3.2.8 References

[1] N. Zhu, D. Zhang, W. Wang, X. Li, B. Yang, J. Song, X. Zhao, B. Huang, W. Shi, R. Lu, A novel coronavirus from patients with pneumonia in China, 2019, New England journal of medicine 382(8) (2020) 727-733.

[2] N.J. Matheson, P.J. Lehner, How does SARS-CoV-2 cause COVID-19?, Science 369(6503) (2020) 510-511.

[3] F. Zhou, T. Yu, R. Du, G. Fan, Y. Liu, Z. Liu, J. Xiang, Y. Wang, B. Song, X. Gu, Clinical course and risk factors for mortality of adult inpatients with COVID-19 in Wuhan, China: a retrospective cohort study, The lancet 395(10229) (2020) 1054-1062.

[4] J.H. Beigel, K.M. Tomashek, L.E. Dodd, A.K. Mehta, B.S. Zingman, A.C. Kalil, E. Hohmann, H.Y. Chu, A. Luetkemeyer, S. Kline, Remdesivir for the treatment of Covid-19—preliminary report, New England Journal of Medicine 383(19) (2020) 1813-1836.

[5] H. Ledford, COVID ANTIBODY TREATMENTS SHOW PROMISE, Nature 591(7851) (2021) 513-514.

[6] J.-L. Excler, M. Saville, S. Berkley, J.H. Kim, Vaccine development for emerging infectious diseases, Nature medicine 27(4) (2021) 591-600.

[7] A. Fontanet, B. Autran, B. Lina, M.P. Kieny, S.S.A. Karim, D. Sridhar, SARS-CoV-2 variants and ending the COVID-19 pandemic, The Lancet 397(10278) (2021) 952-954.

[8] P. Wang, M.S. Nair, L. Liu, S. Iketani, Y. Luo, Y. Guo, M. Wang, J. Yu, B. Zhang, P.D. Kwong, Antibody resistance of SARS-CoV-2 variants B. 1.351 and B. 1.1. 7, Nature 593(7857) (2021) 130-135.

[9] T.C. Williams, W.A. Burgers, SARS-CoV-2 evolution and vaccines: cause for concern?, The Lancet Respiratory Medicine 9(4) (2021) 333-335.

[10] S. Talebian, G.G. Wallace, A. Schroeder, F. Stellacci, J. Conde, Nanotechnology-based disinfectants and sensors for SARS-CoV-2, Nature nanotechnology 15(8) (2020) 618-621.

[11] M.D. Shin, S. Shukla, Y.H. Chung, V. Beiss, S.K. Chan, O.A. Ortega-Rivera, D.M. Wirth, A. Chen, M. Sack, J.K. Pokorski, COVID-19 vaccine development and a potential nanomaterial path forward, Nature nanotechnology 15(8) (2020) 646-655.

[12] Z. Tang, N. Kong, X. Zhang, Y. Liu, P. Hu, S. Mou, P. Liljeström, J. Shi, W. Tan, J.S. Kim, A materials-science perspective on tackling COVID-19, Nature Reviews Materials 5(11) (2020) 847-860.

[13] J. Zhou, N. Krishnan, Y. Jiang, R.H. Fang, L. Zhang, Nanotechnology for virus treatment, Nano Today 36 (2021) 101031.

[14] L. Rao, R. Tian, X. Chen, Cell-membrane-mimicking nanodecoys against infectious diseases, ACS nano 14(3) (2020) 2569-2574.

[15] X. Wei, G. Zhang, D. Ran, N. Krishnan, R.H. Fang, W. Gao, S.A. Spector, L. Zhang, T‐cell‐mimicking nanoparticles can neutralize HIV infectivity, Advanced Materials 30(45) (2018) 1802233.

[16] H.-W. Chen, Z.-S. Fang, Y.-T. Chen, Y.-I. Chen, B.-Y. Yao, J.-Y. Cheng, C.-Y. Chien, Y.-C. Chang, C.-M.J. Hu, Targeting and enrichment of viral pathogen by cell membrane cloaked magnetic nanoparticles for enhanced detection, ACS applied materials & interfaces 9(46) (2017) 39953-39961.

[17] L. Rao, W. Wang, Q.F. Meng, M. Tian, B. Cai, Y. Wang, A. Li, M. Zan, F. Xiao, L.L. Bu, G. Li, A. Li, Y. Liu, S.S. Guo, X.Z. Zhao, T.H. Wang, W. Liu, J. Wu, A Biomimetic Nanodecoy Traps Zika Virus To Prevent Viral Infection and Fetal Microcephaly Development, Nano Lett 19(4) (2019) 2215-2222.

[18] Q. Zhang, A. Honko, J. Zhou, H. Gong, S.N. Downs, J.H. Vasquez, R.H. Fang, W. Gao, A. Griffiths, L. Zhang, Cellular Nanosponges Inhibit SARS-CoV-2 Infectivity, Nano Lett 20(7) (2020) 5570-5574.

[19] C. Wang, S. Wang, Y. Chen, J. Zhao, S. Han, G. Zhao, J. Kang, Y. Liu, L. Wang, X. Wang, Y. Xu, S. Wang, Y. Huang, J. Wang, J. Zhao, Membrane Nanoparticles Derived from ACE2-Rich Cells Block SARS-CoV-2 Infection, ACS Nano 15(4) (2021) 6340-6351.

[20] T.M. Clausen, D.R. Sandoval, C.B. Spliid, J. Pihl, H.R. Perrett, C.D. Painter, A. Narayanan, S.A. Majowicz, E.M. Kwong, R.N. McVicar, B.E. Thacker, C.A. Glass, Z. Yang, J.L. Torres, G.J. Golden, P.L. Bartels, R.N. Porell, A.F. Garretson, L. Laubach, J. Feldman, X. Yin, Y. Pu, B.M. Hauser, T.M. Caradonna, B.P. Kellman, C. Martino, P. Gordts, S.K. Chanda, A.G. Schmidt, K. Godula, S.L. Leibel, J. Jose, K.D. Corbett, A.B. Ward, A.F. Carlin, J.D. Esko, SARS-CoV-2 Infection Depends on Cellular Heparan Sulfate and ACE2, Cell 183(4) (2020) 1043-1057.e15.

[21] C. Mycroft-West, D. Su, S. Elli, Y. Li, S. Guimond, G. Miller, J. Turnbull, E. Yates, M. Guerrini, D. Fernig, The 2019 coronavirus (SARS-CoV-2) surface protein (Spike) S1 Receptor Binding Domain undergoes conformational change upon heparin binding, BioRxiv (2020) 2020.02. 29.971093.

[22] P.S. Kwon, H. Oh, S.-J. Kwon, W. Jin, F. Zhang, K. Fraser, J.J. Hong, R.J. Linhardt, J.S. Dordick, Sulfated polysaccharides effectively inhibit SARS-CoV-2 in vitro, Cell discovery 6(1) (2020) 50.

[23] R. Tandon, J.S. Sharp, F. Zhang, V.H. Pomin, N.M. Ashpole, D. Mitra, M.G. McCandless, W. Jin, H. Liu, P. Sharma, Effective inhibition of SARS-CoV-2 entry by heparin and enoxaparin derivatives, Journal of Virology 95(3) (2021) 10.1128/jvi. 01987-20.

[24] Y. Takayama, K. Kusamori, M. Nishikawa, Click chemistry as a tool for cell engineering and drug delivery, Molecules 24(1) (2019) 172.

[25] R.H. Fang, C.-M.J. Hu, B.T. Luk, W. Gao, J.A. Copp, Y. Tai, D.E. O'Connor, L. Zhang, Cancer cell membrane-coated nanoparticles for anticancer vaccination and drug delivery, Nano letters 14(4) (2014) 2181-2188.

[26] C.-M.J. Hu, L. Zhang, S. Aryal, C. Cheung, R.H. Fang, L. Zhang, Erythrocyte membrane-camouflaged polymeric nanoparticles as a biomimetic delivery platform, Proceedings of the National Academy of Sciences 108(27) (2011) 10980-10985.

[27] J. Xu, E. Feng, J. Song, Bioorthogonally cross-linked hydrogel network with precisely controlled disintegration time over a broad range, Journal of the American Chemical Society 136(11) (2014) 4105-4108.

[28] K. Barker, S.K. Rastogi, J. Dominguez, T. Cantu, W. Brittain, J. Irvin, T. Betancourt, Biodegradable DNA-enabled poly (ethylene glycol) hydrogels prepared by copper-free click chemistry, Journal of Biomaterials Science, Polymer Edition 27(1) (2016) 22-39.

[29] R. Yan, Y. Zhang, Y. Li, L. Xia, Y. Guo, Q. Zhou, Structural basis for the recognition of SARS-CoV-2 by full-length human ACE2, Science 367(6485) (2020) 1444-1448.

[30] F. Qi, S. Qian, S. Zhang, Z. Zhang, Single cell RNA sequencing of 13 human tissues identify cell types and receptors of human coronaviruses, Biochemical and biophysical research communications 526(1) (2020) 135-140.

[31] L. Rao, S. Xia, W. Xu, R. Tian, G. Yu, C. Gu, P. Pan, Q.-F. Meng, X. Cai, D. Qu, Decoy nanoparticles protect against COVID-19 by concurrently adsorbing viruses and inflammatory cytokines, Proceedings of the National Academy of Sciences 117(44) (2020) 27141-27147.

[32] T. Hehlgans, K. Pfeffer, The intriguing biology of the tumour necrosis factor/tumour necrosis factor receptor superfamily: players, rules and the games, Immunology 115(1) (2005) 1-20.

[33] Y.-L. Lin, H.-Y. Lei, Y.-S. Lin, T.-M. Yeh, S.-H. Chen, H.-S. Liu, Heparin inhibits dengue-2 virus infection of five human liver cell lines, Antiviral research 56(1) (2002) 93-96.

[34] M. Tamhankar, D.M. Gerhardt, R.S. Bennett, N. Murphy, P.B. Jahrling, J.L. Patterson, Heparan sulfate is an important mediator of Ebola virus infection in polarized epithelial cells, Virology journal 15 (2018) 1-12.

[35] S. Ghezzi, L. Cooper, A. Rubio, I. Pagani, M.R. Capobianchi, G. Ippolito, J. Pelletier, M.C.Z. Meneghetti, M.A. Lima, M.A. Skidmore, Heparin prevents Zika virus induced-cytopathic effects in human neural progenitor cells, Antiviral research 140 (2017) 13-17.

[36] S.-J. Kwon, D.H. Na, J.H. Kwak, M. Douaisi, F. Zhang, E.J. Park, J.-H. Park, H. Youn, C.-S. Song, R.S. Kane, Nanostructured glycan architecture is important in the inhibition of influenza A virus infection, Nature nanotechnology 12(1) (2017) 48-54.

[37] W. Li, R.J. Hulswit, I. Widjaja, V.S. Raj, R. McBride, W. Peng, W. Widagdo, M.A. Tortorici, B. Van Dieren, Y. Lang, Identification of sialic acid-binding function for the Middle East respiratory syndrome coronavirus spike glycoprotein, Proceedings of the National Academy of Sciences 114(40) (2017) E8508-E8517.

[38] J.L. Connolly, E.S. Barton, T.S. Dermody, Reovirus binding to cell surface sialic acid potentiates virus-induced apoptosis, Journal of virology 75(9) (2001) 4029-4039.

[39] P. Isa, C.F. Arias, S. López, Role of sialic acids in rotavirus infection, Glycoconjugate journal 23 (2006) 27-37.

Chapter 4 Cell membrane based nanodiscs for broad spectrum neutralization

4.1 Synthesis of Erythrocyte Nanodiscs for Bacterial Toxin Neutralization

4.1.1 introduction

Nanodiscs (NDs) are small discoidal lipid bilayers enclosed by membrane scaffolding stabilizers. [1, 2] Typical NDs are sub-20 nm in diameter, and common stabilizers include membrane scaffold proteins, [3] peptides, [4] and synthetic polymers. [5] The unique disc-like structure allows NDs to reduce phagocytosis by the reticuloendothelial system compared to their spherical counterparts. [6-8] This feature makes NDs attractive for the targeted delivery of antitumor, antivirus, and antibacterial drugs. [9-11] Due to their small size and disc shape, NDs can penetrate draining lymph nodes effectively and thus become appealing nanovaccine formulations. [12, 13] Additionally, typical ND synthesis involves simple solubilization and reconstitution of lipid bilayer membranes, making their manufacturing scalable. [14] With these advantages, NDs have recently gained increasing attention as a versatile nanomedicine platform. [15-17]

So far, most ND formulations are made with synthetic lipid bilayers. [18, 19] For a specific application, the formulation requires careful optimization of lipid composition. [20] However, rational lipid selection approaches still need to be improved, and the trial-and-error approach may only sometimes lead to a desirable outcome. [21, 22] Meanwhile, some synthetic lipids can impose immune risks, limiting ND applications. [23, 24] In this perspective, we wonder whether NDs can be made with natural cell membranes consisting of native lipids, proteins, and their associated biological functions. By fabricating cellular NDs that do not involve synthetic lipid bilayers or post-synthesis functionalization, we hypothesize that these cellular NDs can inherit native cell membrane functions for broad therapeutic applications. [25,

26] In fact, an ND formulation was recently made directly from the bacterial outer membrane. With their small size and disc shape, the bacterial NDs were transported to the lymph nodes rapidly and interacted with antigen-presenting cells effectively. As a result, they presented the native bacterial antigens to the immune system and mounted effective antibacterial immunity. To test our broad hypothesis of cellular NDs, here we use human red blood cell (RBC) membrane to synthesize NDs (denoted "RBC-NDs") and apply them for detoxification against bacterial toxins (Figure 4.1A). RBC-NDs are synthesized by mixing the RBC membrane with amphiphilic scaffold copolymer styrene-maleic acid (SMA) at optimized stoichiometry. RBC-NDs provide natural membrane lipids and proteins that can absorb and trap bacterial toxins, preventing them from attacking the host cells. The toxin neutralization studies are carried out with two RBC susceptible bacterial toxin samples: (a) purified α-toxins from methicillin-resistant Staphylococcus aureus (MRSA) as a known model toxin, and (b) whole secreted proteins (wSP) from MRSA bacteria as a complex toxin sample containing known and unknown bacterial toxins. [27-29] In vitro studies show that RBC-NDs inhibit effectively toxin-induced hemolysis and cytotoxicity. In vivo studies reveal significant survival benefits from RBC-NDs to mice challenged by both purified bacterial toxin and wSP. Overall, this work demonstrates the feasibility of preparing RBC-NDs and using such cellular NDs for therapeutic applications.

4.1.2 Preparation and characterizatio of RBC-NDs

To determine the reaction stoichiometry, we gradually increased the membrane-to-SMA weight ratios. The nanodisc yield was quantified by measuring the membrane protein content in the retentate divided by the membrane protein input, which was found to increase accordingly and reach a plateau at a membrane-to-SMA ratio of 1 : 5 (Figure 4.1B). We chose this ratio to prepare the RBC-NDs for all subsequent experiments. Upon mixing with SMALP200, the RBC

membrane vesicle size decreased significantly, suggesting the transformation of larger membrane vesicles (132.5±3.7 nm) to much smaller RBC-NDs (18.7±2.9 nm) (Figure 4.1C). Meanwhile, the zeta potential values measured from the RBC-NDs and the membrane vesicles are comparable, implying the preservation of the cellular proteins and surface properties. Transmission electron microscopy (TEM) revealed disc-shaped nanoparticles with a homogeneous size distribution, similar to previous SMA-stabilized synthetic lipid nanodiscs and bacterial membrane nanodiscs (Figure 4.1D). [30]

These results indicate the successful synthesis of RBC-NDs. For the stability test, RBC-ND samples were stored in 1X phosphate-buffered saline (PBS) at 4 °C for 14 days and 50 % fetal bovine serum (FBS) at 37 °C for 72 h (Figure 4.1E). We observed little change in RBC-ND size in both studies, indicating good buffer storage stability and biostability.

We next investigated RBC-ND pharmacokinetic and biodistribution profiles in mice. For the pharmacokinetic study, we labeled RBC-NDs with Alexa Fluor® 647 and injected the fluorescently labeled samples via the tail vein (10 mg kg−1 membrane protein, n=6). We collected blood samples at a series of time points within 48 h. When fitted with a two-compartment model, the pharmacokinetic profile shows a circulation half-time of 15.2 h (Figure 4.1F). [31, 32] For the biodistribution study, we also injected fluorescently labeled RBC-NDs into mice through the tail vein (10 mg kg^{-1} membrane protein, n=6) and measured the fluorescence values of the heart, liver, spleen, lung, kidney, and blood. As shown in Figure 1G, the liver and spleen, the two major reticuloendothelial system (RES) organs, emitted the strongest signal. A significant fluorescence level was also observed in the blood at all time points. As the blood fluorescence decreased, the fluorescence in the liver increased. Such correlation indicates that the RES is primarily responsible for clearing the RBC-

NDs.

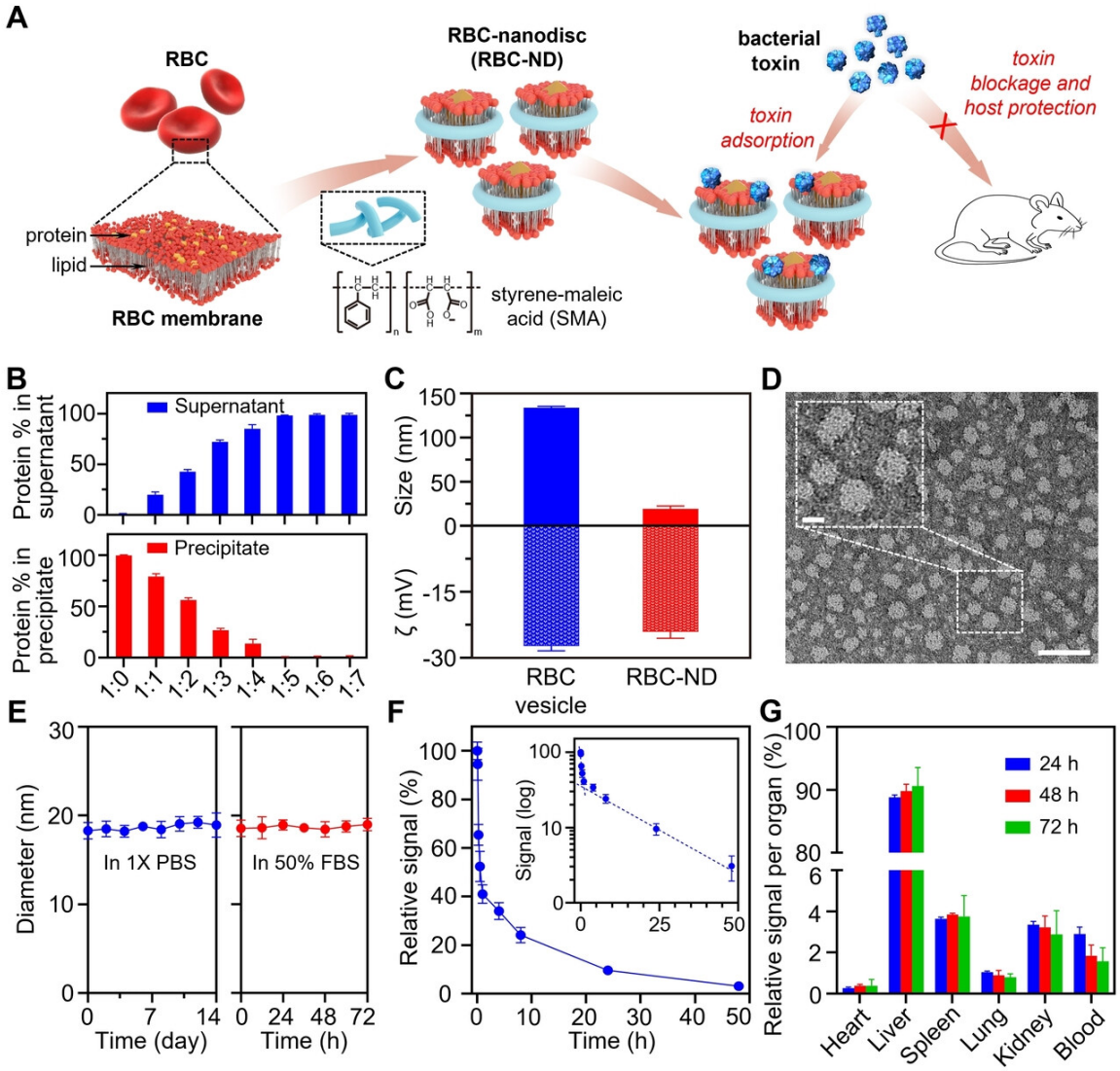

Figure 4.1Preparation and characterization of human red blood cell nanodiscs (RBC-NDs).

A) Schematic preparation of RBC-NDs and their mechanism of neutralizing bacterial toxins. B) Yield (% protein in supernatant) and loss (% protein in precipitate) at different weight ratios of RBC membrane protein to SMA copolymer. C) Dynamic light scattering measurements of size (diameter) and zeta potential (mV) of RBC membrane vesicles and RBC-NDs. D) Transmission electron microscopy (TEM) image of RBC-NDs (scale bar: 50 nm). Insert: a zoom-in view of RBC-NDs (scale bar:10 nm) (E) Stability of RBC-NDs in 1X PBS at 4 °C for 14 days and 50 % fetal bovine serum (FBS) at 37 °C for 72 hours. F) Pharmacokinetic profile of RBC-NDs after intravenous injection of Alexa Fluor® 647-labeled RBC-NDs (10 mg kg^{-1}, membrane protein). G) Biodistribution of RBC-NDs in mice at 24, 48, and 72 h after intravenous injection. In all studies, n=3. Data in B, C, and G are presented as mean ± standard deviation. Data in E and F are presented as mean+standard deviation.

4.1.3 Neutralization of α-toxin and wSP *in vitro*

Following the formulation and characterization studies of RBC-NDs, we investigated their neutralization against α-toxin in vitro. To establish the hemolytic activity of α-toxin, we varied the toxin concentration and measured the hemolysis. The percent hemolysis of α-toxin followed a sigmoidal curve as a function of the log of the toxin concentration. We found that 8 $\mu g\ mL^{-1}$ α-toxin caused complete RBC lysis (HD100, Figure 4.2A). We then used this concentration in the subsequent neutralization studies. As shown in Figure 2B, we first used a preincubation regimen, where various concentrations of RBC-NDs were mixed with α-toxin and then added to RBCs. The RBC-ND concentration that inhibited half of the hemolysis (IC50) is 0.21 $\mu g\ mL^{-1}$, and 2 $\mu g\ mL^{-1}$ was needed to inhibit the hemolysis (IC100, preincubation) completely. Then, we used a competitive regimen to evaluate the neutralization efficiency, where variousconcentrations of RBC-NDs were mixed with RBCs and then added with α-toxin. The IC50 and IC100 values of RBC-NDs were 0.85 $\mu g\ mL^{-1}$ and 16 $\mu g\ mL^{-1}$, respectively. These results demonstrated that RBC-NDs effectively neutralized the membrane lysis activity of α-toxin. We next investigated RBC-NDs against α-toxin-induced cytotoxicity on human umbilical vein endothelial cells (HUVECs). To establish the cytotoxicity profile of α-toxin, we varied the toxin concentration and measured the cell viability. The value followed a sigmoidal curve as a function of the log of the toxin concentration where 4 $\mu g\ mL^{-1}$ α-toxin caused 100 % cell death (EC100, Figure 4.2C). We then carried out the neutralization in a preincubation regimen, where various concentrations of RBC-NDs were first mixed with α-toxin (4 $\mu g\ mL^{-1}$). Then the mixtures were added to HUVECs. As shown in Figure 4.2D, RBC-NDs showed a dose-dependence neutralization against α-toxin, and the neutralization followed a typical sigmoidal

profile. HUVEC viability was 50 % and 100 % when the RBC-ND concentrations were 0.13 μg mL^{-1} (IC50) and 1 μg mL^{-1} (IC100), respectively. We also conducted the study in a competitive regimen, where RBC-NDs were first mixed with HUVECs, followed by α-toxin addition. In this case, RBC-NDs showed an IC50 value of 0.77±0.05 μg mL−1 and an IC100 value of 8±0.12 ug mL−1 (Figure 4.2D). A live-dead cell assay further confirmed the neutralization activity.

RBC-NDs were further examined for protection against wSP-induced cytotoxicity on HUVECs. In the study, 1.22 v/v % wSP caused 70 % cell death (EC70), and 2 v/v % wSP caused complete cell death (EC100) (Figure 4.2G). In a preincubation regimen of neutralization, we mixed various concentrations of RBC-NDs with wSP (1.22 v/v %, EC70) and added the mixtures to the HUVECs. Figure 4.2H shows that cell viability was 50 % and 100 % when the RBC-ND concentrations were 0.76 μg mL^{-1} (IC50) and 4 μg mL^{-1} (IC100), respectively. In a competitive regimen, where RBC-NDs were first mixed with HUVECs followed by the addition of wSP (1.22 v/v %), the IC50 and IC100 values increased to 2.59 μg mL^{-1} and 16 μg mL^{-1}, respectively (Figure 4.2H). A live-dead cell assay further confirmed the observed neutralization efficacy of RBC-NDs

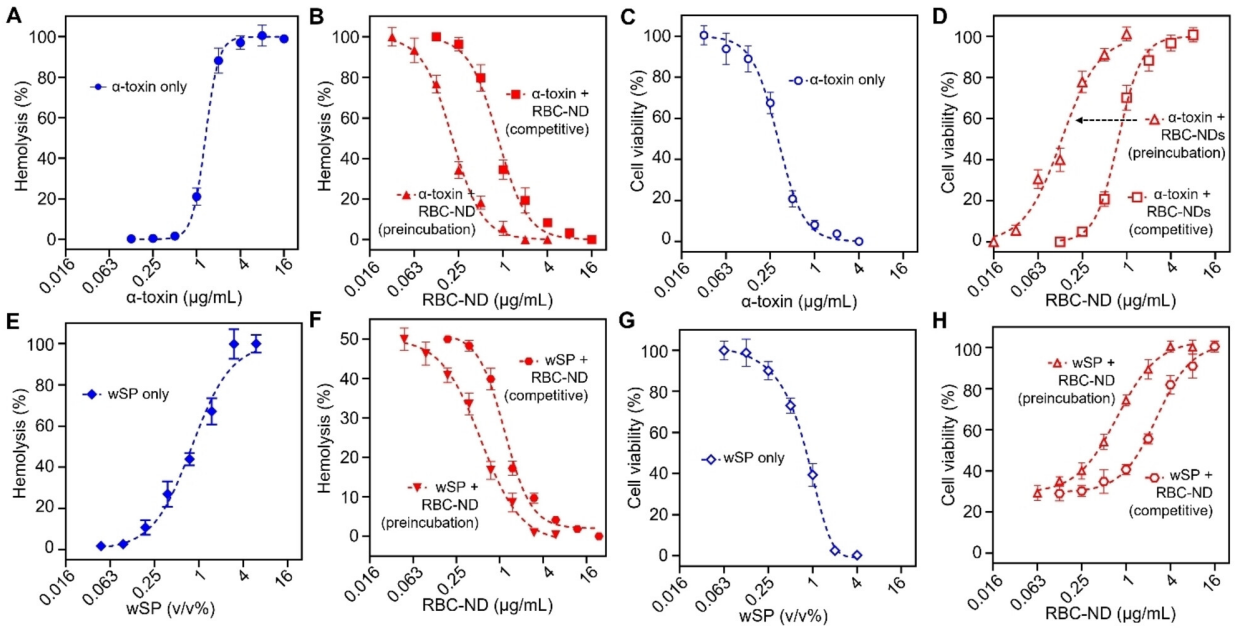

Figure 4.2 RBC-NDs neutralizing hemolysis and cytotoxicity of α-toxin and wSP.

A), E) Quantification of hemolysis after incubation of RBCs with (A) α-toxin or (E) wSP at various concentrations. B), F) Quantification of hemolysis in preincubation and competitive regimens. For preincubation regimen, different concentrations of RBC-NDs were premixed with (B) α-toxin (8 μg mL−1, HD100) or (F) wSP (0.8 v/v %, HD50) followed by incubating with RBCs. For competitive regimen, different concentrations of RBC-NDs were premixed with RBCs followed by incubating with (B) α-toxin (8 μg mL−1, HD100) or (F) wSP (0.8 v/v %, HD50). C), G) Viability of HUVECs treated with different concentrations of (C) α-toxin or (G) wSP. D), H) Viability of HUVECs in preincubation and competitive regimens. For preincubation regimen, different concentrations of RBC-NDs were premixed with (D) α-toxin (4 μg mL^{-1}, EC100) or (H) wSP (1.22 v/v %, EC70) followed by incubating with HUVECs. For competitive regimen different concentrations of RBC-NDs were premixed with HUVECs followed by incubating with (D) α-toxin (4 μg mL^{-1}, EC100) or (H) wSP (1.22 v/v %, EC70). In all studies, n=6, and data are presented as mean±standard deviation.

4.1.4 Neutralization of α-toxin and wSP *in vivo*

After confirming RBC-ND neutralization against bacterial toxins in vitro, we assessed such capability in vivo using mouse models of α-toxin or wSP intoxication. When mice were injected with α-toxin through the tail vein, their survival decreased as the toxin dosage increased. An α-toxin dosage of 0.25 mg kg^{-1} concentration to test RBC-ND neutralization. In a therapeutic regimen, we first injected α-toxin (0.25 mg kg^{-1}) intravenously and 2 min later injected RBC-

NDs. As shown in Figure 4.3B, at 10, 20, and 30 mg kg^{-1} of the RBC-ND, the mouse survival rate was 40 %, 60 %, and 100 %, respectively. Such dose-dependent survival benefit reflects the neutralization efficacy of RBC-NDs against α-toxin intoxication. In a prevention regimen, RBC-NDs (10 mg kg^{-1}) were first injected into mice via the tail vein, followed by α-toxin (0.25 mg kg^{-1}) injection at various intervals. As shown in Figure 4.3C, only 40 % of mice challenged with α-toxin 5 min after RBC-NDs injection survived. When the interval decreased to 3 min, the survival increased to 80 %. At a 1-min interval, all mice survived. This interval-dependent survival benefit indicates strong protection of RBC-NDs against α-toxin lethality.

To evaluate RBC-ND neutralization against MRSA wSP in vivo, we first established the wSP lethality in mice. Injection of fresh tryptic soy broth (TSB) and 1.5 mL kg^{-1} wSP caused no death, but 2.0 mL kg^{-1} caused 50 % death (LD50, Figure 4.3D). Above this dosage (2.5 and 3 mL kg^{-1}), no mice survived. We used 2.0 mL kg^{-1} (LD50) of wSP for the following study. In a therapeutic regimen, mouse survival was 60 % and 80 % when the RBC-NDs were injected within 2 min at 5 mg kg^{-1} and 10 mg kg^{-1}, respectively (Figure 4.3E). All mice survived when the RBC-ND dosage increased to 20 mg kg^{-1}. In a prevention regimen, mice were first injected with 20 mg kg^{-1} RBC-NDs, followed by wSP (2.0 mL kg^{-1}) at various intervals. As shown in Figure 4.3F, mice challenged with wSP at 3 and 5 min after the nanodisc injection showed survival rates of 80 and 70 %, respectively. At a 1-min interval, all mice survived. Like mice challenged with purified α-toxin, the correlation between the injection interval and the survival rate indicates the protective effect of RBC-NDs against wSP intoxication.

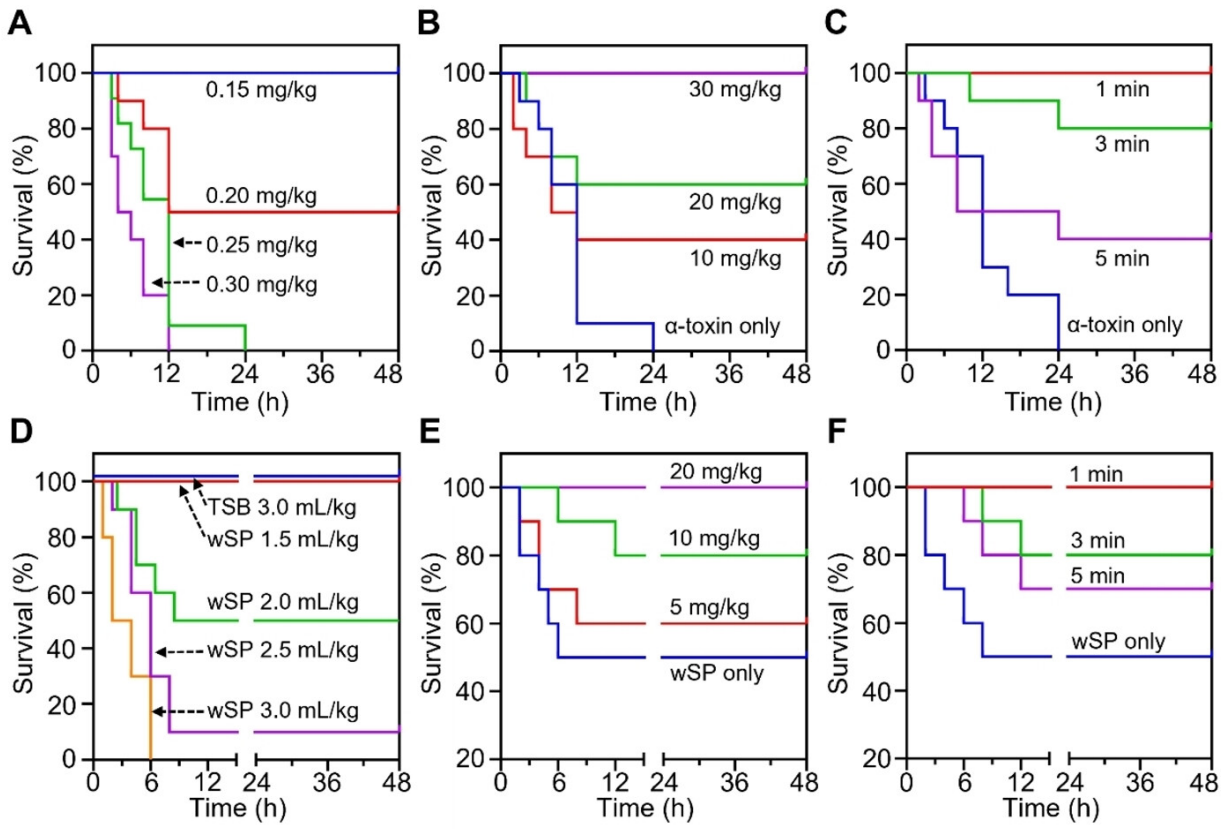

Figure 4.3 In vivo neutralization efficacy of RBC-NDs against α-toxin and wSP.

A) Survival rates of mice over 48 h following intravenous injection of α-toxin at various dosages (n=10). B) Survival rates of mice over 48 h in a therapeutic regimen, where mice were first injected with α-toxin (0.25 mg kg^{-1}) followed by injections of RBC-NDs within 2 min at various dosages. C) Survival rates of mice over 48 h in a prevention regimen, where mice were first injected with RBC-NDs (10 mg kg^{-1}) followed by injection of α-toxin (0.25 mg kg^{-1}) at various intervals, including 1, 3, and 5 min. D) Survival rates of mice over 48 h following intravenous injections of tryptic soy broth (TSB, 3.0 mL kg^{-1}) and wSP at various dosages. E) Survival rates of mice over 48 h in a therapeutic regimen, where mice were first injected with wSP (2.0 mL kg^{-1}) followed by injections of RBC-NDs at various dosages. F) Survival rates of mice over 48 h in a prevention regimen, where mice were first injected with RBC-NDs (20 mg kg^{-1}) followed by injections of wSP (2.0 mL kg^{-1}) at various intervals including 1, 3, and 5 min. In all studies, n=10. Statistical analysis was performed using Log-rank and Mantel-Cox test.

Finally, we evaluated the acute toxicity of RBC-NDs after in vivo administration in healthy mice. RBC-NDs were injected intravenously at 30 mg kg^{-1} (the highest concentration

used in this study) through the tail vein. We first examined the RBC, platelet, and white blood cell counts 24 h after the injection. Their values were comparable to the baseline levels (Figure 4.4A). Next, we tested the comprehensive serum chemistry panel, which was consistent with the baseline levels (Figure 4.4B). Therefore, the blood analysis indicated the short-term safety of RBC-NDs.

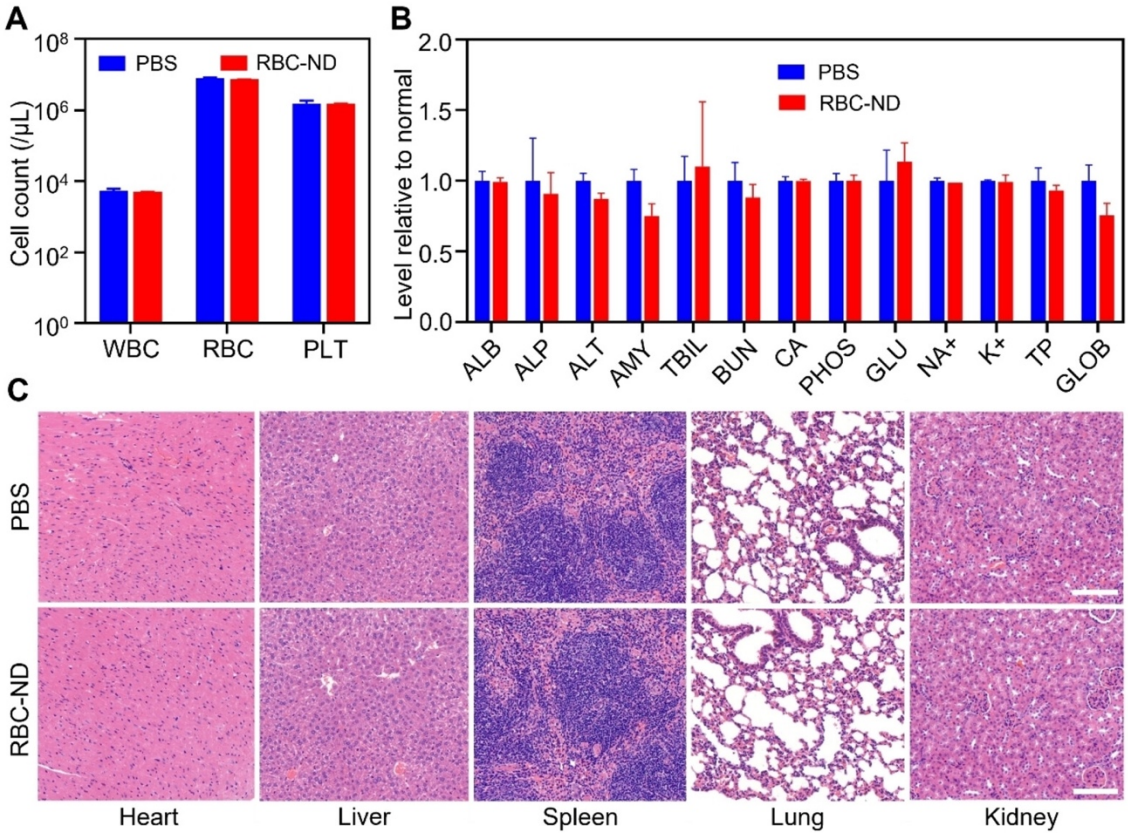

Figure 4.4 In vivo biosafety of RBC-NDs.

A) Counts of various blood cells 24 h after intravenous injection of PBS (control) or RBC-NDs (30 mg kg^{-1}). WBC, white blood cells; RBC, red blood cells; PLT, platelets. B) Blood biochemical panel analysis after 24 h administration of PBS or RBC-NDs. ALB, albumin; ALP, alkaline phosphatase; ALT, alanine transaminase; AMY, amylase; TBIL, total bilirubin; BUN, blood urea nitrogen; CA, calcium; PHOS, phosphorus; GLU, glucose; NA+, sodium; K+, potassium; TP, total protein; GLOP, globulin. C) H&E staining of histology sections from major organs (heart, liver, spleen, lung, and kidney) after 24 h administration of PBS or RBC-NDs. Scale bar=100 μm. Two groups of data were analyzed by using a student's t-test (two-tailed), and the comparison between PBS and RBC-NDs groups was not statistically significant ($P>0.05$). In all studies, n=6, and data are presented as mean+standard deviation.

We also collected the mouse heart, liver, spleen, lung, and kidney. The organ tissues were sectioned and stained with hematoxylin and eosin (H&E). The histological analysis showed similar appearances between the control and treated groups without apparent irregularities, indicating the absence of acute toxicity from the RBC-NDs (Figure 4.4C). Collectively, these data show good biosafety of the RBC-NDs.

4.1.5 Conclusion

In conclusion, we formulated cellular nanodiscs using natural RBC membrane and demonstrated their robust detoxification capability against bacterial toxins. The resulting RBC-NDs were significantly smaller than RBC membrane vesicles and were stable in biological solutions. We used purified α-toxin and wSP from MRAS bacteria to demonstrate that RBC-NDs effectively inhibited the hemolysis and cytotoxicity induced by these bacterial toxins. In mouse models of α-toxin and wSP intoxication, RBC-NDs conferred survival benefits in both therapeutic and prevention regimens. Moreover, RBC-NDs showed no apparent acute toxicity in vivo. Together, these results illustrate that the RBC-ND is an effective detoxification platform. Inspired by the formulation and associated biological functions of RBC-ND, similar design strategies may be applied to other types of cell membranes for novel cellular nanodiscs towards broad biomedical applications.

We previously developed RBC membrane-coated nanoparticles (RBC-NPs) and studied their capacity for neutralizing PFTs. [33-35] Note that the RBC-ND formulation reported here distinguishes greatly from the prior spherical RBC-NP formulation in terms of their size, shape, morphology, structure, and composition. We expect that the cellular nanodisc technology will enable additional opportunities of leveraging natural cell membranes for broad medical applications.

Chapter 4.1, in full, is a reprint of the material as it appears in *Angewandte Chemie International Edition*, 2023, Lei Sun, Dan Wang, Ilkoo Noh, Ronnie H. Fang, Weiwei Gao, and Liangfang Zhang; The dissertation author was a major contributor and co-author of this paper.

4.1.6 Reference

[1] T.H. Bayburt, S.G. Sligar, Membrane protein assembly into Nanodiscs, FEBS letters 584(9) (2010) 1721-1727.

[2] I.G. Denisov, S.G. Sligar, Nanodiscs for structural and functional studies of membrane proteins, Nature structural & molecular biology 23(6) (2016) 481-486.

[3] S. Zhang, Q. Ren, S.J. Novick, T.S. Strutzenberg, P.R. Griffin, H. Bao, One-step construction of circularized nanodiscs using SpyCatcher-SpyTag, Nature communications 12(1) (2021) 5451.

[4] C. Anada, K. Ikeda, A. Egawa, T. Fujiwara, H. Nakao, M. Nakano, Temperature- and composition-dependent conformational transitions of amphipathic peptide-phospholipid nanodiscs, Journal of Colloid and Interface Science 588 (2021) 522-530.

[5] T. Ravula, N.Z. Hardin, A. Ramamoorthy, Polymer nanodiscs: Advantages and limitations, Chemistry and Physics of Lipids 219 (2019) 45-49.

[6] J.A. Champion, S. Mitragotri, Role of target geometry in phagocytosis, Proceedings of the National Academy of Sciences of the United States of America 103(13) (2006) 4930-4934.

[7] Y.N. Zhang, W. Poon, A.J. Tavares, I.D. McGilvray, W.C.W. Chan, Nanoparticle-liver interactions: Cellular uptake and hepatobiliary elimination, Journal of Controlled Release 240 (2016) 332-348.

[8] S.L. Zhang, H.J. Gao, G. Bao, Physical Principles of Nanoparticle Cellular Endocytosis, Acs Nano 9(9) (2015) 8655-8671.

[9] R. Kuai, P.B. Singh, X.Q. Sun, C. Xu, A.H. Najafabadi, L. Scheetz, W.M. Yuan, Y. Xu, H. Hong, D.B. Keskin, C.J. Wu, R. Jain, A. Schwendeman, J.J. Moon, Robust Anti-Tumor T Cell Response with Efficient Intratumoral Infiltration by Nanodisc Cancer Immunotherapy, Advanced Therapeutics 3(9) (2020).

[10] I. Noh, Z.Y. Guo, J.R. Zhou, W.W. Gao, R.H. Fang, L.F. Zhang, Cellular Nanodiscs Made from Bacterial Outer Membrane as a Platform for Antibacterial Vaccination, Acs Nano 17(2) (2023) 1120-1127.

[11] J. Hwang, Y. Jung, S. Moon, S. Yu, H. Oh, S. Kim, K.W. Kim, J.H. Yoon, J. Chun, S.J. Kim, W.J. Chung, D.H. Kweon, Nanodisc-Mediated Conversion of Virustatic Antiviral Antibody to Disrupt Virus Envelope in Infected Cells, Small Methods 6(4) (2022).

[12] A.H. Najafabadi, J. Zhang, M.E. Aikins, Z.I.N. Abadi, F. Liao, Y. Qin, E.B. Okeke, L.M. Scheetz, J. Nam, Y. Xu, D. Adams, P. Lester, T. Hetrick, A. Schwendeman, M.S. Wicha, A.E. Chang, Q. Li, J.J. Moon, Cancer Immunotherapy via Targeting Cancer Stem Cells Using Vaccine Nanodiscs, Nano Letters 20(10) (2020) 7783-7792.

[13] H. Wang, X.Y. Wang, C. Xie, M.F. Zhang, H.T. Ruan, S.L. Wang, K. Jiang, F. Wang, C.Y. Zhan, W.Y. Lu, H. Wang, Nanodisk-based glioma-targeted drug delivery enabled by a stable glycopeptide, Journal of Controlled Release 284 (2018) 26-38.

[14] I.G. Denisov, Y.V. Grinkova, A.A. Lazarides, S.G. Sligar, Directed self-assembly of monodisperse phospholipid bilayer nanodiscs with controlled size, Journal of the American Chemical Society 126(11) (2004) 3477-3487.

[15] R. Kuai, X.Q. Sun, W.M. Yuan, Y. Xu, A. Schwendeman, J.J. Moon, Subcutaneous Nanodisc Vaccination with Neoantigens for Combination Cancer Immunotherapy, Bioconjugate Chemistry 29(3) (2018) 771-775.

[16] R. Kuai, L.J. Ochyl, K.S. Bahjat, A. Schwendeman, J.J. Moon, Designer vaccine nanodiscs for personalized cancer immunotherapy, Nature Materials 16(4) (2017) 489.

[17] H. Chu-Han, Z. Ze-Yu, S. Yi-Fan, H. Qian, W. Peng, Research Progress of Nanodiscs in Biomedical Field, PROGRESS IN BIOCHEMISTRY AND BIOPHYSICS 47(12) (2020) 1250-1260.

[18] M.E. Aikins, Y. Qin, H.E. Dobson, A.H. Najafabadi, K. Lyu, Y. Xu, Y. Xin, A. Schwendeman, M.S. Wicha, A.E. Chang, Q. Li, J.J. Moon, Cancer stem cell antigen nanodisc cocktail elicits anti-tumor immune responses in melanoma, Journal of Controlled Release 351 (2022) 872-882.

[19] J. Bariwal, H.R. Ma, G.A. Altenberg, H.J. Liang, Nanodiscs: a versatile nanocarrier platform for cancer diagnosis and treatment, Chemical Society Reviews 51(5) (2022) 1702-1728.

[20] F. Hagn, M.L. Nasr, G. Wagner, Assembly of phospholipid nanodiscs of controlled size for structural studies of membrane proteins by NMR, Nature Protocols 13(1) (2018) 79-98.

[21] M.J. Li, W.M. Atkins, W.D. McClary, Preparation of Lipid Nanodiscs with Lipid Mixtures, Current protocols in protein science 98(1) (2019) e100.

[22] M.A. McLean, M.C. Gregory, S.G. Sligar, Nanodiscs: A Controlled Bilayer Surface for the Study of Membrane Proteins, in: K.A. Dill (Ed.), Annual Review of Biophysics, Vol 472018, pp. 107-124.

[23] H.C. Huff, D. Maroutsos, A. Das, Lipid composition and macromolecular crowding effects on CYP2J2-mediated drug metabolism in nanodiscs, Protein Science 28(5) (2019) 928-940.

[24] Y. You, Y. Tian, Z.G. Yang, J.F. Shi, K.J. Kwak, Y.H. Tong, A.P. Estania, J.H. Cao, W.H. Hsu, Y.T. Liu, C.L. Chiang, B.R. Schrank, K. Huntoon, D.Y. Lee, Z.W. Li, Y.R. Zhao, H. Zhang, T.D. Gallup, J. Ha, S.Y. Dong, X.F. Li, Y.F. Wang, W.J. Lu, E. Bahrani, L.J. Lee, L.S. Teng, W. Jiang, F. Lan, B.Y.S. Kim, A.S. Lee, Intradermally delivered mRNA-encapsulating extracellular

vesicles for collagen-replacement therapy, Nature Biomedical Engineering 7(7) (2023) 887-+.

[25] R.H. Fang, A.V. Kroll, W.W. Gao, L.F. Zhang, Cell Membrane Coating Nanotechnology, Advanced Materials 30(23) (2018).

[26] S.Y. Wang, D. Wang, Y.O. Duan, Z.D. Zhou, W.W. Gao, L.F. Zhang, Cellular Nanosponges for Biological Neutralization, Advanced Materials 34(13) (2022).

[27] B.J. Berube, J.B. Wardenburg, Staphylococcus aureus α-Toxin: Nearly a Century of Intrigue, Toxins 5(6) (2013) 1140-1166.

[28] K. Tam, V.J. Torres, Staphylococcus aureus Secreted Toxins and Extracellular Enzymes, Microbiology Spectrum 7(2) (2019).

[29] X.L. Wei, J. Gao, F. Wang, M. Ying, P. Angsantikul, A.V. Kroll, J.R. Zhou, W.W. Gao, W.Y. Lu, R.H. Fang, L.F. Zhang, In Situ Capture of Bacterial Toxins for Antivirulence Vaccination, Advanced Materials 29(33) (2017).

[30] M. Esmaili, C.J. Brown, R. Shaykhutdinov, C. Acevedo-Morantes, Y.L. Wang, H. Wille, R.D. Gandour, S.R. Turner, M. Overduin, Homogeneous nanodiscs of native membranes formed by stilbene-maleic-acid copolymers, Nanoscale 12(32) (2020) 16705-16709.

[31] C.M.J. Hu, L. Zhang, S. Aryal, C. Cheung, R.H. Fang, L.F. Zhang, Erythrocyte membrane-camouflaged polymeric nanoparticles as a biomimetic delivery platform, Proceedings of the National Academy of Sciences of the United States of America 108(27) (2011) 10980-10985.

[32] S.E.A. Gratton, P.D. PohhauS, J. Lee, I. Guo, M.J. Cho, J.M. DeSimone, Nanofabricated particles for engineered drug therapies:: A preliminary Biodistribution study of PRINT ™ nanoparticles, Journal of Controlled Release 121(1-2) (2007) 10-18.

[33] C.M.J. Hu, R.H. Fang, J. Copp, B.T. Luk, L.F. Zhang, A biomimetic nanosponge that absorbs pore-forming toxins, Nature Nanotechnology 8(5) (2013) 336-340.

[34] Y.J. Chen, M.C. Chen, Y. Zhang, J.H. Lee, T. Escajadillo, H. Gong, R.H. Fang, W.W. Gao, V. Nizet, L.F. Zhang, Broad-Spectrum Neutralization of Pore-Forming Toxins with Human Erythrocyte Membrane-Coated Nanosponges, Advanced Healthcare Materials 7(13) (2018).

[35] Y.J. Chen, Y. Zhang, M.C. Chen, J. Zhuang, R.H. Fang, W.W. Gao, L.F. Zhang, Biomimetic Nanosponges Suppress In Vivo Lethality Induced by the Whole Secreted Proteins of Pathogenic Bacteria, Small 15(6) (2019).

4.2 Neuronal membrane nanodiscs for broad-spectrum neurotoxin detoxification

4.1.1 Introduction

Nanodiscs, characterized by their disc-shaped structure consisting of phospholipids surrounded by a stabilizing belt, have become invaluable tools in various fields, from membrane protein research to drug delivery. [1-4] The recent advancement of cell membrane nanodiscs (denoted 'cellular-ND') has opened new possibilities in nanomedicine. [5-7] These biomimetic nanoconstructs inherit the advantageous traits of traditional synthetic nanodiscs, such as their diminutive size, remarkable stability, and efficient tissue penetration. However, what sets cellular-NDs apart is their unique composition derived from natural cell membranes, allowing them to interact with biological systems and execute cellular functions in innovative ways.

For instance, cellular-NDs made from the outer membrane of Gram-negative bacteria inherit the multi-antigenic nature and inherent immunogenicity of their source membrane, making them ideal candidates for antibacterial vaccination. [5] Due to their small size, these nanodiscs exhibit enhanced localization to draining lymph nodes following subcutaneous administration compared to traditional outer membrane vesicles, ultimately extending the survival of vaccinated subjects upon challenge with live bacteria. Similarly, those derived from cancer cell membranes, when combined with a lipid adjuvant, are rapidly engulfed by antigen-presenting cells, eliciting robust anti-tumor immune responses. [7]

Expanding upon these initial developments, cellular-NDs have been harnessed for biological neutralization. Leveraging a top-down fabrication approach using cell membranes enables cellular-NDs to function as host cell decoys, entrapping harmful molecules based on membrane functionality without the need to identify specific targets. Their small size may enhance collision rates with toxin targets, thereby augmenting bioneutralization efficacy. Building upon these principles, researchers have engineered cellular-NDs utilizing human red blood cell (RBC) membranes, effectively neutralizing pore-forming toxins such as α-toxin and secreted proteins

from methicillin-resistant *Staphylococcus aureus* (MRSA). [6] Additionally, platelet membrane-derived nanodiscs serve as decoys, neutralizing pathological anti-platelet antibodies and bacterial virulence factors in animal models. [8]

Drawing on this background, in this work, we undertake an effort to expand the application of cellular-NDs in biological neutralization [9]. One promising avenue is their potential use in neutralizing neurotoxins, a class of compounds drawing considerable attention due to their unparallel potency. Neurotoxins like tetrodotoxin (TTX), saxitoxin (SAX), and botulinum toxin (BoNT) are notorious for their lethal effects, raising concerns about their potential as biological weapons capable of causing widespread devastation. [10-13] Conventional antidotes, including monoclonal antibodies and small-molecule inhibitors, monoclonal antibodies, and polymer affinity ligands, typically target the specific molecular structures of individual toxins. [14-18] As a result, enormous structural diversity exhibited by neurotoxins present significant challenges in antidote development, particularly in achieving broad-spectrum efficacy. [19-21] In certain cases such as BoNTs, their cell surface receptors are yet fully discovered. For some identified receptors, the molecular details the govern the recognition remain undertermined. [22]

Regardless of the structural and functional diversity, neurotoxins rely on cell membrane binding for bioactivity. For example, TTX and SAX bind selectively with voltage-dependent ion channels, plugging their entrance to permeate ion influx. [23, 24] Using a different mechanism, BoNT recognizes a wide range of cell surface receptors to initiate endocytosis and subsequently block pre-synaptic release of acetylcholine, the neurotransmitter at the neuromuscular junction. [22] Leveraging this shared property among neurotoxins, we propose the utilization of neuron membrane-derived nanodiscs for broad-spectrum neurotoxin neutralization. To achieve this goal, in this work, we engineer neuron-NDs using a human neuronal membrane through a facile self-

assembly process. After thorough characterization of the neuron-ND, we assess their efficacy in neutralizing TTX and BoNT, two model toxins representing distinct working mechanisms. Using comprehensive cell function assays, we demonstrate that neuron-NDs neutralize TTX, preventing TTX-induced ion channel blockage. We also show that neuron-NDs neutralize BoNT, reversing BoNT-induced inhibition of synaptic vesicle recycle. In animal models of intoxication, Neuron-NDs neutralize both toxins, offering significant survival benefits in toxin-intoxicated animals. These findings underscore the potential of neuron-NDs for broad-spectrum neurotoxin neutralization and their importance in combating neurotoxin-related threats.

4.1.2 preparation and characterization of Neuron-ND

We derived neuron membrane from human SH-SY5Y cells and made neuron membrane-derived vesicles (denoted 'Neuron-V') using sonication. Subsequently, we combined these vesicles with styrene-maleic acid (SMA) copolymer, resulting in the spontaneous formation of Neuron-ND. [5] During this process, the hydrodynamic diameter of the sample decreased from 80.5 ± 12.1 nm to 26.3 ± 2.5 nm (Figure 4.5B). The zeta potential values remained consistent, shifting from -24.5 ± 1.3 mV before the addition of SMA to -25.1 ± 2.3 mV afterward. Examination under a transmission electron microscope revealed a disc-shaped nanostructure with uniform size distribution in the final sample (Figure 4.5C). Furthermore, the sample demonstrated stability in both water and 1X phosphate-buffered saline (PBS) for a period of one week (Figure 4.5D). These findings align with previously documented formulations of cell membrane-nanodiscs, affirming the successful synthesis of Neuron-ND. [5-8]

Following the fabrication of Neuron-NDs, we labeled them with a fluorescent dye and administered them to mice via the tail vein injection. To evaluate the pharmacokinetic profile of Neuron-NDs, we monitored the fluorescence intensity of mouse blood samples at different time

points post-injection. Figure 4.5E illustrates a rapid decline in signal within the first hour, followed by a slower rate of decrease thereafter. Employing a two-compartment model, we calculated an elimination half-life of 19.7 hours (Figure 4.5E, inset). For the assessment of Neuron-ND biodistribution, we measured fluorescent intensity in the heart, liver, spleen, lung, kidney, and blood at 24, 48, and 72 h post-injection (Figure 4.5F). Upon normalization per gram of tissue, Neuron-NDs exhibited predominant accumulation in the liver and spleen, the primary organs of the reticuloendothelial system (RES). Analyzing on an organ-specific basis revealed liver and spleen as the major sites of Neuron-ND distribution. Notably, substantial fluorescence persisted in the blood across all time points. The decrease in blood fluorescence corresponded with an increase in liver signal, indicating the role of the reticuloendothelial system (RES) in Neuron-ND clearance. [25]

Following Neuron-ND formulation, we then investigated its ability to neutralize TTX using a cell osmotic swelling assay. [26] In this study, neuro-2a cells were exposed to veratridine (VTD) and ouabain (O). VTD facilitates Na^+ influx by activating the voltage-gated sodium channel (VGSC), while O prevents Na^+ efflux by inhibiting Na^+/K^+-ATPase. [27, 28] Consequently, intracellular Na^+ accumulates, causing cellular swelling and rounding. TTX is known to block VGSC, counteracting the effects of VTD and O, thus helping cells maintain their

elongated shape. Consequently, TTX neutralization is evidenced by a more rounded cell shape.

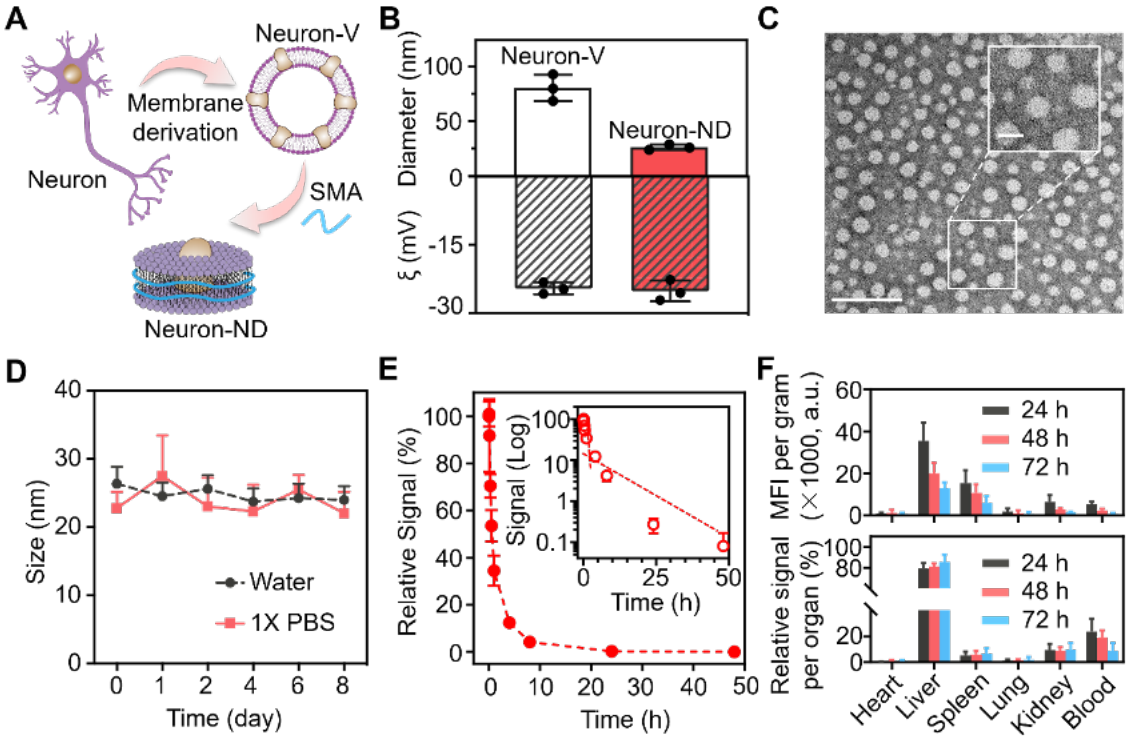

Figure 4.5 Preparation of characterization of Neuron-ND.

(A) Schematic preparation of neuron membrane-derived nanodiscs (denoted 'Neuron-ND'). We derived neural cell membranes (Neuron-V) from human neuronal cells. Neuron-V was then mixed with styrene-maleic acid (SMA) copolymer to form Neuron-ND, which showed a discoidal shape with natural membrane lipids and proteins, surrounded by SMA copolymer. (B) Size (diameter, nm) and zeta potential (mV) of neuron membrane vesicles (Neuron-V) and Neuron-ND, measured by dynamic light scattering (DLS). (C) Transmission electron microscopy (TEM) image of Neuron-ND (scale bar: 100 nm). Inset: a zoom-in view of Neuron-ND (scale bar: 20 nm). (D) DLS measurement of Neuron-ND size in 1X PBS at 4°C for 8 days. (E) Pharmacokinetic profile of Neuron-ND in mice. After intravenous injection of Alexa Fluor® 647 labeled Neuron-ND through the tail vein. Mouse blood samples were collected, and their fluorescence intensity was measured at different time points. Inset: semi log plot of fluorescence signal at different time points. (F) Biodistribution profile of Neuron-ND was measured by intravenously injecting Alexa Fluor® 647 labeled Neuron-ND into mice. At 24, 48, and 72 h time points, the organs from a randomly grouped subset of mice were collected, homogenized, and measured for fluorescence. In all datasets, n=3 independent experiments using the same batch of neuron membranes. In (E) and (F), Neuron-ND dosage was 10 mg/kg (membrane protein). Data (B) and (E) are presented as mean ± s.d. Data (D) and (F) are presented as mean + s.d.

4.1.3 Neutralizaiton of TTX and BoNT in vitro

As shown in **Figure 4.6A**, control cells added with PBS displayed a typical ellipsoidal shape. However, exposure to VTD and O induced a rounder shape due to uncontrolled Na^+ influx. Conversely, the addition of TTX enabled the cells to maintain their usual ellipsoidal morphology, indicating TTX's counteraction of VTD/O-induced osmotic swelling. Upon mixing TTX with Neuron-ND and administering the mixture to the cells, the cells appeared round, suggesting TTX neutralization by Neuron-ND.

To quantitatively assess this neutralization effect, we measured the cell roundness factor on a scale from 1 to 0, where 1 indicates a circular shape and values less than 1 indicate elongation. As shown in Figure 4.6B, cells treated solely with synthetic lipid nanodisc (denoted 'LND') control exhibited elongated shapes due to the absence of TTX neutralization. However, upon Neuron-ND addition, the roundness factor increased with escalating Neuron-ND concentrations, plateauing at 0.5 mg/mL and above. The maximum roundness value closely matched that of cells treated with VTD and O only, implying complete TTX neutralization.

Furthermore, we evaluated TTX neutralization using a cell-based sodium flux fluorescence assay. [26, 29] In this assay, neuro-2a cells loaded with a Na+-sensitive dye allowed monitoring of fluorescence changes indicative of Na+ influx across the cell membrane (Figure 4.6C). Control cells exhibited stable fluorescence, indicating consistent Na+ influx. Upon VTD addition, fluorescence significantly increased, signifying induced Na+ influx. However, co-treatment with TTX and VTD resulted in fluorescence levels comparable to controls, indicating TTX counteraction of VTD. Upon mixing TTX with Neuron-ND and subsequent addition to the cells, the fluorescence signal increased upon VTD addition, suggesting recovery of Na+ influx due to TTX neutralization by Neuron-ND. Notably, this neutralization was confirmed by

observing LND-treated cells, which showed no increase in Na+ influx, indicating the absence of TTX neutralization. Quantification using the maximum fluorescence change (ΔFmax/F0) revealed a dose-dependent neutralization against TTX with increasing Neuron-ND concentrations (Figure 4.6D).

Additionally, we investigated the neutralization of TTX by Neuron-ND using a cytotoxicity assay. This assay relies on a similar mechanism to the cell swelling assay, where intracellular Na+ accumulation due to VTD and O leads to cytotoxicity, and TTX counteracts these effects, enhancing cell viability. Decreased cell viability thus reflects TTX neutralization. As depicted in Figure 4.6E, LND-treated cells exhibited the highest viability, indicating no TTX neutralization. Conversely, as Neuron-ND concentrations increased, cell viability decreased, indicating dose-dependent TTX neutralization. At 1 mg/mL of Neuron-ND, cell viability was comparable to that of cells treated with VTD and O but not TTX, suggesting complete TTX neutralization.

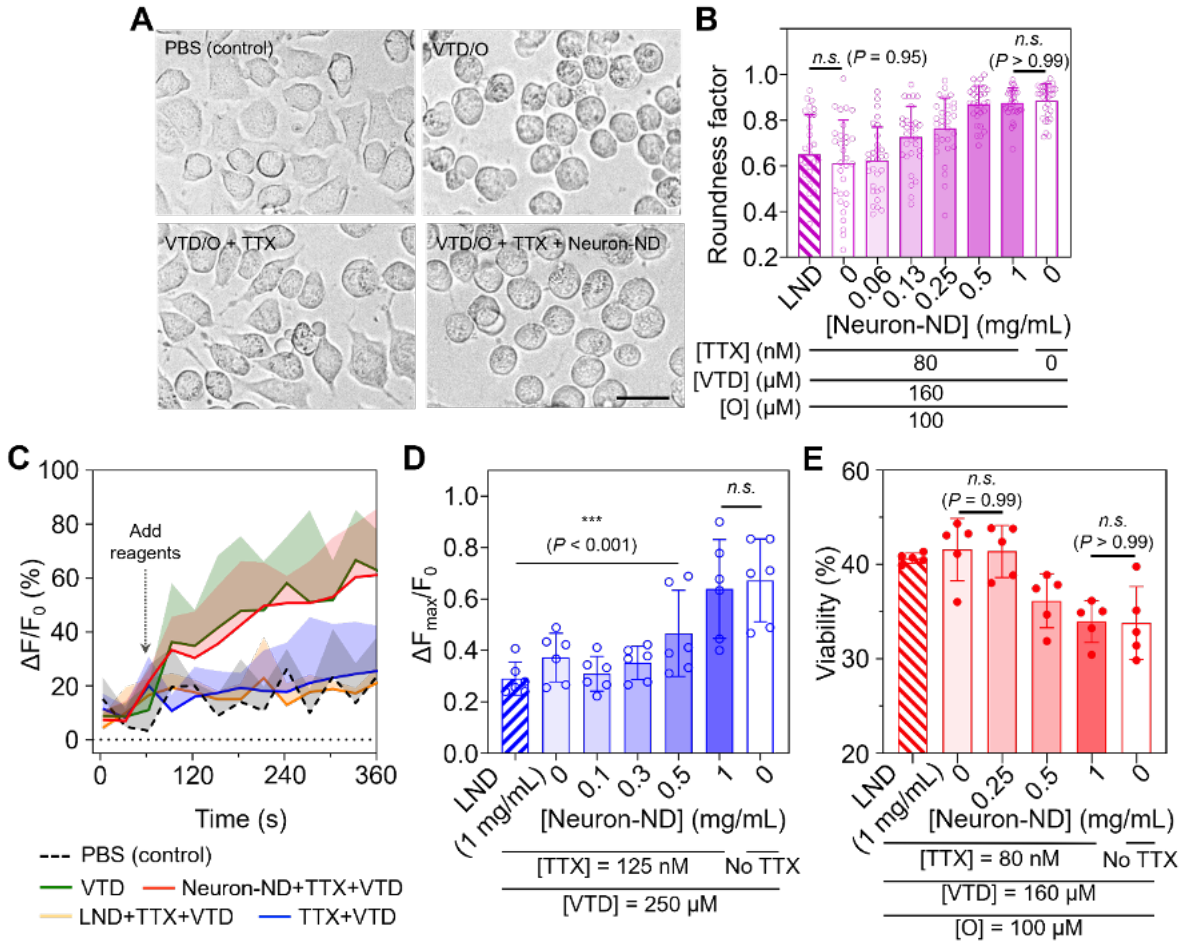

Figure 4.6 Neuron-ND neutralize TTX in vitro.

(A) Representative images of neuro-2a cells treated with different reagents indicated in the graph. Scale bar = 20 μm. (B) Quantification of cell roundness in a cell osmotic swelling assay (n = 30). (C) Na+-induced fluorescence changes at different measured from different study groups. Reagents indicated in the graph were added at 1 min. Neuron-ND or LND concentration was kept at 1 mg/mL (n = 3). (D) Maximum fluorescence change (ΔFmax/F0) of neuro-2a cells measured in a sodium flux fluorescence assay (n = 6). (E) The viability of neuro-2a cells treated with various groups indicated in the graph (n = 5). In (B) and (C), data are presented as mean + s.d. In (D) and (E), data are presented as mean ± s.d. The statistical analysis was performed using the student's t-test (n.s., not significant).

We next used BoNT as a different model toxin and tested the ability of Neuron-ND to neutralize it. Initially, we assessed the capacity of Neuron-ND in binding with BoNT. First, we held BoNT concentrations constant and varied Neuron-ND concentrations (**Figure 4.7A**).

Initially, the bound BoNT increased as Neuron-ND concentration increased, plateauing when Neuron-ND concentrations exceeded 50 μg/mL. Approximately 6 μg/mL Neuron-ND bound with 50% of the BoNT (EC50). In the subsequent experiment, we maintained Neuron-ND input constant and varied BoNT concentrations (Figure 4.7B). The study yielded a sigmoid binding profile of bound BoNT against the logarithm of BoNT input, with the EC50 value for Neuron-ND binding with BoNT calculated to be 370 pg/mL.

Following the binding study, we then tested BoNT neutralization by examining the ability of neuro-2a cells to recycle the synaptic vesicles as a function assay. [30, 31] In this assay, neuro-2a cells were loaded with a styryl FM dye, which stained synaptic vesicles green under a fluorescence microscope. Upon addition of a K^+ and Ca_2^+ solution to polarize the cells, rapid release of stained vesicles through exocytosis occurred, resulting in the loss of FM dye and a reduction in cell fluorescence intensity (Figure 4.7C). However, pre-incubation with BoNT before treatment with K^+ and Ca_2^+ led to cells retaining fluorescence, indicating BoNT inhibition of synaptic vesicle release. Conversely, treatment with a mixture of BoNT and Neuron-ND resulted in fluorescence diminishment after K^+ and $Ca2^+$ treatment, indicating restoration of synaptic vesicle release and BoNT neutralization by Neuron-ND. We also tested LND for neutralization, with cells treated with BoNT and LND retaining fluorescence, confirming that the observed inhibition was attributed to Neuron-ND.

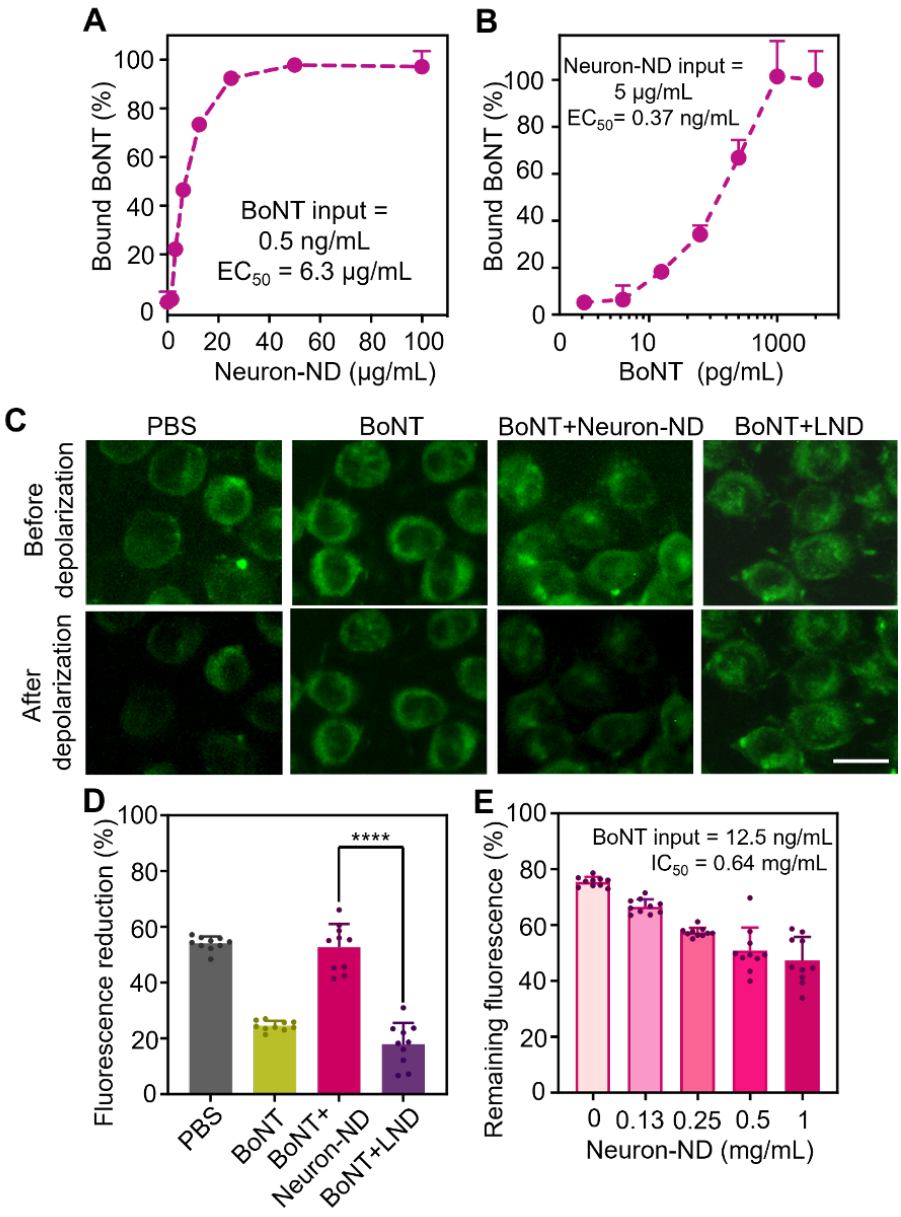

Figure 4.7 Neutralization of BoNT by Neuron-ND.

Relative binding of BoNT (0.5 ng/mL) to Neuron-NDs at various concentrations. (B) Relative binding of BoNT at various concentrations to Neuron-ND (5 µg/mL). (C) Representative fluorescence images of Neuro-2a cells before and after treatment with high K+ and Ca2+ to induce synaptic vesicle release. In this assay, neuro-2a cells were incubated with Neuron-ND or LND (1 mg/mL), followed by adding BoNT (12.5 ng/mL). The green color represents synaptic vesicles stained with FM1-43, a styryl fluorescent dye. Scale bar, 20 µm. (D) Remaining fluorescence of neuro-2a cells after depolarization. Cells were exposed to PBS (control), BoNT only, BoNT+Neuron-ND, and BoNT+LND. (E) Remaining fluorescence at various concentrations of Neuron-ND (0-1 mg/mL). In both (D) and (E), fluorescence from cells before depolarization with high K+ and Ca2+ was defined as 100%. Data presented as mean ±s.d. The statistical analysis was performed using the student's t-test (****$p<0.0001$)

Following the microscopic observation, we quantitatively measured cell fluorescence to compare BoNT neutralization in each group. Addition of K^+ and Ca_2^+ to the PBS group led to approximately 50% reduction in fluorescence intensity (Figure 4.7D). However, with the presence of BoNT, fluorescence reduction was only about 20%, indicating higher inhibition of synaptic vesicle release. Cells treated with Neuron-ND and then BoNT exhibited fluorescence reduction comparable to the PBS group, while cells treated with LND and then BoNT showed fluorescence reduction like the BoNT group. These findings corroborated the effective BoNT neutralization by Neuron-ND. Furthermore, as Neuron-ND concentration increased, remaining fluorescence (or inhibition of synaptic vesicle release) decreased accordingly, indicating dose-dependent BoNT neutralization by Neuron-ND (Figure 4.7E). The IC50 value, representing the Neuron-ND concentration inhibiting half of BoNT-induced synaptic inhibition, was determined to be 0.64 mg/mL.

4.1.4 Neutralization of TTX and BoNT in vivo

After demonstrating the ability of Neuron-ND to neutralize TTX and BoNT *in vitro*, we next assessed such neutralization ability in mouse models of TTX or BoNT intoxication. In a lethal TTX intoxication model, mice were injected with 9 μg/kg TTX subcutaneously. At this dosage, 60% of mice survived. In a treatment regimen, mice were injected with TTX (9 μg/kg) followed by injections of Neuron-ND (**Figure 4.8A**). Injection of Neuron-ND led to higher survival rates: at dosages of 5, 10, or 15 mg/kg, the survival rates were 70%, 80%, and 100%, respectively (Figure 4.8B). In comparison, PBS, or LND groups showed no survival benefit. We also used a sub-lethal TTX intoxication model. In this model, mice were injected with 8 μg/kg TTX subcutaneously. At this dosage, all mice survived, allowing us to evaluate TTX intoxication using a five-point scale based on their intoxication symptoms, including lethargy, mobility,

response to stimuli, and hunching. [32] Each symptom contributed to one score with a maximum score of four. As shown in Figure 4.8C, mice injected with 5, 10, and 15 mg/kg of Neuron-ND received an average score of 3.3, 2.8, and 1.5, respectively. In comparison, the LND and PBS groups showed scores of 3.3 and 3.7, which were significantly higher compared with the Neuron-ND group at the same concentrations.

We also used a preventative regimen to examine the efficacy, where mice were first injected with Neuron-ND intravenously, followed by injection of TTX (9 μg/kg) subcutaneously (Figure 4.8D). Injection of Neuron-ND resulted in higher survival rates: at dosages of 2, 5, or 10 mg/kg, the survival rates were 60%, 90%, and 100%, respectively (Figure 4.8E). Similar to previous study, the LND and PBS groups showed no survival benefits. In the sublethal model, mice were injected with 8 μg/kg TTX subcutaneously, and their intoxication symptoms were scored. Mice treated with 2, 5, and 10 mg/kg of Neuron-ND received an average score of 3.3, 2.3, and 0.7, respectively. (Figure 4.8F) In contrast, the score of the LND group was comparable to that of the PBS group. These results demonstrated effective TTX detoxification by Neuron-ND *in vivo*.

To evaluate Neuron-ND neutralization against BoNT in vivo, we determined the LD100 value of BoNT to be 10 ng/kg when the toxin was injected through the tail vain. Next, we injected BoNT of this dosage followed by injections of Neuron-ND, both intraveneously (Figure 4.8G). Injection of Neuron-ND resulted in higher survival rates: at dosages of 5, 10, or 15 mg/kg, the survival rates were 0%, 50%, and 100%, respectively (Figure 4.8H). In comparison, PBS or LND groups showed no survival benefit. In a sub-lethal BoNT intoxication model, mice were injected with 6 ng/kg BoNT. At this dosage, 100% of mice survived, enabling the evaluation of BoNT intoxication using a scoring system based on symptoms, including ruffled fur, wasp waist, motility, respiration, and body weight loss. [32] As shown in Figure 4.8I, mice treated with 5, 10,

and 15 mg/kg of Neuron-ND received an average score of 13.5, 14, and 4.7, respectively. In comparison, the LND or PBS-treated group received significantly higher scores.

We also used a preventative regimen to examine the efficacy of Neuron-ND in neutralizing BoNT. In the lethal BoNT intoxication model, mice were first intravenously injected with Neuron-ND, followed by injection of BoNT (10 ng/kg) intravenously (Figure 4.8J). Injection of Neuron-ND resulted in higher survival rates: at dosages of 2, 5, or 10 mg/kg, the survival rates were 33%, 83%, and 100%, respectively (Figure 4.8K). In comparison, all mice died in the PBS or LND groups. In the sublethal model, mice treated with 2, 5, and 10 mg/kg of Neuron-ND received an average score of 13.7, 11.2, and 6.2, respectively. In comparison, the score of the LND group scored an average value of 13.5, comparable to that of the PBS group. (Figure 4.8L). These results demonstrated effecctive BoNT neutralization by Neuron-ND *in vivo*.

Figure 4.8 In vivo neutralization of TTX and BoNT by Neuron-ND.

(A) Schematic of Neuron-ND for TTX neutralization in 4-week-old ICR mice. In the treatment regimen, mice received a subcutaneous injection of TTX, followed by the intravenous injection of Neuron-ND, LND, or PBS. The interval between TTX and nanodisc injection was 1 min. Mice survival was monitored for 24 h after the TTX injection. (B) Survival rate of mice over 24 h in a treatment regimen. TTX dosage was kept at 9 μg/kg. (C) Intoxication score of mice in a treatment regimen. The scores were recorded within 2 h after TTX injection. TTX dosage was maintained at 8 μg/kg. (D) Schematic of Neuron-ND for TTX neutralization in the preventative regimen. Mice were first injected intravenously with Neuron-ND, LND, or PBS. After 2 min, they were challenged by a subcutaneous injection of TTX. Mice survival was monitored for 24 h after the TTX injection. (E) Survival rate of mice over 24 h in a preventative regimen. TTX dosage was kept at 9 μg/kg. (F) Intoxication score of mice in a preventative regimen. TTX dosage was kept at 8 μg/kg. (G) Schematic depiction of Neuron-ND for BoNT neutralization. In the therapeutic regimen, mice received an intravenous injection of BoNT, followed by an intravenous administration of Neuron-ND. The interval between BoNT and nanodisc injection was 1 min. Mice survival and clinical scores were monitored for 7 d after the BoNT injection. (H) Survival rate of mice over 7 d in a therapeutic regimen. BoNT dosage was kept at 10 ng/kg. Mice treated with LND (15 mg/kg) or PBS served as controls. (I) Clinical scores of mice in a therapeutic regimen. BoNT dosage was maintained at 6 ng/kg. (J) Schematic of Neuron-ND for BoNT neutralization in the preventative regimen. Mice were first injected intravenously with Neuron-ND, followed by the intravenous injection of BoNT 2 min later. Mice survival and clinical scores were monitored for 7 d after the BoNT injection. (K) Survival rate of mice over 7 d in a preventative regimen. BoNT dosage was kept at 10 ng/kg. Mice treated with LND (10 mg/kg) or PBS were used as controls. (L) Clinical score of mice treated with Neuron-ND at different dosages in a preventative regimen. BoNT dosage was kept at 6 ng/kg. In (B) and (C), n = 10 per group. In other groups, n = 6 per group. *P $\leqslant$ 0.05, ****P $\leqslant$ 0.001, ****P $\leqslant$ 0.0001. Statistical analysis was performed with a Student’s t-test (two-tailed).

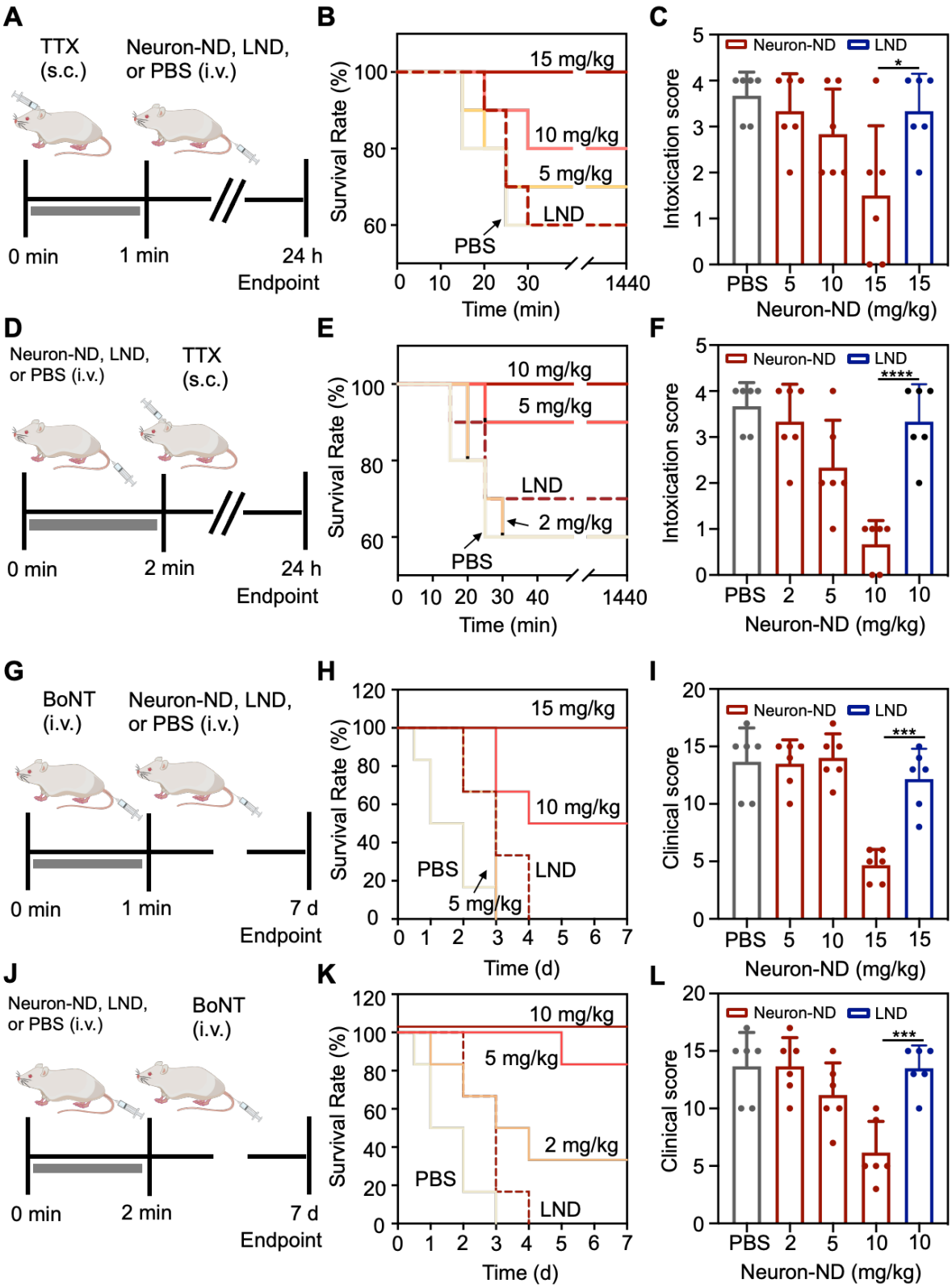
A
TTX
(s.c.)
Neuron-ND, LND,
or PBS (i.v.)
0 min
1 min
24 h
Endpoint
B
Survival Rate (%)
15 mg/kg
10 mg/kg
5 mg/kg
LND
PBS
Time (min)
C
Neuron-ND
LND
Intoxication score
Neuron-ND (mg/kg)
D
Neuron-ND, LND,
or PBS (i.v.)
TTX
(s.c.)
0 min
2 min
24 h
Endpoint
E
10 mg/kg
5 mg/kg
LND
2 mg/kg
PBS
Time (min)
F
****
G
BoNT
(i.v.)
Neuron-ND, LND,
or PBS (i.v.)
0 min
1 min
7 d
Endpoint
H
Time (d)
I
***
Clinical score
J
Neuron-ND, LND,
or PBS (i.v.)
BoNT
(i.v.)
0 min
2 min
7 d
Endpoint
K
L

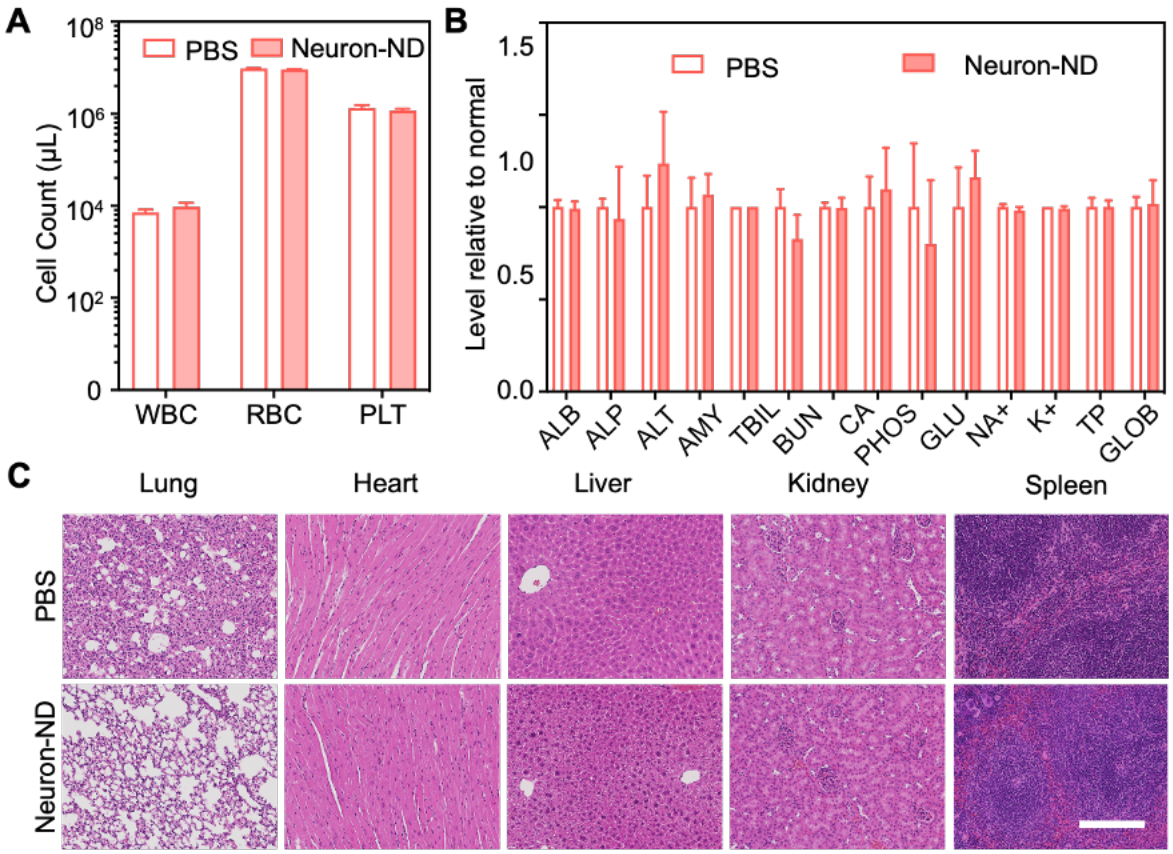

Figure 4.9 In vivo biosafety of Neuron-ND.

(A) Blood cell counts 7 days after intravenous injection of Neuron-ND (15 mg/kg) or PBS (n=3). WBC, white blood cells; RBC, red blood cells; PLT, platelets. (B) Blood biochemistry panel 7 days after administration of PBS or Neuron-ND (15 mg/kg) intravenously (n = 3). ALB, albumin; ALP, alkaline phosphatase; ALT, alanine transaminase; AMY, amylase; TBIL, total bilirubin; BUN, blood urea nitrogen; CA, calcium; PHOS, phosphorus; GLU, glucose; NA+, sodium; K+, potassium; TP, total protein; GLOP, globulin. (C) Hematoxylin-and-eosin (H&E) staining of histology sections from major organs (lung, heart, liver, kidney, and spleen) 7 days after PBS or Neuron-ND (15 mg/kg) administration. Scale bar = 200 μm. All data presented as mean ±s.d. In panels A and B, a statistical analysis was performed using the paired Student's t-test, with no statistically significant difference between the PBS and Neuron-ND groups ($P > 0.05$).

Lastly, we assessed the acute toxicity of Neuron-ND in healthy mice following in vivo administration via tail vein injection at a dosage of 15 mg/kg. After 7 d, both blood count and comprehensive metabolic panel analysis were conducted. Figure 4.9 A illustrates that the levels of RBC, white blood cells (WBC), and platelets (PLT) in mice injected with Neuron-ND were

comparable to those in the control group receiving PBS injections. Moreover, the comprehensive blood chemistry results depicted in Figure 4.9B aligned with baseline levels. Histopathological analysis of major organs, including the liver, spleen, heart, lung, and kidney, was performed as depicted in Figure 4.9 C. Tissue samples were collected, sectioned, and stained with hematoxylin and eosin (H&E) 7 days post-injection. Remarkably, no abnormalities were observed in the Neuron-ND treated group compared to the control group. These findings strongly suggest the biosafety of Neuron-ND at the tested dosage.

4.2.5 Methods

Neuron membrane derivation: SH-SY5Y cells, a human neuroblastoma cell line, were obtained from American Type Culture Collection (ATCC, CRL-2266) and cultured in the Dulbecco's modified Eagle's medium (DMEM, Corning) supplemented with 10% fetal bovine serum (FBS, Hyclone) and 1% penicillin-streptomycin (Gibco). The cells were maintained at 37°C with 5% CO_2 in a humidity-controlled incubator. The cells were cultured in T175 culture flasks to full confluency and detached with ethylenediaminetetraacetic acid (EDTA, Hyclone). Then, the cells were harvested by a rubber scraper (Fisher Scientific) and centrifuged at 700 ×g for 5 min. The collected cells were washed three times with 1X phosphate-buffered saline (PBS, Hyclone) with centrifugation at the same settings. After the centrifugation, the supernatant was discarded, and the pellet was resuspended in isolation buffer consisting of 30 mM Tris-HCl (pH = 7.5), 225 mM D-mannitol, 75 mM sucrose, 0.2 mM ethylene glycol-bis(β-aminoethyl ether)-(*N*, *N*, *N*', *N*'-tetraacetic acid) (EGTA), and 100 μL of protease-phosphatase inhibitor cocktail (all from Millipore-Sigma). Cells were then disrupted using a Kinematica Polytron PT 10/35 probe homogenizer (70% power and 20 passes). The homogenized solution was centrifuged at 20 k ×g for 25 min at 4°C. The pellet was discarded, and the supernatant was centrifuged again at

100 k ×g for 35 min at 4°C. The cell membrane was collected as the pellet and washed twice with 0.2 mM EDTA in water. Membrane protein content was quantified by using a bicinchoninic acid (BCA) protein assay (Pierce, Thermo Fisher Scientific). Approximately 1×10^8 SH-SY5Y cells yield 1 mg of membrane (protein weight). The membrane was suspended in 0.2 mM EDTA and stored at -80°C for subsequent studies.

Preparation of Neuron-ND: Neuron-ND was prepared by mixing the SH-SY5Y membrane with SMALP 200 (Cube Biotech), followed by sonicating the mixture (Fisherbrand 120 Sonic Dismembrator, 100 W for 30 s) in an ice water bath. After the sonication, the mixture was stirred overnight at 4°C. After that, the mixture was centrifuged at 150 k × g for 30 min. The pellet was discarded, and the supernatant was collected. The Neuron-NDs in the supernatant were concentrated with an Amicon filtration tube (Millipore, 10 kDa molecular weight cut-off or MWCO). The protein content of the Neuron-ND in the retentate was quantified using a BCA protein assay. For fluorescently labeled Neuron-ND, 100 µg Alexa Fluor™ 647-NHS (Ex/Em = 650/668, Invitrogen) dissolved in dimethyl sulfoxide (Sigma, DMSO) was mixed with 10 mg Neuron-ND in 0.1 M sodium bicarbonate buffer. After incubation at room temperature for 1 h, the mixture was washed three times using 10 kDa MWCO Amicon Ultra centrifugal filters. The dye-labeled Neuron-ND was stored at 4 °C for further use. To prepare lipid nanodiscs (LND), 1,2-dimyristoyl-sn-glycero-3-phosphocholine (DMPC, Sigma, 10 mg) was dissolved in 1 mL chloroform and methanol mixture (1 : 1). This solution was evaporated to form a dry lipid film below a vacuum aspirator, which was then added with 1 mL PBS and 50 mg SMALP 200. After sonication for 30 s in an ice water bath, the mixture was stirred overnight at 4 °C.

Physicochemical characterization of Neuron-ND: Neuron-ND size and zeta potential were measured with dynamic light scattering (DLS, Malvern ZEN 3600 Zetasizer, at 0.5 mg/mL). For

Neuron-ND morphology, samples were negatively stained with 1% uranyl acetate (Electron Microscopy Sciences) and visualized using a JEOL 1200 EX II transmission electron microscope (TEM). To evaluate the stability, Neuron-ND samples (1 mL, 1 mg/mL) were suspended in 1X PBS or water at 4 °C, and their sizes and polydispersity index (PDI) were measured at various time points (0, 1, 2, 4, 6, and 8 d) with DLS.

Animal care and injections: All animal studies were approved under the guidelines of the University of California San Diego (UCSD) Institutional Animal Care and Use Committee (IACUC). In all animal studies, 4-week-old ICR mice (Harlan Laboratories, male) were used. Mice were housed in an animal facility at UCSD under federal, state, local, and NIH guidelines for animal care. In the study, no inflammation or any abnormal appearance was observed at the sites of injection.

Pharmacokinetics, biodistribution of Neuron-ND: In the pharmacokinetics study, Alexa Fluor™ 647 labeled Neuron-NDs (15 mg/kg, protein weight) was injected through the tail vein (n = 3), and the blood samples were collected at predetermined time points (1, 3, 5, 15, and 30 min, and 1, 4, 8, 24, and 48 h) via submandibular puncture with heparin-coated microtubes (Millipore-Sigma). In the study, 20 μL of blood was mixed with 80 μL PBS in a 96-well plate for fluorescence measurement with a plate reader (BioTek Synergy Mx, Agilent). Pharmacokinetic parameters were calculated based on fitting with a two-compartment model. For the biodistribution study, Alexa Fluor™ 647 labeled Neuron-NDs (15 mg/kg, protein weight) were injected intravenously through the tail vein. At 24, 48, and 72 h after the injection, major organs, including the liver, kidney, spleen, lung, heart, and blood, were collected from the mice. The collected organs were then weighed and homogenized in 1X PBS for fluorescence measurement.

In vitro Neuro-2a cell viability assay: Neuro-2a cells were seeded at 4000 cells/well density one day before the experiment in a 384-well plate (Corning). The plate was maintained under the same conditions as described for cell maintenance. On the day of the experiment, a working solution of DMEM, comprising 200 μM of Ouabain, 320 μM of veratridine (VTD), 10 v/v% of fetal bovine serum (FBS, Thermo Fisher Scientific), and 1 v/v% of penicillin-streptomycin (PS, Thermo Fisher Scientific) was prepared. Serial dilutions of the working solution containing O at 12.5, 25, 50, 100, and 200 μM or VTD at 20, 40, 80, 160, and 320 μM were added to each well. After 24 h incubation, the cell viability was measured by a 3-(4, 5-dimethylthiazol-2-yl)-5-(3-carboxymethoxyphenyl)-2-(4-sulfophenyl)-2H-tetrazolium (MTS) assay (Promega). To study the impact of tetrodotoxin (TTX, R&D Systems) on cytotoxicity, the cells were treated with the diluted working solutions containing O (final concentration 100 μM), VTD (final concentration 160 μM), and TTX (final concentrations ranging from 0 to 320 nM). Cell viability was measured by following the same procedure as described above. To study how TTX neutralization by Neuron-ND affected the cytotoxicity, a mixture of 50 μL Neuron-ND and 4 μL TTX was prepared in DMEM. The concentrations of Neuron-ND in the mixture ranged from 0 to 10 mg/mL (protein concentration), and the TTX concentration in the mixture was kept at 0.8 μM. After 1 h incubation, Neuron-NDs were removed using Amicon Ultra-4 Centrifugal Filters (10 kDa MWCO, centrifuged at 6000 ×g for 10 min). Subsequently, 13 μL of the filtrate was mixed with 2 μL O-VTD stock solution (in DMSO), and 115 μL cell culture medium. Then, 25 μL mixture containing O (final concentration 100 μM) and VTD (final concentration 160 μM) was added to the cells. Cell viability was measured as described above. The neutralization effect of LND was assessed using the same procedure as with Neuron-ND. In all measurements, the viability measured from cells cultured without O, VTD, or TTX was used as 100%.

In vitro cell osmotic swelling assay: Neuro-2a cells were seeded in a 384-well plate at 2500 cells/well density. The plate was incubated under the same conditions as described above for cell maintenance. To induce cell swelling, a mixture of VTD (160 μM) and O (100 μM) was added to the cells. To study the neutralization against TTX, TTX (final concentration 80 nM) was incubated with LND (1 mg/mL) or Neuron-ND at various concentrations (0-1 mg/mL) for 30 min. Following incubation, the supernatant containing unbound TTX was obtained by removing Neuron-ND via centrifugation (6000 ×g for 10 min with Amicon Ultra-4 centrifugal filters, MWCO = 10 kDa). The unbound TTX mixed with VTD (final concentration 160 μM) and O (final concentration 100 μM) was incubated with Neuro-2a cells for 12 h. Following the incubation, the bright field images of the cells were taken with an EVOS inverted microscope (Thermo Fisher Scientific). The cell roundness was defined as $(4\pi \times \text{area})/(\text{perimeter})^2$. Roundness values approaching 0 indicate a more elongated cell shape, whereas values approaching 1 indicate a circular cell shape. In the study, 30 cells randomly chosen from these images were analyzed for each experimental group to assess the neutralization effects.

In vitro Neuro-2a cell sodium flux assay: Neuro-2a cells were seeded in a 384-well culture plate at a density of 2500 cells/well and cultured for 24 h before the study under the conditions described above. On the day of the study, 1 mL of the sodium flux dye loading solution (Brilliant Sodium Flex, ION biosciences) was prepared by following the manufacturer's instructions. The cell culture medium was replaced with 20 μL of the dye-loading solution, and cells were incubated at 37°C for 30 min. Serial dilutions of VTD were made using DMSO to concentrations of 0.4, 0.8, 1.6, and 3.1 μM. To study the effect of VTD on inducing sodium influx, 1 μL VTD solution was added into each well, resulting in final VTD concentrations of 62.5, 125, 250, and 500 μM. To study the effect of TTX on inhibiting VTD-induced sodium influx, TTX was serially

diluted in PBS to concentrations of 0.4, 0.8, 1.6, and 3.1 μM. Subsequently, 2 μL TTX solution was added to each well, resulting in final TTX concentrations of 31.3, 62.5, 125, and 250 nM. After incubation for 15 min, 1 μL VTD was added to achieve a final VTD concentration of 250 μM. The fluorescent intensity was recorded 60 sec before the addition of VTD. After adding VTD, the fluorescent intensity measurements were taken every 20 seconds for 300 seconds at room temperature. To study TTX neutralization with Neuron-ND, 1.3 mM TTX was mixed with 10 mg/mL Neuron-ND or LND control. After 1 h incubation, the nanodiscs were removed with Amicon Ultra-4 centrifugal filters (Millipore, 30 kDa MWCO) using centrifugation (6000 ×g for 10 min). Subsequently, 2 μL of the filtrate containing unbound TTX was added to the cells and incubated at room temperature for 15 min. Then, VTD was added into the well to a final concentration of 250 μM. We initiated the recording of the fluorescent intensity 60 sec before the addition of VTD. After adding VTD, the fluorescent intensity was measured every 20 sec for 300 sec at room temperature. For dose-dependent neutralization, 125 nM TTX was incubated with Neuron-ND of 0, 0.125, 0.25, 0.5, and 1 mg/mL (protein concentration). In the data plotting, ΔF_{max} represents the maximum increase in fluorescence intensity change relative to F_0, where F_0 is the mean baseline fluorescence intensity, and ΔF is the fluorescence intensity change at given time points relative to F_0.

In vivo neutralization of TTX by Neuron-ND: To evaluate the toxicity of TTX *in vivo*, subcutaneous injections of various dosages of TTX solutions (8-10 μg/kg) were administered to ICR mice (n = 10). Mouse survival was monitored for 24 h after the TTX injection. A TTX dosage that induced 40% of death in mice (LD40) was selected for the following studies. To evaluate the neutralization effect of Neuron-ND, mice were treated in both treatment and prevention regimens. In the treatment regimen, ICR mice (n=10) were subcutaneously injected

with TTX (9 μg/kg). After 1 min, they received intravenous injections of LND (15 mg/kg) or Neuron-ND at varying dosages (5-15 mg/kg, 100 μL injection volume). In the preventative efficacy study, mice first received an intravenous injection of LND (10 mg/kg) or Neuron-ND at varying dosages (2-10 mg/kg, 100 μL injection volume). After 2 min, mice were subcutaneously injected with TTX (9 μg/kg). In both regimens, the mouse survival was monitored for 24 h after TTX injection. To evaluate the neutralization effect in a sublethal model, the sublethal dosage of TTX (8 μg/kg) was injected subcutaneously into ICR mice (n=6). The degree of intoxication was scored on a five-point scale (0, normal; 4, maximal score). The intoxication score was based on the syndrome, including lethargy, mobility, response to stimuli, and hunching (Table 1). In the treatment regimen, ICR mice were first subcutaneously injected with TTX. LND (15 mg/kg) or Neuron-NDs at varying dosages (5-15 mg/kg, 100 μL injection volume) were administered intravenously 1 min after subcutaneous injection of sublethal dosage of TTX. In the prevention regimen, TTX was first injected subcutaneously. After 2 min, LND (10 mg/kg) or Neuron-NDs at varying dosages (2-10 mg/kg, 100 μL injection volume) were administered intravenously. In both regimens, the syndromes of mice were monitored for 2 h after TTX injection.

Quantification of botulinum toxin (BoNT) binding with Neutron-ND: To evaluate BoNT binding with Neuron-ND, 500 pg/mL BoNT type A1 from *Clostridium botulinum* (Metabologics) was mixed with 100 μL Neuron-ND or LND (0-100 μg/mL) in 1X PBS containing 1w/v% BSA. The mixtures were incubated at room temperature for 30 min under vortexing. The unbound BoNT concentration in the mixture or BoNT standard was quantified with an enzyme-linked immunosorbent assay (ELISA, R&D Systems).

BoNT neutralization by Neuron-ND in vitro: The neutralization was investigated by using a synaptic vesicle recycling assay. Specifically, Neuro-2a cells were seeded at 8000 cells/well

density in a 96-well plate and cultured for 24 h. On the day of the experiment, 0-25 ng/mL of BoNT were incubated with Neuro-2a cells for 3 h. The cells were washed twice with Hank's balanced salt solution (HBSS), followed by incubation with 10 μM *N*-(3-triethylammoniumpropyl)-4-(4-(dibutylamino) styryl) pyridinium dibromide (FM1-43, Ex/Em = 480/520 nm, Thermo Fisher Scientific) in HBSS containing 2 mM $CaCl_2$ and 56 mM KCl. After 10 min of incubation, the cells were washed twice with Ca^{2+}/K^+-free HBSS containing 0.5 mM EGTA. The cells were kept in 100 μL Ca^{2+}/K^+-free HBSS and depolarized by adding 2 μL Ca^{2+}/K^+ solution (with the final concentration of 2 mM Ca^{2+} and 56 mM K^+). Cells were imaged with an inverted fluorescence microscope (EVOS, Thermo Fisher Scientific) from 2 min before polarization to 8 min after polarization. The images were analyzed with ImageJ to quantify the fluorescence. The intensity from cells without the treatment and with FM1-43 but without depolarization was normalized as 0 and 100 % intensity. To evaluate BoNT neutralization by Neuron-ND, the Neuro-2a cells were added with LND (1 mg/mL, control) or Neuron-ND at various concentrations (0-1 mg/mL) in 100 μL medium, followed by adding BoNT (12.5 ng/mL final concentration). After incubation for 3h, the media were replaced, and the same procedure was used to examine the effect of BoNT.

Neutralization of BoNT by Neuron-ND in vivo: The BoNT stock was first diluted in gelatin-phosphate buffer (30 mM, pH 6.2, 0.2 w/v% gelatin) and subsequently injected intravenously through the tail vein into ICR mice at various dosages (0-2 ng/kg, $n = 6$). Mouse survival was monitored daily for 7 d. To evaluate the neutralization of Neuron-ND, two dosing regimens were used to examine the therapeutic efficacy. In a treatment regimen, BoNT at the LD100 dose (10 ng/kg) was injected intravenously into mice. After 1 min, LND (15 mg/kg) or Neuron-ND at varying dosages (5-15 mg/kg) was injected intravenously ($n = 6$). In a prevention regimen, mice

were first injected with LND (10 mg/kg) or Neuron-ND at varying dosages (2-10 mg/kg) through the tail vein (n = 6). Two minutes after the injection, mice were injected with BoNT at an LD100 dose (10 ng/kg). Mice were monitored daily for 7 d. The humane endpoint was set as weight loss exceeding 30% or the emergence of agonal breathing. To evaluate BoNT neutralization in a sublethal model, the sublethal dosage of BoNT (6 ng/kg) was injected intravenously into ICR mice (n=6). Clinical scores were recorded according to previously reported criteria, where mice were scored based on ruffled fur, wasp waist, motility, respiration, and body weight loss. In the treatment regimen, mice were first subcutaneously injected with BoNT. LND (15 mg/kg) or Neuron-NDs at varying dosages (5-15 mg/kg, 100 μL injection volume) were administered intravenously 1 min after injection of sublethal dosage of BoNT. In the prevention regimen, BoNT was first injected intravenously. After 2 min, LND (10 mg/kg) or Neuron-NDs at varying dosages (2-10 mg/kg, 100 μL injection volume) were administered intravenously. In both regimens, the syndromes of mice were monitored for 7 d.

In vivo biosafety study: For the biosafety evaluation, Neuron-ND (15 mg/kg, n = 3) was injected intravenously into the mice through the tail vein. The control group received an injection of the same volume of PBS. At 7 d postinjection, approximately 310 μL of the blood was collected via the submandibular puncture. 250 μL blood was coagulated in an Eppendorf tube and then centrifuged at 3 k ×g for 5 min to collect the serum for comprehensive metabolic panel analysis. Additionally, 60 μL blood was collected into an EDTA-coated microtube for the complete blood count without further processing. All blood samples were tested at the UCSD Animal Care Program Diagnostic Services Laboratory. To evaluate the impact of Neuron-ND on tissue and organs, mice were euthanized and major organs including the liver, heart, spleen, lung, and kidney, were harvested. The collected organs were fixed with 10% formalin and sectioned for

hematoxylin and eosin (H&E) staining. Histological slide images were taken with a Micromaster II Microscope (Fisher Scientific).

4.2.6 Conclusion

In summary, we fabricated neuron-NDs using natural neuronal membrane and demonstrated their broad-spectrum detoxification capabilities against neurotoxins. Comprising membrane building blocks stabilized by synthetic polymer chains, these neuron-NDs were significantly smaller than neuronal membrane vesicles, exhibited a disc shape, and showed high stability in biological buffers. Using comprehensive cellular assays, we validated their ability to mitigate TTX-induced ion channel inhibition and reverse BoNT-induced suppression of synaptic vesicle recycling. Crucially, in mouse models, Neuron-ND administration led to significant improvements in survival rates following TTX and BoNT intoxication, underscoring their therapeutic potential. Importantly, even in healthy mice, Neuron-ND injections elicited no discernible acute toxicity. Collectively, these findings underscore the Neuron-ND as a versatile and potent platform for neurotoxin detoxification, offering broad-spectrum protection against these harmful agents.

Chapter 4.2, in full, has been submitted for publication of the material. The dissertation author was the primary author of this paper.

4.1.6 References

[1] D.P. Staus, H.L. Hu, M.J. Robertson, A.L.W. Kleinhenz, L.M. Wingler, W.D. Capel, N.R. Latorraca, R.J. Lefkowitz, G. Skiniotis, Structure of the M2 muscarinic receptor-β-arrestin complex in a lipid nanodisc, Nature 579(7798) (2020) 297-302.

[2] J. Bariwal, H.R. Ma, G.A. Altenberg, H.J. Liang, Nanodiscs: a versatile nanocarrier platform for cancer diagnosis and treatment, Chem. Soc. Rev. 51(5) (2022) 1702-1728.

[3] A.O. Elzoghby, O. Samir, A. Soliman, S. Solomevich, M. Yu, A. Schwendeman, M.L. Nasr, Nanodiscs: Game changer nano-therapeutics and structural biology tools, Nano Today 53 (2023) 102026.

[4] E.L. Dane, A. Belessiotis-Richards, C. Backlund, J.N. Wang, K. Hidaka, L.E. Milling, S. Bhagchandani, M.B. Melo, S.W. Wu, N. Li, N. Donahue, K.Y. Ni, L.Y. Ma, M. Okaniwa, M.M. Stevens, A. Alexander-Katz, D.J. Irvine, STING agonist delivery by tumour-penetrating PEG-lipid nanodiscs primes robust anticancer immunity, Nat. Mater. 21(6) (2022) 710-720.

[5] I. Noh, Z.Y. Guo, J.R. Zhou, W.W. Gao, R.H. Fang, L.F. Zhang, Cellular nanodiscs made from bacterial outer membrane as a platform for antibacterial vaccination, ACS Nano 17(2) (2023) 1120-1127.

[6] L. Sun, D. Wang, I. Noh, R.H. Fang, W.W. Gao, L.F. Zhang, Synthesis of erythrocyte nanodiscs for bacterial toxin neutralization, Angew. Chem. Int. Ed. 62(21) (2023) e202301566.

[7] Z.Y. Guo, I. Noh, A.T. Zhu, Y.Y. Yu, W.W. Gao, R.H. Fang, L.F. Zhang, Cancer cell membrane nanodiscs for antitumor vaccination, Nano Lett. 23(17) (2023) 7941-7949.

[8] L. Sun, Y. Yu, Y. Peng, D. Wang, S. Wang, I. Noh, R.H. Fang, W. Gao, L. Zhang, Platelet membrane-derived nanodiscs for neutralization of endogenous autoantibodies and exogenous virulence factors, Small (2023) https://doi.org/10.1002/smll.202308327.

[9] S.Y. Wang, D. Wang, Y.O. Duan, Z.D. Zhou, W.W. Gao, L.F. Zhang, Cellular nanosponges for biological neutralization, Adv. Mater. 34(13) (2022) 2107719.

[10] O. Cenciarelli, P.W. Riley, A. Baka, Biosecurity threat posed by botulinum toxin, Toxins (Basel) 11(12) (2019) 681.

[11] A.P. Thottumkara, W.H. Parsons, J. Du Bois, Saxitoxin, Angew. Chem. Int. Ed. 53(23) (2014) 5760-5784.

[12] M. Makarova, L. Rycek, J. Hajicek, D. Baidilov, T. Hudlicky, Tetrodotoxin: History, biology, and synthesis, Angew. Chem. Int. Ed. 58(51) (2019) 18338-18387.

[13] M. Pohanka, Botulinum toxin as a biological warfare agent: Poisoning, diagnosis and countermeasures, Mini-Rev. Med. Chem. 20(10) (2020) 865-874.

[14] K.D. Janda, A Small molecule inhibitors of botulinum neurotoxin, Toxicon 156 (2018) S49-S50.

[15] T. Minamitani, K. Kiyose, R. Otsubo, T. Ito, H. Akiba, R.A. Furuta, T. Inoue, K. Tsumoto, M. Satake, T. Yasui, Novel neutralizing human monoclonal antibodies against tetanus neurotoxin, Sci. Rep. 11(1) (2021) 12134.

[16] A. Nowakowski, C. Wang, D.B. Powers, P. Amersdorfer, T.J. Smith, V.A. Montgomery, R. Sheridan, R. Blake, L.A. Smith, J.D. Marks, Potent neutralization of botulinum neurotoxin by recombinant oligoclonal antibody, Proc. Natl. Acad. Sci. U. S. A. 99(17) (2002) 11346-11350.

[17] M.M. Liu, R. Huang, A. Weisman, X.Y. Yu, S.H. Lee, Y.L. Chen, C. Huang, S.H. Hu, X.H. Chen, W.F. Tan, F. Liu, H. Chen, K.J. Shea, Synthetic polymer affinity ligand for Bacillus

thuringiensis (Bt) Cryl Ab/Ac Protein: The use of biomimicry based on the Bt protein-insect receptor binding mechanism, J. Am. Chem. Soc. 140(22) (2018) 6853-6864.

[18] M. Nakamoto, D. Zhao, O.R. Benice, S.H. Lee, K.J. Shea, Abiotic mimic of endogenous tissue inhibitors of metalloproteinases: Engineering synthetic polymer nanoparticles for use as a broad-spectrum metalloproteinase inhibitor, J. Am. Chem. Soc. 142(5) (2020) 2338-2345.

[19] D.S. Reddy, Progress and challenges in developing medical countermeasures for chemical, biological, radiological, and nuclear threat agents, J. Pharmacol. Exp. Ther. 388(2) (2024) 260-267.

[20] L.F. Zhang, J.C. Leroux, Current and forthcoming approaches for systemic detoxification Preface, Adv. Drug Del. Rev. 90 (2015) 1-2.

[21] N.J. Cho, J.S. Glenn, Materials science approaches in the development of broad-spectrum antiviral therapies, Nat. Mater. 19(8) (2020) 813-816.

[22] Q. Chai, J.W. Arndt, M. Dong, W.H. Tepp, E.A. Johnson, E.R. Chapman, R.C. Stevens, Structural basis of cell surface receptor recognition by botulinum neurotoxin B, Nature 444(7122) (2006) 1096-1100.

[23] H.Z. Shen, Z.Q. Li, Y. Jiang, X.J. Pan, J.P. Wu, B. Cristofori-Armstrong, J.J. Smith, Y.K.Y. Chin, J.L. Lei, Q. Zhou, G.F. King, N. Yan, Structural basis for the modulation of voltage-gated sodium channels by animal toxins, Science 362(6412) (2018) 306.

[24] T. Raisch, S. Raunser, The modes of action of ion-channel-targeting neurotoxic insecticides: lessons from structural biology, Nat. Struct. Mol. Biol. 30(10) (2023) 1411-1427.

[25] Y.N. Zhang, W. Poon, A.J. Tavares, I.D. McGilvray, W.C.W. Chan, Nanoparticle-liver interactions: Cellular uptake and hepatobiliary elimination, J. Control. Release 240 (2016) 332-348.

[26] D. Wang, X.Z. Ai, Y. Duan, N.F. Xian, R.H. Fang, W.W. Gao, L.F. Zhang, Neuronal cellular nanosponges for effective detoxification of neurotoxins, ACS Nano 16(11) (2022) 19145-19154.

[27] H.L. Zhu, R.D. Wassall, M. Takai, H. Morinaga, M. Nomura, T.C. Cunnane, N. Teramoto, Actions of veratridine on tetrodotoxin-sensitive voltage-gated Na+ currents, Na v 1.6, in murine vas deferens myocytes, Br. J. Pharmacol. 157(8) (2009) 1483-1493.

[28] S.J. Khundmiri, S.A. Salyer, B. Farmer, N. Qipshidze-Kelm, R.D. Murray, B.J. Clark, Z.J. Xie, T.A. Pressley, E.D. Lederer, Structural determinants for the ouabain-stimulated increase in Na-K ATPase activity, Biochim. Biophys. Acta 1843(6) (2014) 1089-1102.

[29] B. Tay, T.A. Stewart, F.M. Davis, J.R. Deuis, I. Vetter, Development of a high-throughput fluorescent no-wash sodium influx assay, PLoS One 14(3) (2019) e0213751.

[30] S. Iwabuchi, Y. Kakazu, J.Y. Koh, K.M. Goodman, N.C. Harata, Examination of synaptic vesicle recycling using FM dyes during evoked, spontaneous, and miniature synaptic activities, J. Vis. Exp. 85(85) (2014) e50557.

[31] X.Z. Ai, D. Wang, I. Noh, Y.U. Duan, Z.D. Zhou, N. Mukundan, R.H. Fang, W.W. Gao, L.F. Zhang, Glycan-modified cellular nanosponges for enhanced neutralization of botulinum toxin, Biomaterials 302 (2023) 122330.

[32] S.I. Miyashita, J. Zhang, S.C. Zhang, C.B. Shoemaker, M. Dong, Delivery of single-domain antibodies into neurons using a chimeric toxin-based platform is therapeutic in mouse models of botulism, Sci. Transl. Med. 13(575) (2021) eaaz4197.

Chapter 5 Conclusion

5.1 Neuronal cell membrane coated nanoparticles for effective detoxification of neurotoxins

This chapter covered the preparation and characterization of cell membrane coated nanoparticles for neurotoxin neutralization. By coating neuron cell membranes onto polymeric cores, the resulting nanoparticles inherited surface receptors from source cells, which made them decoys of neurotoxin. We used tetrodotoxin as the model neurotoxin and showed that these nanoparticles were able to lure neurotoxins, bind with and neutralize the toxins, and thus block them from attacking the host neuron cells. The detoxification efficacy in vitro was demonstrated in a cytotoxicity assay, a calcium flux assay and a cell osmotic swelling assay. In the mouse model of TTX intoxication, neuron cell membrane-coated nanoparticles enhanced mouse survival in therapeutic and prophylactic regimens without showing acute toxicity. Overall, this work provides a new type of cell membraned coated nanoparticles by using neurons as the source cell for neurotoxin neutralization. Besides tetrodotoxin, the present of related receptors on nanoparticle surface. The application of this new formulation holds great potential to treat various injuries and diseases caused by neurotoxins.

5.2 Surface modified CNPs for biological neutralization

This chapter presented the functionalization of macrophage membrane-coated nanoparticles via metabolic engineering. In the first part, we report glycan modified CNPs for botulinum toxin neutralization. Specifically, macrophage was metabolically engineered to increase the expression levels of gangliosides. The glycan modified cell membrane was coated onto a polymeric core, creating glycan modified nanoponges. These CNPs with higher levels of gangliosides on the surface had greater binding capacity with botulinum toxin when compared to unmodified counterparts. In a mouse model of botulinum toxin intoxication, the glycan-modified

CNPs showed more pronounced survival benefits in both treatment and preventative regimens. This study demonstrates that combining CNP technique with cell surface glycan engineering holds great promise in the development of nanomedicines. This strategy serves as broad-spectrum countermeasures against emerging threats posed by BoNT and other neurotoxins..

In the second chapter, we adopted the metabolic engineering strategy to fabricate heparin modified CNPs for virus neutralization. In particular, cellular nanosonges were made with azido expressing host cell membranes followed by conjugating different density of heparin onto CNPs surface. Modified cellular nanosonges brought heparin to the proximity of their surface receptor, which cooperated to enhance virus binding. Thus, CNPs with a higher level of heparin density bound more SARS-Cov-2 S proteins and showed a higher inhibition efficacy against SARS-Cov-2 live virus infectivity. Therefore, heparin-engineered CNP is an effective platform to neutralize SARS-Cov-2. Its applications can be extended to the neutralization of other heparin-dependent viruses. Overall, surface modified CNPs offer more functions with the potential to neutralize various pathological agents.

5.3 Cell membrane based nanodiscs for broad spectrum neutralization

Nanodiscs, discoidal nanostructures enclosed by membrane scaffold stabilizers, are a compelling nanomedicine platform due to their ultrasmall size and distinct disc shape. This chapter presented the utilization of nanodiscs for the broad spectrum neutralization of bacterial toxins and neurotoxins. In the first section, we report a red blood cell membrane based nanodisc, synthesized by mixing cell membrane with amphiphilic scaffold copolymer. The resulting nanodiscs neutralized hemolytic activity and cytotoxicity caused by α-toxin and whole secreted proteins from methicillin-resistant Staphylococcus aureus bacteria. After administering those

toxins into mice, nanodiscs treated mice conferred survival benefits in both therapeutic and prevention regimens.

In the second section, we generated nanodisc by using neuron cell membranes through a similar self assembly process. We assess their efficacy in neutralizing tetrodotoxin and botulinum toxin. In vitro cell function assays demonstrated nanodiscs bound with tetrodotoxin, preventing ion channel blockage. We also showed that these nanodiscs reversed botulinum toxin induced inhibition of synaptic vesicle recycle. In mouse models of intoxication, nanodiscs offered significant survival benefits. Overall, these findings underscore the potential of nanodiscs for broad-spectrum neutralization and their importance in combating related threats to human health.